
Robust Artificial Clock Transition by Continuous Dynamical Decoupling in Multi-Ion Calcium Crystals

Von der QUEST-Leibniz-Forschungsschule der
Gottfried Wilhelm Leibniz Universität Hannover

zur Erlangung des akademischen Grades

Doktor der Naturwissenschaften

Dr. rer. nat

genehmigte Dissertation von

Lennart Pelzer, Dipl.-Phys.

2023

Robust Artificial Clock Transition by
Continuous Dynamical Decoupling in
Multi-Ion Calcium Crystals

Lennart Pelzer

Referent: Prof. Dr. Piet O. Schmidt

Gottfried Wilhelm Leibniz Universität Hannover und
Physikalisch-Technische Bundesanstalt, Braunschweig

Korreferent: Prof. Dr. Christian Ospelkaus

Gottfried Wilhelm Leibniz Universität Hannover und
Physikalisch-Technische Bundesanstalt, Braunschweig

Korreferent: Prof. Dr. Roei Ozeri

Weizmann Institute of Science, Rehovot

Tag der Disputation: 9. Februar 2022

Abstract

Optical atomic clocks reach astonishingly low frequency uncertainties. Therefore, they are a valuable tool for applications even beside time determination. Predicted extensions of the standard model of particle physics can be tested using these clocks. For this reason, they can help to uncover unresolved discrepancies between these models and the observed universe. A low frequency uncertainty also enables height measurements according to general relativity. Clock comparisons over long distances might be used to refine geodetic models of the earth's gravitational potential.

A variety of atomic species and techniques are in competition for realizing the most accurate clock. The aluminium single ion clock is, at the moment, the most accurate clock. But it is impeded by long averaging times due to the quantum projection noise limit. For some of the aforementioned applications, this is a serious drawback. Larger ion crystals offer an increased signal-to-noise ratio, but maintaining their frequency accuracy is demanding, as the strong confinement potentials shift the atomic resonance.

This thesis reports on the experimental realization of a continuous dynamical decoupling technique. Designed coupling of Zeeman sub-levels by radio-frequency fields is used to mitigate major frequency shifts in $^{40}\text{Ca}^+$ crystals. The obtained artificial clock transition has the potential to compete with more promising clock transitions of different atomic species regarding its low sensitivity to magnetic field fluctuations as well as suppressed quadrupole and tensorial ac-Stark shifts.

Long coherence times in multi-ion $^{40}\text{Ca}^+$ crystals are obtained for the artificial transition. Thus, the system's potential for a low statistical uncertainty makes it promising as a replacement for a lattice clock in a compound clock or for applications where frequency differences must be determined on a short timescale.

Keywords: continuous dynamical decoupling, multi-ion, frequency metrology, optical atomic clock

Zusammenfassung

Optische Atomuhren erreichen außergewöhnlich niedrige Frequenzunsicherheiten. Daher sind sie selbst für Anwendungen neben der Zeitbestimmung ein nützliches Werkzeug. Erweiterungen des Standardmodells der Teilchenphysik können durch sie getestet werden und somit können sie helfen, ungelöste Diskrepanzen dieser Modelle mit dem beobachteten Universum aufzudecken. Außerdem werden Höhenmessungen nach Vorhersage der allgemeinen Relativitätstheorie ermöglicht. Uhrenvergleiche über lange Distanzen können verwendet werden, um geodätische Modelle des Gravitationspotentials der Erde zu verbessern.

Viele Atomarten und Techniken konkurrieren um die Realisierung der genauesten Uhr. Derzeit hat die Aluminium-Einzelionenuhr die höchste Genauigkeit. Aufgrund ihrer Limitierung durch Quanten-Projektions-Rauschen sind lange Mittelungszeiten erforderlich. Dies ist ein großer Nachteil für einige der oben genannten Anwendungen. Mehrionenkristalle bieten ein größeres Signal-zu-Rauschverhältnis, die Erhaltung ihrer Frequenzgenauigkeit wird jedoch durch die starken Einschlusspotentiale erschwert, welche die atomare Resonanz verschieben.

Diese Arbeit beinhaltet die experimentelle Realisierung einer kontinuierlich dynamischen Entkopplungstechnik. Maßgeschneiderte Radiofrequenzfelder werden zur Kopplung von Zeeman-Zuständen genutzt, um einige Frequenzverschiebungen in $^{40}\text{Ca}^+$ Kristallen abzuschwächen. Der künstlich erzeugte Uhrenübergang hat das Potenzial, zu vielversprechenderen Übergängen anderer Atomarten aufzuschließen. Dies gilt in Hinblick auf seine geringe Empfindlichkeit gegenüber Magnetfeldfluktuationen, sowie der unterdrückten Quadrupol- und tensoriellen, dynamischen Stark-Verschiebung.

Für den künstlichen Übergang werden lange Kohärenzzeiten in Mehrionen $^{40}\text{Ca}^+$ Kristallen erreicht. Der Austausch von Gitteruhren in einer Hybriduhr durch große Ionenkristalle wird aufgrund der langen Kohärenzzeiten ihres künstlichen Übergangs denkbar. Außerdem ist der künstliche Übergang für Anwendungen interessant, bei denen Frequenzunterschiede auf einer kurzen Zeitskala bestimmt werden müssen.

Contents

I	Introduction	
1	History of time measurements	3
2	Optical atomic clocks	5
3	Statistical uncertainty in ion clocks	9
II	Setup	
4	Ion trap	15
4.1	DC voltages	16
4.2	Radio-frequency supply chain	17
5	Offset magnetic field coils	19
5.1	Active magnetic field stabilization	19
5.2	Ac-mains line magnetic field noise	20
6	Experimental control	23
6.1	Laser control	23
6.2	Sequences	24
7	Rf-field coils	27
7.1	Rf-Waveform	29
8	Laser system	33
8.1	Calcium	33
8.2	Ionization and loading of neutral ^{40}Ca	33
8.3	Wavelength meter frequency stabilization	35
8.4	Clock laser setup	36
8.5	Beam configuration	49
9	Imaging system	51
9.1	Multi-ion state discrimination	52
III	Setup characterization	
10	Coherent optical spectroscopy	59
10.1	Dynamics of a trapped ion	61
10.2	Ion-light interaction	63
11	Systematic shifts	67
11.1	Motion induced frequency shifts	67
11.2	External field shifts	80
11.3	Trapping potential shifts	83
IV	Continuous dynamical decoupling	
12	Introduction	93
13	Continuous dynamical decoupling theory	95

13.1	Magnetic field suppression	99
13.2	Tensor shift suppression	101
14	Single ion results	105
14.1	Calibration	105
14.2	Optical coupling	109
14.3	Frequency shift suppression	112
14.4	Linewidth and stability	117
15	Multi-ion results	123
15.1	Crystal shape	123
15.2	Inhomogeneous fields	125
15.3	Quadrupole shift suppression	126
V Outlook and Summary		
16	Continuous dynamical decoupling improvements	133
17	New experimental control system	135
18	Compound clock	137
19	Spherical ion crystal	139
20	Summary	143
VI Appendix		
A	Ion crystal shape	147
B	Laser angle determination	149
C	Waveforms for continuous dynamical decoupling	151
D	Continuous dynamical decoupling parameter sets	153
E	Optical coupling of first stage artificial transition	155
E.1	Analytic function for deriving CDD transitions .	155
F	Error signal corrections by optical coupling variations	159
G	Bibliography	161

Acronyms

- ac alternating current 6
- AlN aluminium nitride 15
- AOM acousto-optic modulator 23
- AWG arbitrary waveform generator 29
- BBR blackbody radiation 15
- BSB blue sideband 65
- CDD continuous dynamical decoupling 12
- CEO carrier-envelope offset 46
- DAC digital-to-analog converter 16
- dc direct current viii, 15
- DDS direct digital synthesizer viii, 23
- ECDL external cavity diode laser 34
- EIT electromagnetically induced transparency 33
- EMM excess micromotion 62
- EOM electro-optic modulator 40
- FNC fibre noise cancellation 41
- FPGA field-programmable gate array 23
- FWHM full width at half maximum 10
- LO local oscillator 5
- PBS polarizing beamsplitter 36
- PD photo-diode 49
- PDH Pound-Drever-Hall 35

PID proportional–integral–derivative 18

PLL phase-locked loop 41

PM polarization maintaining 38

PMT photomultiplier tube 24

PTB Physialisch-Technische Bundesanstalt 23

QPN quantum projection noise 4

QPS quadrupole shift 88

RBW resolution bandwidth 40

rf radio-frequency 5

RLC resistor-inductor-capacitor circuit 27

ROI region of interest 55

RSB red sideband 65

RWA rotating wave approximation 64

SBC resolved sideband cooling 33

sCMOS scientific complementary metal–oxide–semiconductor
51

SI international system of units 3

SNR signal-to-noise ratio 6

TASS tensor ac Stark shift 89

TEC thermoelectric cooler 38

TTL transistor–transistor logic 29

VCO voltage controlled oscillator 41

VCO-DDS custom dc voltage steerable DDS 38

WM wavelength meter 35

Mathematical symbols

a^\dagger annihilation operator 63

$\Omega_{m_{0S}, m_{0D}}$ bare Zeeman optical coupling strength 109

ω_0 bare Zeeman state splitting 95

J_i Bessel function of the first kind 83

μ_B Bohr magneton 80, 95

a_0 Bohr radius 88

C capacitance 28

f_{CEO} carrier-envelope offset 44, 46

α_i coil field angle 95

f_{rep} comb pulse repetition rate 44

a creation operator 63

$\Delta\alpha_0$ differential static electric-dipole polarizability 86

δ Dirac delta function 83

E_0 electric field amplitude 59

$S_E(\omega_i)$ electric field spectral density 78

e elementary charge 88

$|e\rangle$ excited state wavefunction 59

Ω_1 first drive coupling strength amplitude 95

Δ_1 first drive detuning 95, 99

m_{1D} first stage D level quantum number 98

ω_1 first stage drive frequency 95, 96

θ_1 first stage mixing angle 96, 112

m_{1S} first stage S level quantum number 98

$\bar{\omega}_1$ frequency splitting of the first stage dressed states 96, 99
 $\bar{\omega}_2$ frequency splitting of the second stage dressed states 97
 κ geometric factor 61
 $\frac{\partial E_i}{\partial r_j}$ gradient of the electric field 88
 $|g\rangle$ ground state wavefunction 59
 $g_{S(D)}$ gyromagnetic factors 95
 L inductance 28
 $\phi_{\text{CEO}}(t)$ instantaneous carrier-envelope offset phase 45
 $\phi_{\text{rep}}(t)$ instantaneous repetition rate phase 45
 $H^{-1}(s)$ inverse transfer function 30
 q ion charge 62
 m ion mass 62
 η Lamb-Dicke parameter 64, 125, 139
 g_J Landé g-factor 80
 $\Delta\nu$ laser detuning 59
 ν_L laser frequency 59, 109
 β modulation index 83
 \dot{n} motional heating rate 78
 Γ natural linewidth 68
 N number of ions 78, 79, 124
 NA numerical aperture 51
 Ω_{729} optical Rabi frequency 108
 $\sigma_z, \sigma^+, \sigma^-$ Pauli spin matrices 63
 $\vec{\epsilon}$ polarization vector 59
 $S_\nu(f)$ power spectral density 38, 40
 Θ quadrupole moment 88, 89, 123

Q_{ij} quadrupole operator 101
 χ_1 quadrupole shift suppression factor first stage 102
 χ_2 quadrupole shift suppression factor second stage 102
 Q quality factor 77
 Ω Rabi frequency 59
 R resistance 28
 Ω_2 second drive coupling strength amplitude 97
 m_{2D} second stage D level quantum number 98
 ω_2 second stage drive frequency 96
 θ_2 second stage mixing angle 97
 m_{2S} second stage S level quantum number 98
 ω secular mode frequency 68
 $J_{z,S(D)}$ spin-Z operator 95
 α_0 static electric-dipole polarizability 139, 143
 n tooth number 44
 J total angular momentum quantum number 80
 $H(s)$ transfer function 29
 ν_a transition frequency 59, 109
 U_{DC} trap dc-voltage amplitude 61
 Ω_{rf} trap drive frequency 61
 U_{rf} trap rf-voltage amplitude 61
 \vec{n} unit vector 59
 $U_{\vec{r}}(\phi)$ unitary rotation with angle ϕ around \vec{r} 95
 \hat{r} valence electron position operator 59
 \vec{k} wavevector 83
 m_J Z-component of the total angular momentum 124
 m_{0D} Z-component of the total angular momentum D-level 98
 m_{0S} Z-component of the total angular momentum S-level 98

List of Figures

Figure 2.1	Sketch of an optical ion clock	6
Figure 4.1	Model of the segmented Paul trap	16
Figure 4.2	Voltage supply of the trap electrodes	17
Figure 5.1	Homogeneity of the axial offset B-field	20
Figure 5.2	Measurement of ac-mains line B-field noise	21
Figure 6.1	Sketch of a spectroscopy pulse sequence	24
Figure 7.1	Rf-coils overview.	28
Figure 7.2	Bode diagram of the rf-coil transfer function	29
Figure 7.3	Residuals of the rf-coil transfer function	30
Figure 8.1	$^{40}\text{Ca}^+$ level scheme	34
Figure 8.2	729 nm laser setup	37
Figure 8.3	729 nm transfer stabilization spectrum	39
Figure 8.4	Pound-Drever-Hall stabilization linewidth	40
Figure 8.5	Oadev fibre length noise	42
Figure 8.6	Schematic fibre-noise cancellation diagram	43
Figure 8.7	Transfer-lock laser stabilization	45
Figure 8.8	Oadev of relevant comb signals	48
Figure 8.9	Sketch of vacuum chamber cross-section	49
Figure 9.1	Sketch of the imaging system	52
Figure 9.2	PMT count histogram of a five ion crystal	53
Figure 9.3	Histogram of camera data	55
Figure 10.1	Sketch of coupled system	63
Figure 11.1	Doppler cooling rate coefficients	68
Figure 11.2	Sideband cooling sketch	70
Figure 11.3	EIT-cooling schematic	72
Figure 11.4	EIT-cooling rate	74
Figure 11.5	Cooling techniques comparison	75
Figure 11.6	EIT-cooling of five ion crystal	76
Figure 11.7	Heating rates of a single ion	77
Figure 11.8	Time dilation shift from mode heating	79
Figure 11.9	Relative optical coupling strength	81
Figure 11.10	Trap rf-field on nodal line	84
Figure 11.11	Radial rf-drive electric field	85
Figure 11.12	Trap drive-induced 2 nd order Doppler and ac-Stark shift	87
Figure 13.1	Sketch of the CDD level-scheme	99
Figure 13.2	B-field shift sensitivity 1 st stage CDD	100
Figure 13.3	B-field shift sensitivity 2 nd stage CDD	101

Figure 13.4	Calculated QPS suppression by CDD . . .	102
Figure 14.1	1 st stage CDD calibration steps	107
Figure 14.2	Adiabatic CDD preparation sweep	108
Figure 14.3	Relative optical coupling strength 1 st stage CDD	111
Figure 14.4	CDD suppression of B-field shift	113
Figure 14.5	Oadev typical B-field noise	114
Figure 14.6	Simulated influence of B-field noise on the artificial transition	114
Figure 14.7	Drive amplitude sensitivity of artificial transition	115
Figure 14.8	Oadev CDD coupling strength	116
Figure 14.9	Sensitivity of CDD to coil temperature . .	116
Figure 14.10	Frequency scan of a 2 nd stage transition .	118
Figure 14.11	Oadev 2 nd stage transition single ion . . .	119
Figure 14.12	CDD pulse time scan	121
Figure 14.13	Fast Rabi oscillations on the CDD transition	122
Figure 15.1	Calculated QPS five ion crystal	124
Figure 15.2	Spatial inhomogeneity B-fields	126
Figure 15.3	Five ion QPS with resonant drive	127
Figure 15.4	Five ion QPS suppression of CDD	128
Figure 15.5	Oadev five ion crystal	129
Figure 19.1	Simulations of spherical multi-ion crystals	139
Figure 19.2	Simulations of linear multi-ion crystals . .	140
Figure 19.3	Camera picture of a spherical crystal . . .	141
Figure F.1	Frequency sensitivity dependency	159
Figure F.2	Frequency deviation 2 nd stage artificial transition by B-field changes	160

Part I

Introduction

Alice: How long is forever?

White Rabbit: Sometimes, just one second.

— Lewis Carroll

History of time measurements

Every clock is based on a periodic process. The oscillations of this process are counted to measure the elapsed time. The unit of time is defined by a specific oscillator's period. For example, one day is equal to one complete rotation of the earth around its axis¹, one second is a certain amount of oscillations of a quartz crystal oscillator etc. During the evolution of mankind the periods of the used oscillators tended towards higher frequencies. This is due to the general trend of decreasing uncertainty for increased period frequency. The quality factor of an oscillator

$$Q = \frac{f_0}{\Delta f}$$

is a measure for this relation. Here, f_0 is the centre frequency of an oscillation and Δf its uncertainty. The uncertainty typically improves over time by technical means, but at some point it is more favourable to choose a system with higher frequency to increase the performance of the new clock.

For most of history, the local time referencing to the position of the sun was sufficient for all needs. In the 19th century country spanning railway systems made synchronization of these local clock realizations necessary for the first time.

The invention of atomic clocks in 1949 [81] and the first realization with caesium in 1955 by Essen and Parry [35] paved the way from a universal applicable but imprecise definition based on a year to a local realized but universal applicable standard with higher accuracy. This is based on the fundamental indistinguishability of atoms of the same species. In 1967, the definition of the second was set from the International Bureau of Weights and Measures as the duration of a certain number of periods of the ¹³³Cs ground state hyperfine level splitting [139]. In the following decades, technological progress from the early atom beam clocks to modern caesium-fountain clocks increased the accuracy of frequency measurements of this transition. Modern Cs-fountain clocks provide a long probe time by launching a cold cloud of atoms ballistically through the interrogation zone.

¹ The modern definition is of course referenced to the international system of units (SI)-second.

They reach an accuracy of 1.6×10^{-16} and quantum projection noise (QPN)-limited statistical fractional frequency uncertainty of $2.5 \times 10^{-14}1/\sqrt{\tau}$ ². Using laser cooling of the atoms leaves frequency shifts due to collisions within the atom cloud the biggest uncertainty contribution [140].

Worldwide, many primary frequency standards³ contribute to the calibration of the *International Atomic Time* from which the local times are derived. The backbone of many modern applications that require precise timing across long distances are secondary frequency standards. They have to be calibrated against the primary standards to ensure accuracy for longer times, but benefit from their small form-factor, low cost and reliable operation. These devices are used in satellite navigation, communication, management of electrical grids etc.

-
- 2 This value is only reached for higher atom densities, which reduces the accuracy. In high accuracy operation mode, typical uncertainties of $1.5 \times 10^{-13}1/\sqrt{\tau}$ are observed.
 - 3 The terms *frequency standard* and *clock* are not equal as the latter includes counting of periods and the definition of the length of these intervals. A visual distinction is given in fig. 2.1. However, to ease reading of the manuscript, this discrimination is omitted mostly.

Optical atomic clocks

Increasing the frequency of the system is the consistent way to improve performance beyond the caesium based clocks. The higher quality factor of narrow optical transitions with shorter wavelength makes the usage of these attractive as an atomic reference.

Here, lasers take over the role of the microwave oscillator as a local oscillator (LO) in a Cs-clock. The development of lasers has become an unimagined success story since the second half of the 20th century. From the first realizations [86], usage of new active media and techniques led to rapid expansion of the field. Nowadays, lasers are an indispensable tool in communication, manufacturing and science applications. Atomic spectroscopy has benefited from this development by the availability of lasers with ever decreasing wavelength and advancing technical maturity.

The spectral gap between the optical and microwave domain posed a hurdle for the practical implementation of optical frequency standards as optical frequencies are not directly electronically countable. The invention of the frequency comb in the beginning of this century [48] superseded the laborious use of frequency chains [125]. Here, the spectrum of a mode-locked femtosecond laser acts as a stable ruler in frequency space which bridges the gap between optical frequencies and countable radio-frequency (rf). Therefore, referencing of optical wavelength to the SI-second became possible.

The main ingredient of an optical frequency standard is a suitable atomic transition. Their selection is mainly based on the sensitivity to environmental perturbations. The availability of suitable cooling methods avoids motional induced shifts, hence the ease of its technical implementation becomes a selection criterion. In order to benefit from the high quality factor, restriction of the atom movement is necessary. Two distinct types of optical clocks are commonly used to confine the atom movement. Optical lattice clocks store an ensemble of thousands of neutral atoms in an optical lattice. Here, intense counter-propagating beams of light form a periodical lattice whose light force is exploited to trap neutral atoms [13]. In contrast, optical clocks

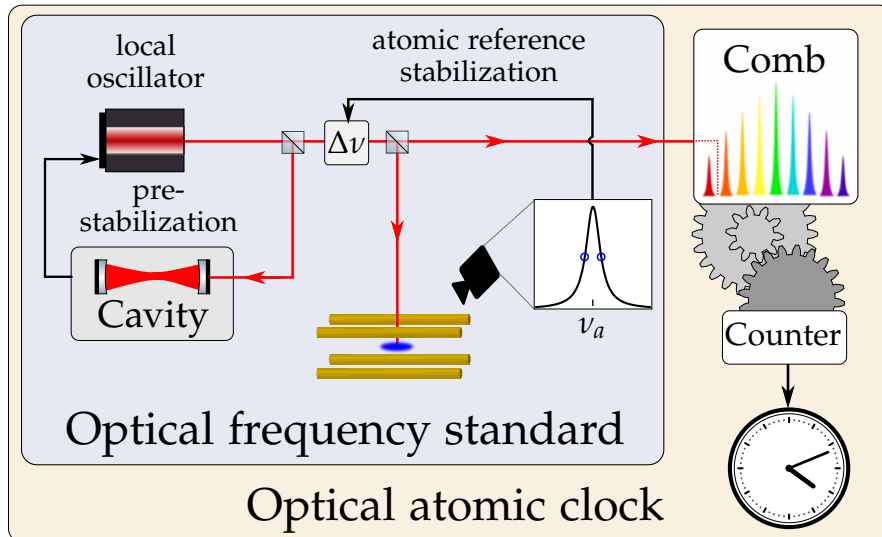


Figure 2.1: Sketch of the working principle of an optical ion clock. A laser acts as LO for an atomic transition with resonance frequency ν_a . The oscillator is pre-stabilized using feedback from a reference cavity. The response of a trapped ion to laser radiation is detected, and the resonance frequency is deduced. An active control loop corrects the laser frequency by $\Delta\nu$ to keep the laser at the atomic resonance frequency. For an optical atomic clock, the optical frequency must be translated into countable frequencies to define a time. Therefore, a frequency comb acts as gearbox to translate between the optical and the rf-domain.

based on trapped ions use the particle's charge to confine it using electric fields [101].

The main advantage of lattice clocks is their large atom number, which significantly improves signal-to-noise ratio (SNR) and therefore decreases the statistical uncertainty limited by QPN. But especially the strong light forces in lattice clocks must be well controlled to maintain the systematic uncertainty. Typically, the lattice laser is operated at a *magic wavelength* where the alternating current (ac)-Stark shifts from different levels cancel to a high degree. An additional drawback is a low duty cycle due to reloading of the trap after each interrogation. This limits the clock's ability to correct LO noise in certain frequency regions due to the Dick-effect [24].

In a linear Paul trap, a single ion can be held at the field-free minimum of the trapping potential with high precision, therefore systematic frequency shifts are typically easier to quantify. However, for extended multi-ion crystals this is no longer true.

Therefore, most ion clocks use only a single ion to preserve the systematic uncertainty, resulting in a high statistical uncertainty.

There is an active competition among different clock atom species. The $^{27}\text{Al}^+$ single ion clock at the National Institute of Standards and Technology is currently the most accurate clock with an accuracy reaching a 9.4×10^{-19} fractional frequency uncertainty and a statistical uncertainty of $1.2 \times 10^{-15} \frac{1}{\sqrt{\tau}}$ [15]. Due to the high statistical uncertainty, it requires a long measurement time to reach this level of accuracy. Other ionic species like $^{171}\text{Yb}^+$ [59], $^{199}\text{Hg}^+$ [114], $^{88}\text{Sr}^+$ [32], among others, reach accuracies at a level from 10^{-17} to low 10^{-18} . The leading lattice clock candidates strontium and ytterbium report systematic shifts of the order of 2×10^{-18} , and their statistical uncertainty of below $5 \times 10^{-17} \frac{1}{\sqrt{\tau}}$ exceeds the capabilities of single ion clocks by two orders of magnitude [14, 90].

As the second is fixed by the Cs hyperfine transition frequency, more accurate absolute frequency measurements are not possible by definition. Therefore, the performance of the individual systems are compared by frequency ratio measurements via frequency comb or direct comparison of independent clocks of the same species. It is expected that the SI-second will be re-defined in the future based on one or several optical transitions [41, 109].

Quantum logic spectroscopy lifts the restriction of finding an atomic species which contains a level scheme suitable for cooling, detection and in addition, a suitable clock transition. Here, the spectroscopy ion is co-trapped with a *logic ion* to share these tasks. The information of the clock transition frequency gained within a spectroscopy pulse is transferred via a joint motional mode to the logic ion's internal state, from which it can be read out. The logic ion is typically also used for sympathetic cooling via the coupled motional modes of the mixed ion crystal. This technique was originally developed for a mixed beryllium aluminium clock [123], but is transferable to a large variety of systems including molecular ions [144], highly-charged ions [92] and the nuclear thorium clock [6]. The latter two systems are expected to offer unrivalled clock transitions, as either a fraction or the complete electron shell structure shields the relevant electrons or the nucleus from external perturbations.

The outstanding accuracy of optical clocks make them a suitable tool for testing theories beyond the boundaries of the fundamental laws of physics [116]. The standard model of particle physics has proven itself by numerous accurate predictions in many fields. Nevertheless, mainly cosmological observations

raise unsolved questions like matter-antimatter asymmetry and the existence of *dark matter* and *dark energy*. Therefore, there is a brisk research effort to find an extension to the standard model. Some predictions of new theories can get tested with low-energy high-precision experiments like optical clocks. This includes for example the temporal or spatial variation of fundamental constants [114], violation of the local Lorentz invariance, local position invariance [73] and tests of predictions of quantum electrodynamics [92].

An application with interdisciplinary impact is *chronometric levelling*. According to general relativity, a gravitational potential changes the local time of a clock. On the surface of the earth, 1 cm height difference corresponds to a fractional frequency shift of 1×10^{-18} [91]. Optical clocks measuring this gravitational redshift extend the toolbox of geodetic applications by a local reference, whose height can be compared almost instantly to another clock over a large distance via fibre-link. This can help e.g. to establish an international height reference frame [145]. Especially transportable optical atomic clocks are interesting in this respect. First performed measurements have shown the realization of these ideas [44, 132].

Statistical uncertainty in ion clocks

As stated previously, the statistical uncertainty is the major obstacle for modern single ion based frequency standards. Beside the effort to operate the clocks for a longer time, some applications, e.g. the resolution of tidal earth deformations with chronometric levelling, require a low frequency uncertainty within a few hours [135].

All described atomic frequency standards are interrogated non-continuously. In a first step, the atoms are prepared by laser cooling and population preparation in a particular state. Then, a laser pulse with the *clock laser* is applied for a duration T_i to imprint the information of the frequency difference of laser and atomic resonance onto the atom's internal state. Afterwards, the state of the ion is measured to collect this information.

This is a projective measurement which gives only partial information about the atom's excitation probability P_e in the excited state due to its quantum-mechanical nature. With N such measurements on an ensemble of uncorrelated two-level atoms or subsequent probing of a single one, the uncertainty of the state population is given by the quantum projection noise (QPN) [60]

$$\Delta P_{\text{QPN}} = \sqrt{\frac{(1 - P_e)P_e}{N}},$$

which takes the form of a binomial distribution.

One meaningful measure for the statistical processes of an oscillator is given by the Allan Variance¹ [110]

$$\sigma_y^2(\tau) = \frac{1}{2(M-1)} \sum_{i=1}^{M-1} (y_{i+1} - y_i)^2, \quad (3.1)$$

with the i^{th} of M fractional frequency values y_i averaged over the measurement interval τ .

¹ Within this work, exclusively the overlapping Allan deviation *oadev* was used. It makes maximal use of a data set by accounting every possible combination of samples [110].

The quantum projection noise (QPN)-limit of an atomic clock is given by [108]

$$\sigma_y(\tau) = \frac{1}{Q} \frac{1}{K} \underbrace{\frac{1}{\sqrt{N}}}_{1/\text{SNR}} \sqrt{\frac{T_C}{\tau}}, \quad (3.2)$$

$$\frac{dP_e}{dv} = K \frac{P_{e,\text{max}}}{\Delta\nu},$$

with the total cycle time T_C and the interrogation time τ . The clock's *duty cycle* τ/T_C is given by the ratio of the accumulated interrogation time and all other contributions including needed characterization measurements. The constant K of order unity is given by the frequency discrimination slope and thus, it is also dependent on the interrogation method. The *standard quantum limit* scaling $1/\sqrt{N}$ for uncorrelated systems can be broken. Depending on the kind and degree of entanglement, an improvement of the joint system's SNR can reach the *Heisenberg limit* scaling $1/\sqrt{N} \rightarrow 1/N$ [70, 76].

The major parameter a QPN-limited single ion clock of a given species can improve its statistical uncertainty on, is increasing the probe time. This is limited by the natural lifetime of the transition. The Fourier-limited full width at half maximum (FWHM) linewidth $\Delta\nu$ is decreased, and with given preparation time the duty cycle increases. This natural lifetime limit cannot be reached for many species, as the probe time is practically limited by the coherence time² of the used local oscillator [78].

There has been improvements on laser stabilization techniques using optical resonators (*cavities*) [89] or technologically different approaches like spectral hole burning [22] to build narrowband low-drift lasers. But the rate of progress tends to flatten out and the technical effort increases with e.g. the need for cryogenic temperatures for lowering the thermally induced noise on mirror substrates or in spectral hole burning samples.

The usage of compound clocks to avoid these laser limitations is expected to be useful [26, 58]. Here, an auxiliary frequency standard with low statistical uncertainty is used in conjunction with a highly accurate clock. The auxiliary device is used to track phase excursions of the LO synchronously to the interrogation time of the accurate clock. Therefore, the accurate clock can exceed its probe time into a region where, with a given spectral

² In this context, the coherence time is defined as maximal interrogation time, for which the LO phase noise is $|\Phi| \leq \pi/2$ for 99% of all interrogations [89].

distribution of the LO, no unambiguous phase determination would be possible any more. With the coarser phase information gained from the faster cycling clock, the phase can be corrected accordingly. Although much of the infrastructure is already needed for frequency ratio measurements, the operation of two coupled clocks is complex and resource intensive.

In recent years, progress towards multi-ion operation has been made to improve the statistical uncertainty by a larger SNR [4, 66, 67, 134]. The challenges can be divided into two groups. First, suitable multi-ion cooling techniques must be provided to minimize motionally induced frequency shifts [19, 75, 87]. Quantum information experiments based on trapped ions face similar challenges, therefore this field is tightly bound to frequency standard applications [34, 64]. Secondly, the confinement in ion traps is many orders of magnitudes stronger compared to lattice clocks. This may lead to several potentially inhomogeneous field-induced frequency shifts depending on the properties of the used atomic species.

In this work, we investigated the prospect of a combination of these ideas. Instead of an additional lattice clock, a multi-ion crystal is used as phase tracker for the LO. This relaxes the requirements on the systematic uncertainty of the multi-ion system, as the ultimate accuracy will be provided by the single ion. In an $^{27}\text{Al}^+ / ^{40}\text{Ca}^+$ system, synergies can be used to implement such a compound ion clock without exceeding need for additional equipment. An aluminium clock needs a logic ion for *sympathetic cooling* and state readout, as it does not offer a transition for cooling and state detection that can be accessed with current laser technology. One possible candidate for this logic ion is $^{40}\text{Ca}^+$ due to a similar mass-to-charge ratio with respect to $^{27}\text{Al}^+$. This is important for efficient sympathetic cooling of all crystal modes [147]. In addition, $^{40}\text{Ca}^+$ offers the benefit of lower minimal Doppler-cooling temperatures and an easier technical implementation of the needed lasers compared to $^{25}\text{Mg}^+$, although this has a closer mass-to-charge ratio compared to $^{27}\text{Al}^+$.

The focus within this work is on the suppression of frequency shifts in multi-ion $^{40}\text{Ca}^+$ crystals, which either broaden the natural linewidth of its clock transition or fluctuate on the timescale of the stabilization loop to the $^{27}\text{Al}^+$ transition. The former would decrease the statistical uncertainty. The latter is in the optimal case of maximal probe time a multiple of its natural lifetime of $\tau \approx 21$ s.

The major building blocks of the experimental setup are summarized in part II. In part III the major frequency shifts of the $^{40}\text{Ca}^+$ system are characterized and in part IV a technique called continuous dynamical decoupling (CDD) to suppress the leading frequency shifts is introduced together with its performance evaluation. Finally, the results are summarized and the prospect for further developments is given in part V.

Part II

Setup

The setup used for the experiments shown in part III and part IV is presented in the following part. First, the linear Paul trap is presented in chapter 4. A detailed description of the control and generation of the static and rf-magnetic fields is given in chapter 5 and chapter 7 respectively. The experimental control system is presented in chapter 6. Several lasers are used for laser-cooling, state-preparation and readout of the state of the ions. The purpose and setup of these are presented in chapter 8 with focus on the clock laser frequency stabilization. The imaging system for detecting ion crystals is introduced in chapter 9. Further information about the setup can be found in Hannig *et al.* [49] and [50].

Ion trap

High precision spectroscopy experiments require a particle at rest. Therefore, a linear Paul trap was chosen to tightly confine the motion of ions to a small region where they can be cooled. The segmented trap design offers additional freedom to shape the confining potential and trap multiple ion crystal ensembles.

The design of the trap was developed for multi-ion clock operation in the group of Tanja Mehlstäubler. Key parameters are low axial micromotion and low motional heating of the ions. For the former, potential simulations are performed to optimize especially the segmentation gap size and width [17, 55, 106]. In conjunction with high alignment precision of the trap assembly, low axial micromotion and heating rates could be attained with those traps [67].

The trap used in this work consists of a stack of four precisely aligned Rogers¹ circuit boards which contain the electrode structures. For micromotion compensation, the ion crystals must be precisely positioned in all three spatial directions, therefore two sets of direct current (dc)-electrodes are provided. The individual boards are separated with spacers and mounted onto an aluminium nitride (AlN) carrier board containing the electrical dc-connections (fig. 4.1). The laser-cut electrode structures are gold coated. For low motional heating, low residual electric field noise is required, therefore all dc-voltages are low-pass filtered on the trap. Furthermore, an rf-supply via a helical resonator with high quality-factor is used.

Good thermal management is necessary to avoid temperature-induced trap deformations and minimize the blackbody radiation (BBR)-shift uncertainty (section 11.2.2). Small rf-losses and high thermal conductivity of the used materials are beneficial. Therefore, AlN has replaced Rogers as circuit board material in further developments. Two temperature sensors² mounted on the two rf-boards provide in situ temperature monitoring. Further information about the trap installation can be found in [50].

¹ RO4350BTM, Rogers Corporation

² PT100

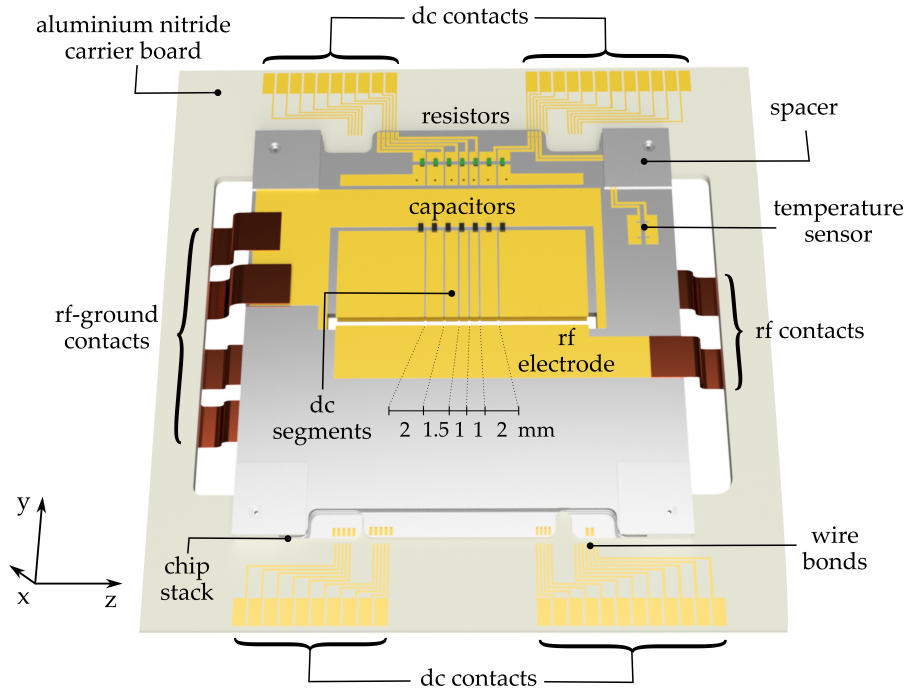


Figure 4.1: Rendered CAD model of the trap assembly. The trap consists of four gold coated stacked Rogers chips mounted onto an aluminium nitride carrier board. The outer compensation layer was removed for a better overview. The electrical connections as well as the position of one temperature sensor is indicated. The two sets of main and compensation dc-electrodes consist of five individually supplied segments of sizes 2.0 mm, 1.5 mm, 1.0 mm, 1.0 mm and 2.0 mm and two longer end caps each. All electrodes are filtered on the trap chip and connected via capacitors with rf-ground.

4.1 DC voltages

The operation of the segmented Paul trap requires 28 low-noise, low-drift dc-voltages. They are applied to the individual electrodes for providing axial confinement and micromotion compensation (fig. 4.2). Each electrode is low-pass filtered directly on the circuit board with a cut-off frequency of $f_c = 113$ Hz [50]. Additionally, each electrode is connected via capacitors to ac-ground.

The voltage source is based on a 16 bit digital-to-analog converter (DAC) card³. Its voltage outputs are combined, amplified and filtered with dedicated electronics [7, 50] to obtain common mode and differential voltages for individual electrode pairs of each trap segment (fig. 4.2). These voltages are controlled within the experimental control program (chapter 6).

³ cDAQ-9174 equipped with three 9264 modules, National Instruments

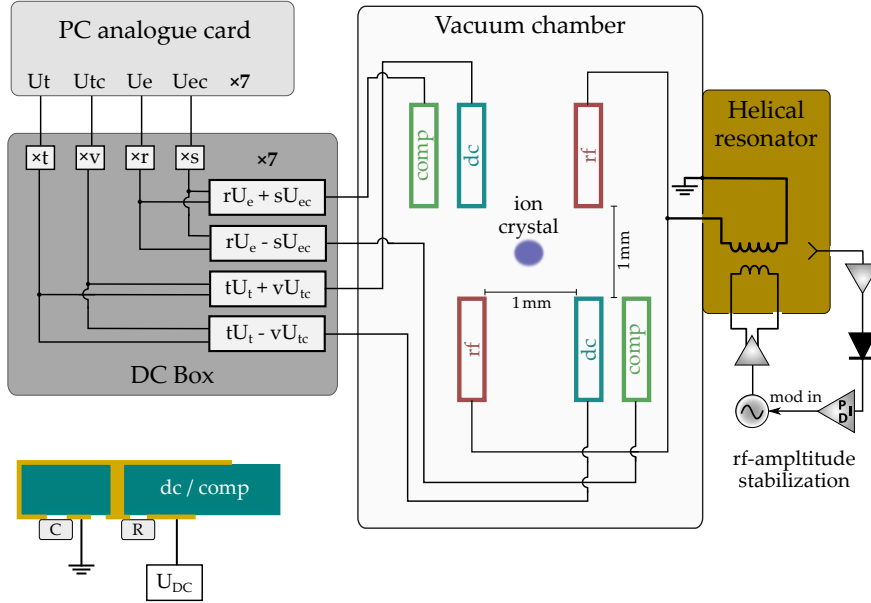


Figure 4.2: Sketch of the voltage supply of the trap electrodes (not to scale). The 28 dc-voltages are sourced by a PC-controlled DAC-card, amplified by the factors $t = r = 12$, $v = 0.25$, $s = 1$, filtered and combined within the dc-electronics box. The trap drive rf-voltage is amplified in the helical resonator and fed into the vacuum chamber. The rf-source is amplitude stabilized using the rectified signal of a pickup antenna. Each dc-electrode features a low-pass filter with respect to the rf-ground (sketch on the lower left). The rf-ground is connected to the helical resonator shield as well as the vacuum chamber. The ground of the DC supply is also attached to the vacuum chamber.

4.2 Radio-frequency supply chain

Large rf-amplitudes are required to provide secular frequencies of $\omega_{x(y)} \approx 2$ MHz. A frequency generator⁴ referenced to the 10 MHz maser signal provides the required signal. Its amplified output is fed into the primary coil of a helical resonator [84, 129] for further voltage amplification and impedance matching to the trap's electrodes. In addition, its spectral resonance with a quality factor of $Q = 420$ at $\Omega_{\text{rf}} = 33$ MHz acts as bandpass filter for noise induced within the rf-chain.

The resonance frequency is drifting over time caused by temperature changes of the trap and the resonator itself. This results in a drift of the radial secular frequencies. A feedback loop is installed to keep the applied voltage stable. A pickup antenna reaching into the resonator probes the field within the

⁴ Marconi 2024

resonator. Its amplified signal is converted to dc by a rectifier⁵ and used to steer the amplitude of the rf-source via a proportional–integral–derivative (PID)-controller⁶.

⁵ based on the Schottky diode HMPS-2822, Broadcom

⁶ RedPitaya

Offset magnetic field coils

A finite and well-aligned magnetic field is needed for e.g. state preparation by optical pumping (chapter 10). For this purpose, three pairs of perpendicular oriented coil sets are employed. They are driven by programmable, low noise current sources¹. One main coil pair with diameter 60 cm, separation 50 cm and 61 windings each is aligned so that it generates the needed offset field in direction of the trap axis. The current in the other two pairs is steered to counteract the offset field perpendicular to the trap axis. The main coils are positioned in near Helmholtz configuration, limited by apparatus dimensions.

5.1 Active magnetic field stabilization

The transition frequency of the $^2S_{1/2} \leftrightarrow ^2D_{5/2}$ transition in $^{40}\text{Ca}^+$ is prone to magnetic field fluctuations due to the linear Zeeman effect (see chapter 11). Even with suppression of this effect by CDD, described in section 14.3.1, typical B-field fluctuations are a major contribution to frequency instabilities. In order to keep the magnetic field amplitude constant at the chosen field of $|\vec{B}_0| = B_{0,z} = 0.3568 \text{ mT}$ under external field fluctuations, an active stabilization is installed. The current through an additional coil pair with five windings, wound up on the same holder, is steered by a slow controller with corner frequency of $f_c < 10 \text{ Hz}$. The B-field in axial direction is measured by a fluxgate sensor² placed in an inverted viewport. Optimally, the axial field changes from the control current should be equal at the ion and sensor position to ensure best noise suppression. For the given coil configuration, this optimum position can be found by varying the sensor position in axial and radial direction. The set-point of the control loop is set by a sequencer-controlled analogue voltage card³, whose minimal step size limits the resolution to $\Delta B_{0,z} = 30 \text{ nT}$. With this active stabilization, a magnet-field stability of $\delta B_{0,z} < 5 \text{ nT}$ on the timescale of

¹ QL355TP, AIM-TTI Instruments

² FGM3D/1000, Sensys

³ PCI-6703, National Instruments

100 s is achieved (fig. 14.5). It is limited by imperfect alignment, temperature drift of the sensor and the voltage reference.

A homogeneous Zeeman shift of the clock transition along extended ion crystals requires a homogeneous B-field. In fig. 5.1, the field produced by the main coil arrangement was measured without the vacuum chamber and surrounding parts. The measured data is in good agreement with field simulations of the setup using the Biot-Savart law. However, frequency shift measurements on an ion crystal (compare fig. 15.2a) reveal an unexpectedly large inhomogeneity, indicating a large influence of the contained parts of the setup on the field-shape.

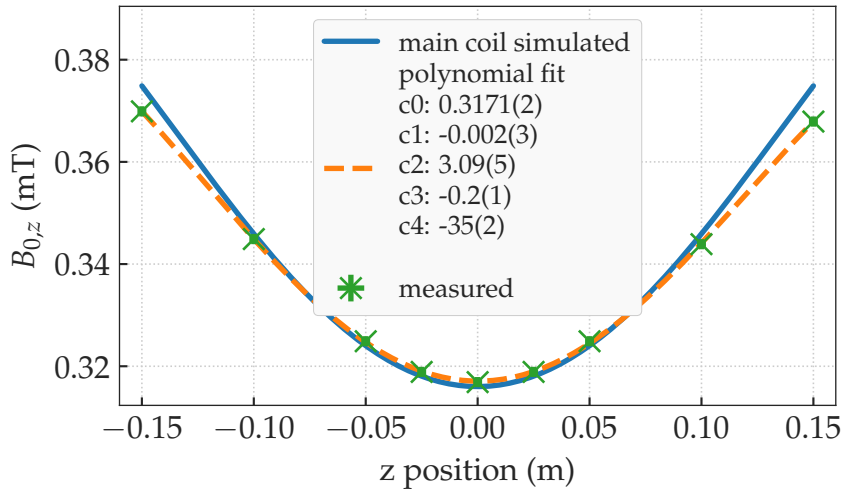


Figure 5.1: Homogeneity of the axial offset magnetic field $B_{0,z}$. The B-field in z-direction was measured without vacuum chamber. The measured values are compared with a magnetic field simulation. The data was approximated with a fourth degree polynomial fit. Measurement uncertainties are barely visible.

5.2 Ac-mains line magnetic field noise

In typical laboratory environments, magnetic field noise from omnipresent mains lines is among the biggest noise contributions. It is generated by B-fields induced from power supply lines of various devices around the ion trap, as well as direct perturbation of the current drivers of the offset coils. Due to the proximity of these devices, the B-fields are inhomogeneous. Therefore, a feedback loop with a magnet-field sensor outside the vacuum chamber is not suitable. The influence of this perturbation can be reduced with magnetic shielding in conjunction

with permanent magnets generating the offset field [115]. Another technique mitigating these noise sources synchronizes the experimental sequence with the mains line cycle (*line-trigger*). For short spectroscopy pulses, the B-field changes are then quasi-static and equal for repeated experiments. In fig. 5.2, the amplitude of mains magnetic field is shown. The sequence start was delayed with respect to the line cycle. A calibrated Ramsey experiment (compare chapter 10) was used to determine line synchronous frequency shifts. The shift is expressed as a magnet field deviation δB_0 , assuming a sole contribution of the B-field modulation to line synchronous frequency shifts. This measurement could be used as a template for a counteracting field generated by a synchronized current signal through the offset coils using a programmable current source. This can be used to cancel the mains induced shift. Such a B-field feed-forward system is in preparation for the described setup.

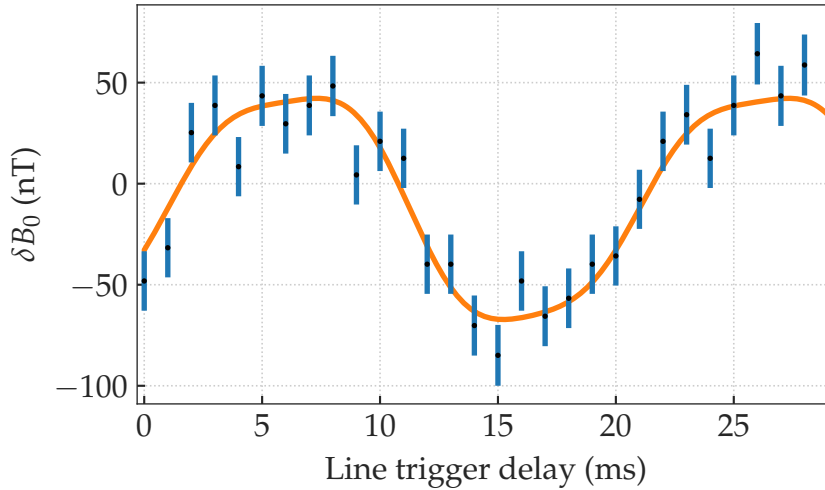


Figure 5.2: Measurement of line synchronous magnetic field noise. The amplitude of B-field deviations is derived from the frequency shift of the $|S_{1/2}, -\frac{1}{2}\rangle \leftrightarrow |D_{5/2}, -\frac{5}{2}\rangle$ transition relative to a delay of sequence to the line-trigger. The frequency shift was determined in a Ramsey sequence with $50\ \mu\text{s}$ dark time. Error bars reflect the QPN of the measurement. The data is fitted with a sum of sinusoidal functions with the first three 50 Hz harmonic frequencies. The major contribution is the 50 Hz amplitude of $59(4)$ nT.

Experimental control

The realization of quantum mechanical experiments on ion crystals described in this work requires several synchronized precisely timed tasks like laser pulses, fluorescence detection etc. At the heart of the setup, a field-programmable gate array (FPGA)-based sequencing hardware (*sequencer*) handles the interaction with all these devices [104, 122]. Its main components are a DAC card¹, a combined DAC, counter and digital input/output card² as well as a stack of sequencer programmable direct digital synthesizer (DDS)³. The sequencer's clock frequency of 100 MHz as well as the DDS clock frequency of 800 MHz is referenced to the Cs-fountain-steered 10 MHz maser signal, which is provided by the time and frequency division of Physikalisch-Technische Bundesanstalt (PTB). User interaction is accomplished with a LabView⁴ based graphical user interface⁵ and sequence control scripts written in Python. A virtual Python server, running in the background, translates the output of the Labview program to FPGA code and handles data exchange with the sequencer.

6.1 Laser control

Most of the lasers described in chapter 8 have at least one acousto-optic modulator (AOM) in their beam path. They are used for switching the light, steering its frequency and controlling its intensity via the sequencer's DDS channels. The individual DDS signals are fed through variable gain amplifiers into the AOMs. For all laser beams, despite the ionization and ablation lasers, an intensity stabilization is installed. It consists of a pickup photodiode close to the vacuum chamber and a control loop. A sample and hold controller adjusts the amplifier gain so that the photodiode signal matches a reference value. The sample pulse timing as well as the set-points are sequencer controlled. A short time window at the beginning

¹ PCI-6703, National Instruments

² PCI-6733, National Instruments

³ based on AD9910, Analog Devices

⁴ National Instruments

⁵ QFP

of each sequence is used for this intensity stabilization. The intensity suppression via AOMs is not sufficient for experiments with long interrogation times. Therefore, additional mechanical shutters⁶ are installed in the beam-paths of 397 nm, 854 nm and 866 nm lasers.

6.2 Sequences

Each experiment consists of several building blocks, a typical example is displayed in fig. 6.1. All sequences contain at least

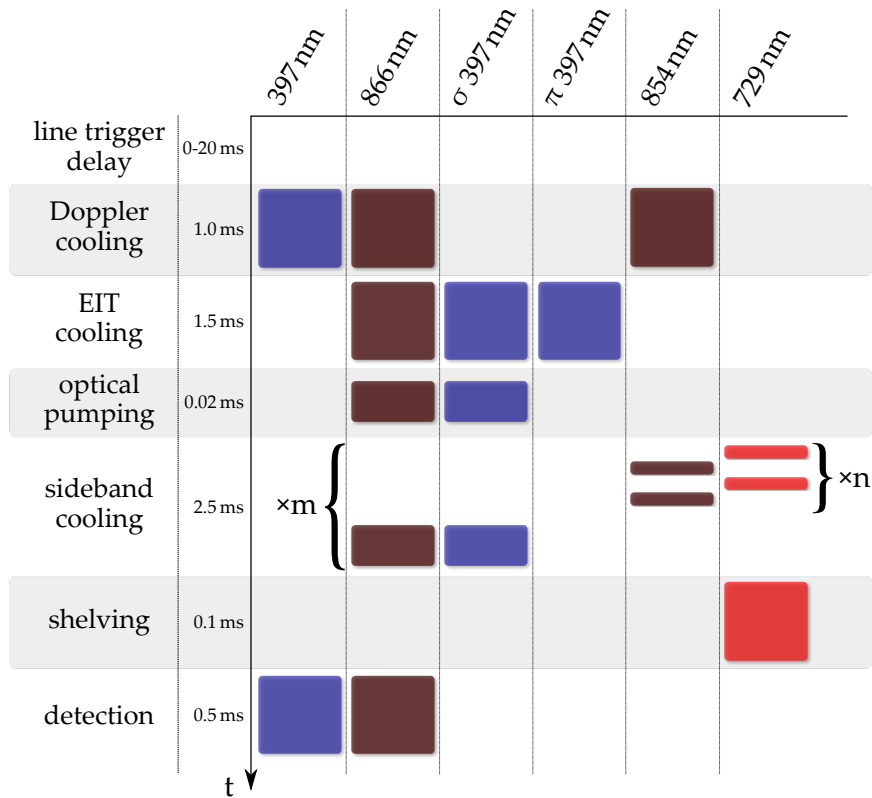


Figure 6.1: Sketch of a spectroscopy pulse sequence. Typical durations of the individual building blocks are shown. Sideband cooling consists of $n \times m$ 729 nm pulses alternated with clear-out 854 nm pulses. After each n^{th} pulse, optical pumping is performed. In the shelving block, various experiments are possible. At its end, a chosen state is projected into a basis, from which a bright/dark state discrimination is performed during detection. The whole sequence is repeated in order to extract the excitation probability.

one detection event at which the fluorescence of the ion is detected on the photomultiplier tube (PMT) and/or camera

⁶ SR474, Stanford Research Systems

(chapter 9). Quantum-mechanical measurements are inherently probabilistic, therefore the same sequence is repeated several times and the excitation probability of the electronic state of the ions is computed within the experimental control program. This number of repetitions (*cycles*) with the same parameter set per data point determines the statistical uncertainty and QPN of the data point.

Ac-mains synchronous magnetic fields are among the biggest perturbations of the system (section 5.2). For sequences with interrogation durations $t \ll 1/50$ Hz, line broadening effects are avoided by starting the sequence line-synchronous.

Occasionally, invalid data points are taken. This happens if e.g. the cooling laser stabilization is interrupted or a high energetic background gas collision occurs and the in-sequence cooling time is not sufficient to reach normal operation state. These states are easily identified by low ion fluorescence detected after normal cooling. Thus, each sequence contains a state monitoring detection window to detect these events (not shown in fig. 6.1). Invalid data is automatically erased and the measurement is repeated. Simultaneously, a far detuned cooling *helper* beam is used for faster re-cooling.

Rf-field coils

In part IV of this work, the application of a continuous dynamical decoupling technique is presented. This technique requires near-resonant coupling between the Zeeman sub-levels of the $^2S_{1/2}$ and $^2D_{5/2}$ levels (compare section 8.1). Therefore, two individually controllable magnetic fields in the rf-domain are required. The desired suppression of frequency shifts is determined by the amplitudes of these fields (chapter 13), and therefore strong rf-drives are advantageous. In addition, the field amplitude should be stable over time to avoid additional frequency shifts (section 14.3.2).

Unfortunately, no suitable, unfiltered signal line on the trap-chip was available for this purpose. Therefore, the envisioned coupling strength on the order of a few 100 kHz (compare section 13.1) for the $^{40}\text{Ca}^+$ transitions requires a resonantly enhanced signal from outside the vacuum vessel. Two separate signal coils are positioned in an inverted view-port opposing the imaging system for minimizing the distance to the ion crystal (see fig. 8.9). The radiating coil consists of a resistor-inductor-capacitor circuit (RLC), with the inductor coil transmitting the desired signal. A primary coil is used to couple the signal inductively into the RLC-circuit, as well as matching the impedance to the $50\ \Omega$ signal source. This radiative coil is formed of a cylindrically wound copper wire, held by a 3D-printed, mesh like polylactide (PLA) holder. Its dimensions are chosen to maximize the coil diameter without blocking the optical access to the trap. Most of the copper wire is exposed to air to avoid heat build-up. A trimming capacitor¹ with low temperature coefficient² is used to fine tune the resonance frequency. Its capacity adds up with the self-capacity of the wire-wound inductance coil. In order to reduce the latter, the wires were separated by small gaps. The resonance frequency

$$\omega_0(T) = \frac{1}{\sqrt{L(T)C(T)}}$$

¹ Type 5453, Johanson Manufacturing

² $\frac{\Delta C}{\Delta T} \frac{1}{C} = 50(50)$ ppm/ $^{\circ}\text{C}$

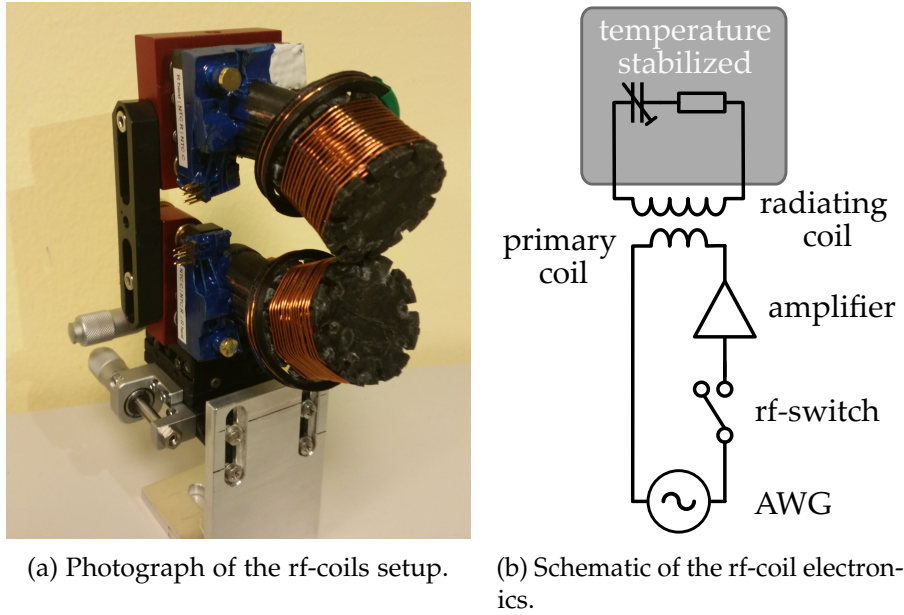


Figure 7.1: Rf-coils overview.

inherits the temperature dependency of the capacitance C and inductance L of the used parts. A flatter resonance spectrum, thus a lower quality factor

$$Q = \frac{\omega_0}{\Delta\omega_0} = \frac{1}{R} \sqrt{\frac{L}{C}},$$

with resistance R is advantageous. This reduces temperature change-induced drifts of the radiated B-field amplitude caused by a change in resonance frequency. An additional resistor was added to reduce the quality factors to $Q_S = 8.59(3)$, $Q_D = 15.95(4)$. The quality factor was only reduced enough to still reach the envisioned coupling strength. The circuits are placed on separate kinematic mirror mounts. The capacitive and resistive parts are glued with thermally conductive epoxy³ to the mount's baseplate together with a heating resistor and temperature sensor for temperature stabilization. A two channel temperature controller⁴ is used to stabilize the temperature of the two RLC-circuits separately. Additional alignment freedom is guaranteed by mounting both coil assemblies onto two translation stages. With this, both coils can get positioned independently to minimize the spatial inhomogeneity of the coil fields at the ion position (compare section 15.2).

³ 2850KT, Stycast

⁴ TEC-1161-4A, Meerstetter Engineering

7.1 Rf-Waveform

Each RLC is fed by an inductively coupled in-coupling coil, which is supplied via an amplifier⁵ with the signal of a dual-channel arbitrary waveform generator (AWG)⁶. Sequencer controlled rf-switches between AWG and amplifiers ensures precise timing of the rf-signals with respect to the laser pulses (fig. 7.1b). The two AWG channels are tightly synchronized internally with the clock derived from a stable 10 MHz reference. The waveforms are pre-computed and uploaded to the memory of the AWG. The start of a dual waveform is then triggered by a sequencer transistor–transistor logic (TTL) signal. The used waveforms are summarized in appendix C. A short-coming of

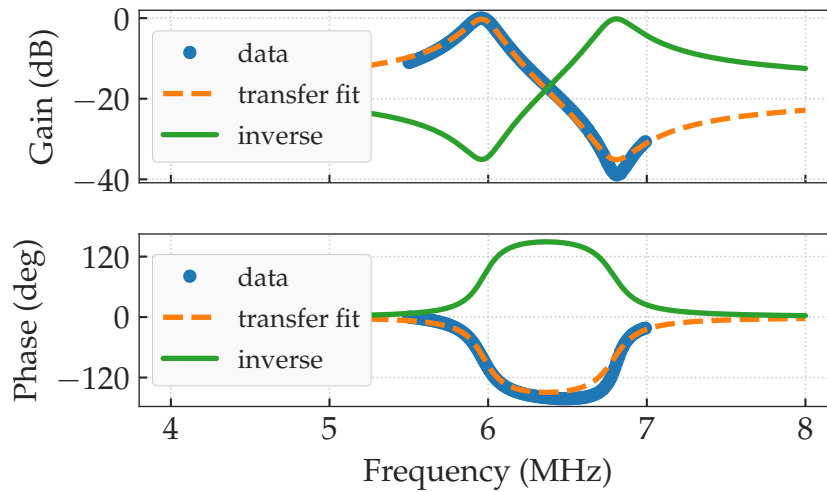


Figure 7.2: Bode diagram of the D coil transfer function. The transmission amplitude and phase were measured with the help of a pick-up antenna and a network analyser. The data (blue) was modelled using a conjugate two poles, two zeros transfer function (orange). For pre-compensation of the signal distortion, the inverse transfer function (green) is applied. Its calculated gain and phase spectrum is scaled for maximal unity gain to avoid unstable behaviour.

the resonant coil design is the signal distortion, especially of the needed modulated waveforms (eq. (C.4)) by the coil's transfer function $H(s)$. For the parameters specified in part IV, the width of the coil resonance is comparable to the modulation frequency. Therefore, the filtering effect of the coil's transfer function would cause a potentially asymmetric and phase shifted distortion of

⁵ ZHL-3A, Mini-Circuits

⁶ 33622A, Keysight

the modulation. In order to circumvent this, the target waveform was transformed digitally⁷ by the inverse transfer function $H^{-1}(s)$ to pre-compensate the distortion. The transmission amplitude and phase of each coil were measured with a pick-up antenna, and the data was modelled using the transfer function

$$H(s) = g \frac{\prod_i (s - z_i)}{\prod_j (s - p_j)} = g \frac{(s - z_r + iz_i)(s - z_r - iz_i)}{(s - p_r + ip_i)(s - p_r - ip_i)},$$

with a complex conjugate pole p_j and zero z_i pair with real z_r, p_r and imaginary z_i, p_i valued coefficients and gain g as fitting parameters. The residuals of the approximative function are flat within $|\frac{\Delta P}{P}| < 10\%$ and $|\frac{\Delta \phi}{\phi}| < 5^\circ$ in a region of ± 200 kHz around the resonance frequency (fig. 7.3). Therefore, the distortion is suppressed compared to the uncompensated case. As the inverse function is unstable, it is scaled below a gain of 0 dB over the whole spectrum to avoid amplified ringing effects (compare fig. 7.2). Deviations arise from the over simplified model and

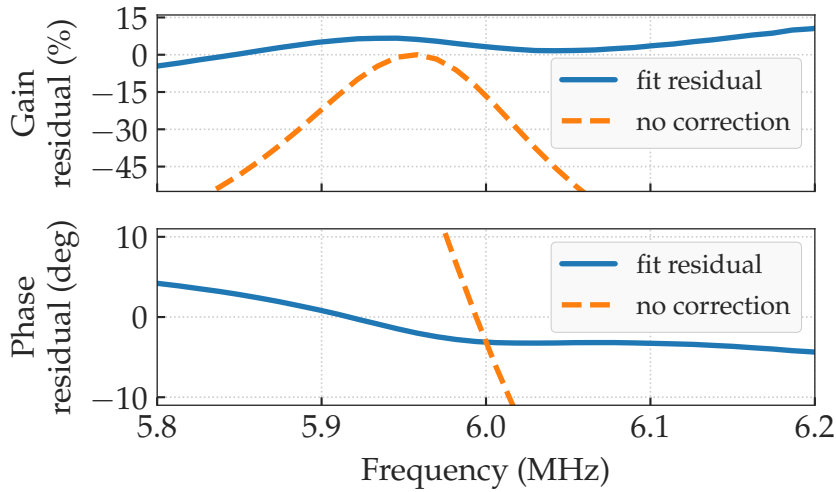


Figure 7.3: Bode plot of the residuals of the approximating model transfer function of fig. 7.2. The curves for gain and phase residuals (blue) of model function and data are compared with the uncorrected data (orange) within the frequency region of interest around the coil's resonance frequency.

the error-prone pick-up antenna measurement. Due to the laboratory wide near-field of the used radiation (around 6 MHz and

⁷ using the python function *dlsim* of the *scipy.signal* module

10 MHz) in combination with the large amount of conducting materials nearby, measurements with a pick-up antenna are sensitive to local displacements and rotations. In the future, a suitable measurement of the gain function with a trapped ion as sensor should lead to more precise results.

Laser system

In this chapter, the laser system for operation of the $^{40}\text{Ca}^+$ setup is presented. In section 8.1, the purpose of the individual lasers is summarized. First, ablating and ionization of neutral calcium (section 8.2) is required for loading ions into the Paul trap. Frequency stabilization of the required cooling lasers is summarized in section 8.3. The stabilization of the quantum logic laser at 729 nm is covered in section 8.4. The optical setup for manipulating the cooling beams and their delivery to the ion trap is covered in detail in [49, 50], so only the configuration around the vacuum vessel is presented in section 8.5.

8.1 Calcium

$^{40}\text{Ca}^+$ is a widely used species in ion trapping experiments. The $^2\text{S}_{1/2} \leftrightarrow ^2\text{P}_{1/2}$ transition at 397 nm is well suited for fast Doppler cooling (section 11.1.1) with only one additional laser at 866 nm needed to avoid population trapping in the metastable $\text{D}_{3/2}$ state. State preparation in the $|S_{1/2}, -1/2\rangle$ level is done with a dedicated, axially aligned σ^- -polarized 397 nm beam (*optical pumping*). With electromagnetically induced transparency (EIT) cooling, the Λ -shaped transitions between $|S_{1/2}, \pm 1/2\rangle$ and $|P_{1/2}, -1/2\rangle$ are exploited to improve cooling by suppression of carrier transitions (section 11.1.3). The metastable $^2\text{S}_{1/2} \leftrightarrow ^2\text{D}_{5/2}$ transition with lifetime $\tau = 1.168(7)$ s [5] allows further cooling by resolved sideband cooling (SBC) (section 11.1.2). In addition, this narrow linewidth transition can be used for various diagnostic measurements via the electron shelving technique [11]. The transition is used as clock transition [18] as well as optical qubit in quantum information experiments [105]. With a laser at 854 nm, the population in the $^2\text{D}_{5/2}$ level is returned to the ground state via the fast decaying $\text{P}_{3/2}$ level.

8.2 Ionization and loading of neutral ^{40}Ca

Loading of an ion into a Paul trap requires two steps. First, a small amount of neutral calcium atoms is evaporated from

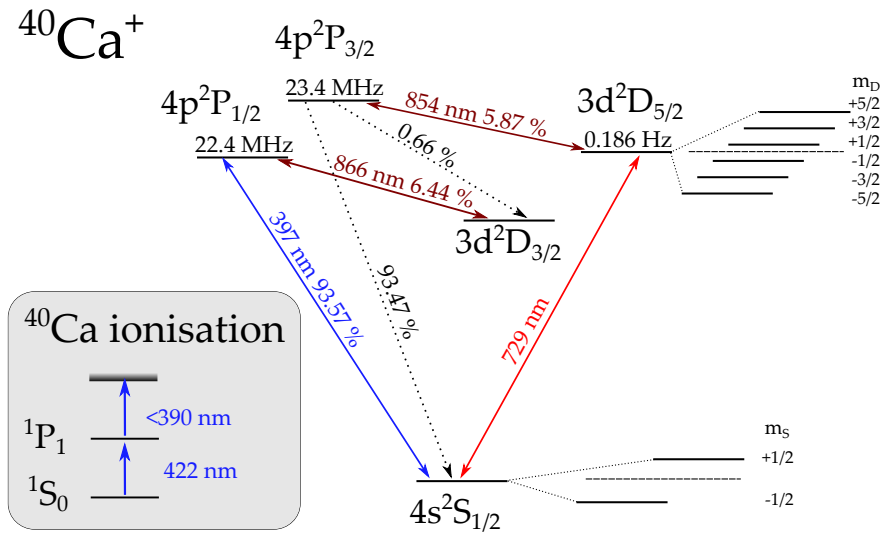


Figure 8.1: $^{40}\text{Ca}^+$ level scheme. Relevant atomic levels are displayed with their natural lifetimes as well as transition frequencies and branching ratios between different levels. For the metastable $^2S_{1/2} \leftrightarrow ^2D_{5/2}$ transition, the Zeeman splitting in an external magnetic field is shown. The laser frequencies utilized for photo-ionisation of neutral ^{40}Ca are indicated. The scheme is adapted from [103].

a macroscopic solid sample. In the presented setup, ablation loading [54] is used. Here, energetic laser pulses evaporate atoms from the solid. For this purpose, a Q-switched frequency-doubled Nd:YAG laser¹ is used. The intensity of the laser is adjusted for loading a single ion with a few shots. In this regime, multi-photon ionization of ^{40}Ca by the ablation laser is unlikely. The neutral atom beam is collimated by an aperture before entering the trapping region. There, the Ca atoms are ionized with a two-step process. The first step excites the atom to the $1P_1$ level with an external cavity diode laser (ECDL) at 422 nm. A second diode laser with wavelength $\lambda < 390$ nm ionizes the atom. Both laser beams are delivered via the same fibre to ensure high spatial overlap. They propagate axially at an angle of approximately 45° with respect to the neutral atom beam. The advantage of ablation loading over resistive heated ovens is fast loading without warm-up times [45]. In addition, a smaller amount of atoms is evaporated, resulting in lower contamination of the trap electrodes, less residual gas in the vacuum vessel and no significant heating of the trap. Also, the ionization lasers illuminate the vacuum chamber only for a short period, reducing stray charges caused by photoelectric emitted

¹ Minilite 1, Continuum

electrons from intense ultraviolet beams. As a downside, precise control of the incidence spot is required for ablation loading. Local erosion of the target surface forces occasionally altering the incidence spot. Therefore, a stepper-motor controlled tilt-able mirror is used. More details about ablation loading in the setup can be found in [49, 50].

8.3 Wavelength meter frequency stabilization

For reliable cooling and fluorescence detection, the involved lasers need a frequency accuracy and stability well below the linewidth of the addressed transitions. For transitions involved in Doppler-cooling, a stability on the order of few MHz is sufficient. The short-term linewidth of the used ECDLs² is mostly determined by optical design and low-noise driving electronics. For longer times, external feedback is required to keep the laser at a certain frequency. All lasers except for the second stage ionization laser and the quantum logic laser at 729 nm are frequency stabilized by commercial wavelength meter³. With this, peak-to-peak fluctuations of $\Delta\nu_{PP} \approx 1$ MHz for a timescale of several hours were achieved [49, 50]. Long term drifts of the wavelength meter (WM) are compensated by calibrating it to the 729 nm laser which is referenced to a highly stable reference laser (section 8.4.4)[89]. Despite the limited resolution of the wavelength meter, the delays by sequentially probing and steering the individual lasers is a limiting factor for the locking bandwidth. Two fibre switches are used to handle the cyclic exposure by different wavelength. Typically, exposure times are kept below 20 ms per channel to ensure fast cycling times. The WM stabilization offers some benefits over alternative schemes like e.g. Pound-Drever-Hall (PDH) stabilization to individual reference cavities. The setup is conceptually simpler, more flexible and takes less space. Even with cavity-referenced lasers, a WM is typically required to identify the desired cavity mode. Laborious thermal shielding of the reference cavities to avoid thermal fluctuations is not necessary. Nevertheless, WM stabilized lasers typically suffer from higher short term fluctuations. But this poses no serious limitation, as shown in section 11.1.1 and section 11.1.3.

² DL Pro, Toptica Photonics

³ ANGSTROM WS/U-10U, High Finesse

8.4 Clock laser setup

High resolution spectroscopy of the $^2S_{1/2} \leftrightarrow ^2D_{5/2}$ transition in $^{40}\text{Ca}^+$ requires a narrowband laser at 729 nm. The operation as optical frequency standard tightens these requirements even more with respect to laser-stability over longer timescales. The WM-lock described in section 8.3 is not sufficient for this task. Instead, a two-step frequency stabilization is used. In the first step, the laser is stabilized with large bandwidth to a medium finesse cavity. In a second step, the light is transfer-locked to a frequency comb for improved long-term performance as well as comparability to PTB frequency standards.

Addressing a narrow quadrupole transition requires a larger optical power compared to the dipole allowed transition. In addition, the stabilization branches of the setup demand a part of the available light. So the use of a high power laser is expedient. A commercial tapered amplifier ECDL system⁴ is used for this purpose. Compared to e.g. a Ti:Sa laser system, this provides a smaller footprint together with potentially lower maintenance overhead at the cost of larger high frequency noise.

8.4.1 Optical setup

The optical setup is separated into three main parts (see fig. 8.2). A portion of the light is used to reference the WM, the rest is fed into the tapered amplifier. The output of the amplifier of $P_{\text{out}} \gtrsim 350 \text{ mW}$ is sufficient for the envisioned task. The majority of the laser intensity is dedicated for the experimental branch. Here, the beam passes a double pass AOM (AOM 3) for frequency steering to the ion's resonance. After a mode cleaning fibre, another two AOMs (AOM 1, 2), with a small net frequency shift are passed. The latter are dedicated for driving bi-chromatic Mølmer-Sørensen gates, which is not covered in this work. They are driven with constant frequencies for all experiments presented in this work. These three AOMs are driven by sequencer-controlled DDSs. With a multichannel fibre switch⁵, the light is guided to the ion from three directions (compare fig. 8.9). Each branch features a polarizing beamsplitter (PBS) for polarization cleaning followed by a $\lambda/2$ -waveplate and a focusing lens. An intensity stabilization photodiode is installed for the axial and diagonal port.

⁴ TA Pro, Toptica Photonics

⁵ EOL 1x4, LEONI

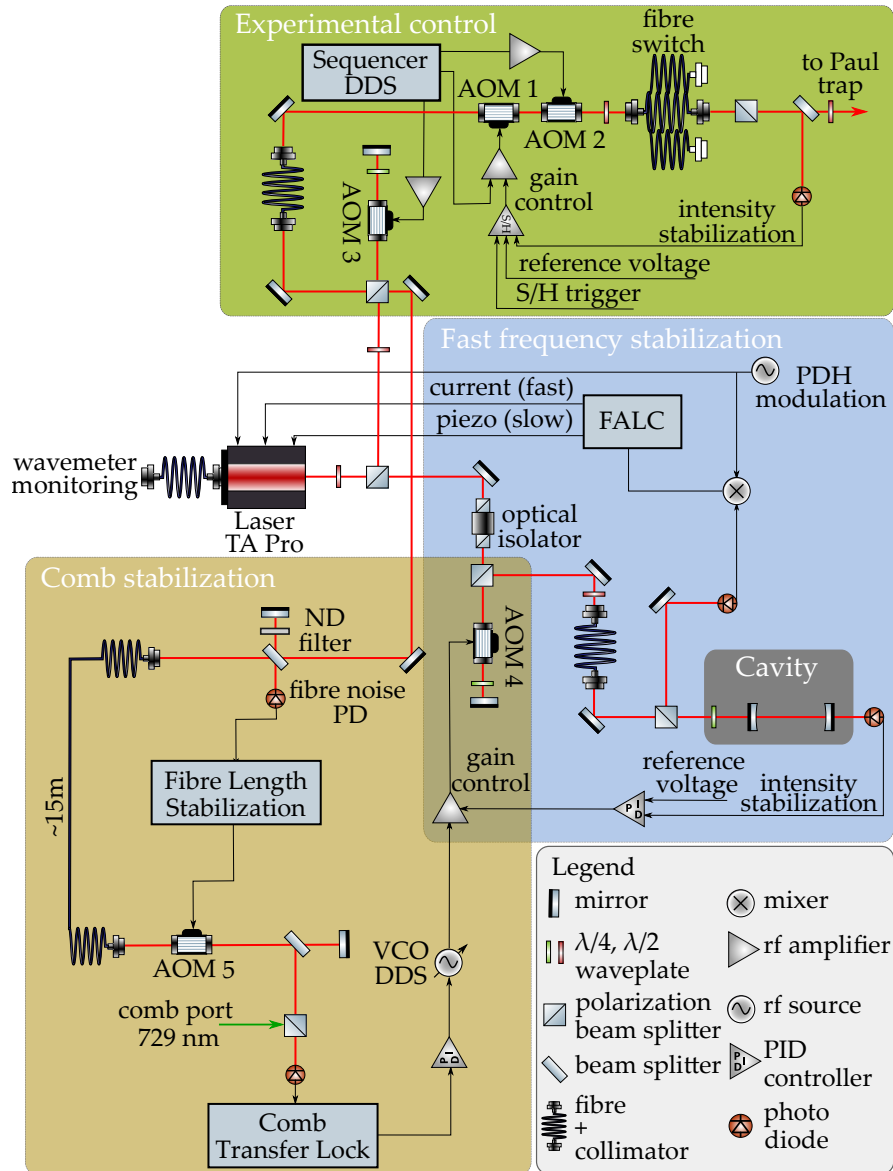


Figure 8.2: Simplified 729 nm laser setup. Only relevant optical elements are displayed. Additional beam steering mirrors, lenses and polarization optics are not displayed for simplicity. AOM beam deflection is not indicated, but the 0th-order is blocked consequently. Some component representations here and in later figures are adapted from [39].

The different beam directions are utilized for micromotion compensation (section 11.3.1), secular mode analysis and addressing of Zeeman transitions with distinct selection rules (compare chapter 10).

The second branch is dedicated to fast frequency stabilization via PDH to an optical resonator (*cavity*). AOM 4 decouples

the resonance frequency of the cavity from the laser frequency in the other branches. It also enables independent frequency steering by the comb stabilization (section 8.4.4). In addition, the amplitude of its driving rf-amplifier is controlled by the cavity transmission intensity stabilization.

The comb stabilization branch consists of a fibre length stabilization setup (section 8.4.3) to the neighbouring laboratory using AOM 5 and an optical beat with the dedicated comb port. The control signal from the comb beat is fed back onto a custom dc voltage steerable DDS (VCO-DDS) driving AOM 4.

8.4.2 Pound-Drever-Hall frequency stabilization

The power spectral density of a typical diode laser contains relevant contributions at Fourier frequencies in the range from dc to 10 MHz. This fast frequency noise sets the bandwidth requirement for the employed laser frequency stabilization. The transfer lock to a frequency comb as described in section 8.4.4 typically involves larger delays preventing high bandwidth control loops [121]. Therefore, the faster PDH pre-stabilization to an optical resonator is advantageous.

For this, an optical resonator (*cavity*) is used as length reference. The resonator setup is described in [50, 131]. It consists of a planar-concave highly reflective mirror pair. The mirrors are optically contacted to a cylindrical ultra low expansion glass spacer with length of $L = 10$ cm and a mirrors' finesse of $\mathcal{F} = 11\,013(22)$. The spacer rests on four polyetheretherketon (PEEK) posts which are mounted on a heat shield. It is surrounded by a vacuum chamber, pumped by a 2 L s^{-1} ion pump, reaching a pressure of $P < 1 \times 10^{-7}$ mbar. For temperature stabilization, the chamber is placed on thermoelectric cooler (TEC) elements inside another heat shield. The whole setup including the surrounding optical elements is placed on a passive vibration isolation platform⁶. It is connected via a polarization maintaining (PM) fibre to the rest of the setup.

The Pound-Drever-Hall technique allows high bandwidth frequency stabilization of laser light (compare fig. 8.3). By using the reflection on the cavity's input mirror, the acquired feedback signal is not bandwidth limited by the cavity's transfer function. The feedback signal is generated by a homodyne detection of the reflected light with a high bandwidth photodiode. Phase

⁶ 250BM-1, Minus K

information is obtained by interference of the carrier signal with phase modulation sidebands. By demodulating the photodiode signal with the modulation signal, a feedback signal with an approximately linear frequency discrimination at the position of the cavity resonance is generated. More details about the PDH technique can be found in [10, 29].

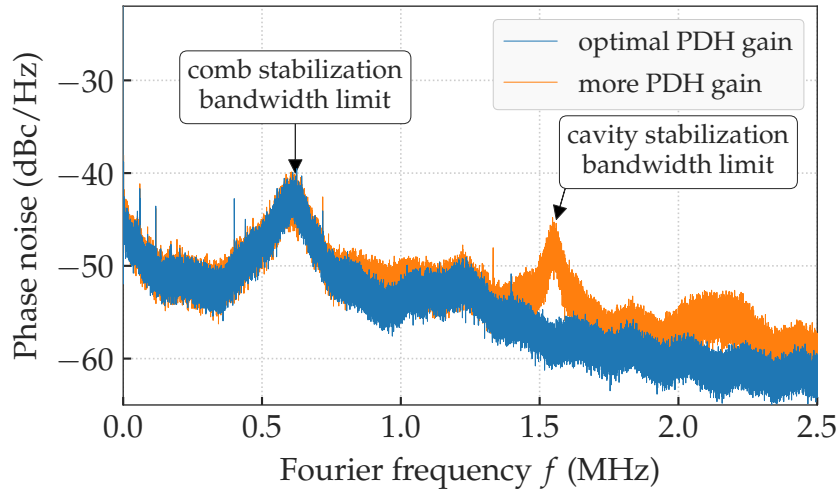


Figure 8.3: Phase noise spectrum of the virtual beat-note of the 729 nm transfer stabilization. In order to differentiate the bandwidth of the comb and cavity stabilization, two traces are recorded with altered PDH controller gain. The peak at Fourier frequency $f \approx 0.6$ MHz marks the bandwidth of the stabilization of the comb to the reference laser. The one peak at $f \approx 1.5$ MHz reflects the PDH stabilization limit.

The 729 nm laser can be frequency steered by a piezoelectric actuator acting on the feedback grating angle, the laser diode driving current and its temperature. The presented stabilization scheme uses the grating angle as slow stabilization path with large frequency tuning range and fast current modulation as fast feedback path. A second current modulation port is used for modulation of the light with the PDH-modulation frequency. Generation of the modulation signal of $f_{\text{mod}} = 20$ MHz as well as its demodulation and phase adjustment is done with a dedicated module⁷. A fast analogue controller⁸ filters the feedback signal and feeds two distinct error signals to a slow path via the laser controller⁹ and a fast path using a dedicated current mod-

⁷ PDD 110, Toptica Photonics

⁸ FALC 110, Toptica Photonics

⁹ DLC pro, Toptica Photonics

ulation input. The control loop filters are optimized for high locking bandwidth $f_c \gtrsim 1.5$ MHz (see fig. 8.3). The achievable bandwidth limit is caused by the accumulated delays along the optical and electrical signal path. Beside the delay along the approximately 5 m long signal loop, phase delay in the electrical components e.g. filters are the main contribution. Applying the PDH-modulation signal to the laser diode, instead of using a dedicated phase modulation electro-optic modulator (EOM), has the disadvantage of a parasitic amplitude modulation causing set-point variations. A dedicated EOM was built into the setup in the meantime. A characteristic hump in the power spectral density appears at the Fourier frequency where the phase delay exceeds $\phi > 180^\circ$. Laser noise beyond this is not compensated (fig. 8.3). In order to avoid this remaining high frequency noise contributions, self-injection of the laser-diode with cavity filtered light is a promising approach [71, 148]. Even with an

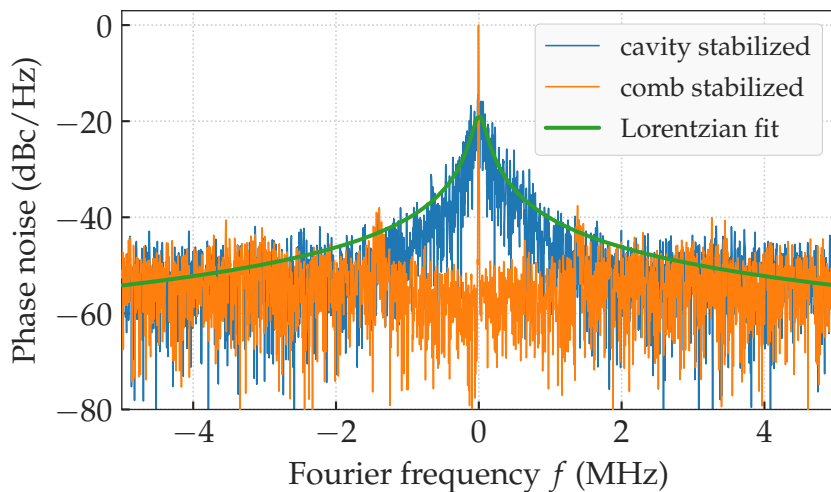


Figure 8.4: Phase noise spectrum of the (in loop) virtual beat-note of the 729 nm laser with enabled (blue) and disabled (orange) controller. The spectrum with disabled controller displays the short-term linewidth of the PDH-stabilized laser. The resolution bandwidth of the used spectrum analyzer $\Delta f_{\text{RBW}} = 10$ Hz results in a sweep rate of $s = 33 \text{ Hz ms}^{-1}$. On this timescale, the unstabilized linewidth can be approximated with a Lorentzian line-shape with width $\Delta\nu_{\text{FWHM}} = 170(4)$ Hz. The peak of the stabilized signal is resolution bandwidth limited. Both traces are normalized to the stabilized peak height. The peaks at $\Delta f \approx 1.5$ kHz are caused by electronic noise. The bandwidth of the transfer-lock stabilization is $f_{\text{BW}} \approx 3$ kHz, which is barely visible on this dataset.

optimal PDH stabilization, the laser frequency is linked to the

cavity length, which is subject to length fluctuations by temperature drifts, vibrational perturbations, intensity noise shifts, fibre length fluctuations and other contributions [46, 93]. The typical linewidth broadening of $\delta\nu \lesssim 200$ Hz at short integration times is compensated by a transfer stabilization to the comb (section 8.4.4).

8.4.3 Fibre length stabilization

At this level of frequency stability, optical path length fluctuations become important. They arise from refractive index changes by temperature or pressure in air and optical elements, especially longer fibres. Also, fluctuations of the geometric path by e.g. vibrating mirror surfaces can be summarized under this category. The magnitude of the spectral broadening by this kind of phase shifts depends primarily on the length of the path and the present perturbation sources.

The bandwidth of the perturbations is typically on the order of kHz, so they can be treated as quasi static compared to the light travel time for medium path lengths. Therefore, a fibre noise cancellation (FNC) [38, 83] can compensate these phase shifts.

A portion of the light through a fibre is reflected back the same path and homodyne detected on an ac-coupled photodiode. An AOM in the beam path generates a frequency offset and is used as frequency actuator. The photodiode signal measures twice the phase deviations accumulated along the path. It is stabilized with a phase-locked loop (PLL) circuit to a stable reference signal (see fig. 8.6). Depending on the requirements and infrastructure, several topologies are possible including multi-point delivery [43] or large distance setups with intermediate amplification [137]. We choose a simple and versatile approach applicable with an extra rf-signal path. A single AOM at the far end of the fibre is used both as phase actuator and enables sure distinction from spurious back reflections. A DDS-chip in conjunction with a voltage controlled oscillator (VCO) is used as versatile phase noise control loop as shown in fig. 8.6.

The performance of the fibre noise cancellation (FNC) is shown in fig. 8.5. In addition, the stability of the unstabilized residual path (from first beam-splitter in Comb stabilization box through experimental control box in fig. 8.2) to the ion trap is shown. Because the light in this path is chopped by a sequencer-controlled AOM, path stabilization would be more evolved and

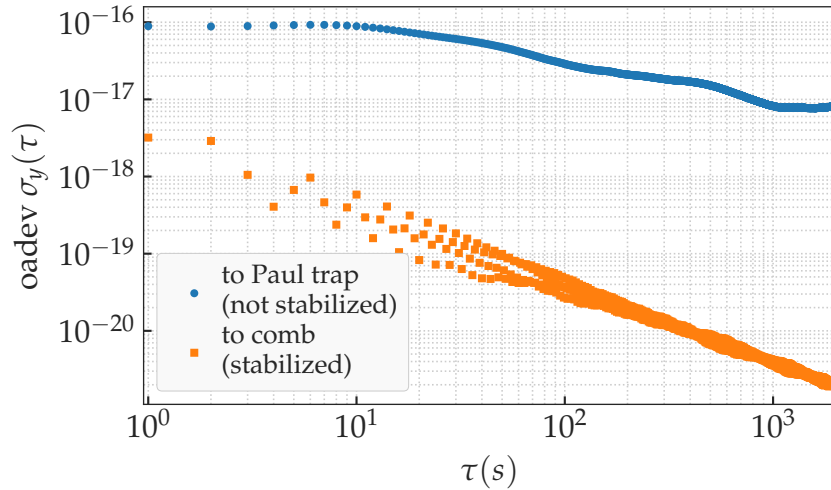


Figure 8.5: Overlapping Allan deviation of in-loop fibre length photodiode signals for two different beam paths. Fractional frequency deviation is calculated with respect to the light frequency. The $L \approx 15$ m path to the frequency comb laboratory (orange) is actively stabilized. The shorter path of approximately 5 m to the ion experiment (blue) is only passively isolated. It passes one fibre, three AOMs and a fibre switch. The visible oscillations in the Allan deviation depicted in orange are caused by jitter in the employed counter module.

was not implemented yet. This measurement was done with a retro-reflector close to the ion position. The optical beat revealed a stability of $\sigma_y < 1 \times 10^{-16}$ for $\tau > 1$ s which is not limiting for the presented experiments.

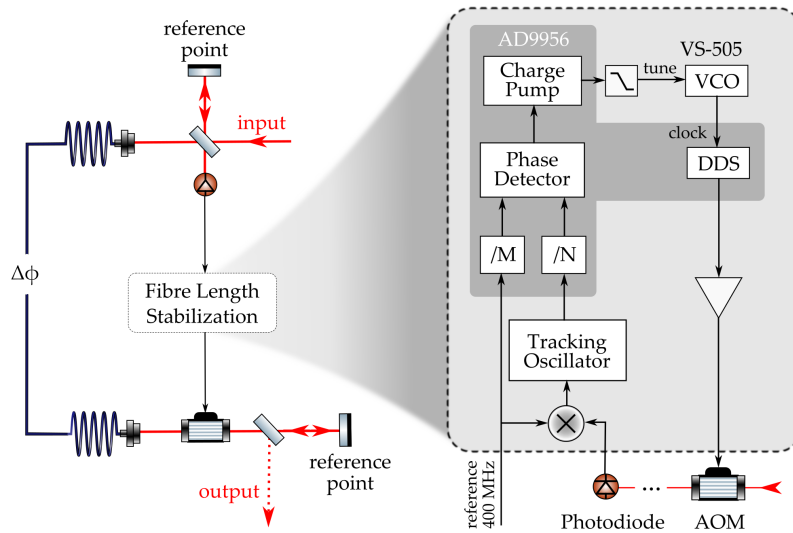


Figure 8.6: Schematic FNC diagram. The phase noise $\Delta\Phi$ accumulated on the path is measured with a self-heterodyne detection on a photodiode. The signal is mixed down and purified with a tracking oscillator and potentially divided by N . Its phase is compared with the divided reference signal on a phase detector. The filtered output of the charge pump is used as control for a voltage-controlled surface acoustic wave oscillator. The output of the oscillator is used as a reference clock for the DDS. The amplified DDS output drives the actuator AOM. Thus, the phase of the DDS is steered to minimize the measured phase differences of the light. This setup has the benefit of flexible frequency choices. Therefore, matching the intermediate signals to the working ranges of AOMs, VCOs and tracking oscillators is easily possible.

8.4.4 729 nm transfer stabilization to fibre comb

Precise measurements of the absolute frequency of laser light in the optical region was barely possible until the end of last century. In 2005, Theodor W. Hänsch and John L. Hall received half of the Nobel Prize in physics

[...] for their contributions to the development of laser-based precision spectroscopy, including the optical frequency comb technique. [98]

Their work made it possible to reference optical frequencies to the definition of the SI-second without the need for inconvenient frequency multiplication chains [125], thus making optical clocks obtainable. A frequency comb generates a strictly periodical pattern in the frequency domain. The spectral distance of the comb's teeth is fixed to a high degree. So it can be used as a frequency ruler for comparison of two optical wavelengths or absolute frequency measurements. This kind of spectrum is produced by mode-locked lasers emitting a periodic train of short pulses. The absolute frequency of one comb tooth is given by

$$f_{abs,n} = n f_{rep} + f_{CEO}, \quad (8.1)$$

with comb pulse repetition rate f_{rep} , tooth number n and the carrier-envelope offset f_{CEO} . The latter accounts for phase offset of the pulse envelope with respect to the carrier frequency. Both frequencies are typically stabilized either directly in the rf-domain or indirectly by stabilizing one comb tooth to a stable reference laser. The latter potentially leads to a better performance, as today, highly stable lasers offer orders of magnitude lower relative phase-noise than their radio-frequency or microwave counterparts. In fact, with a suitable reference laser a low phase noise microwave signal, comparable with the best cryogenic sapphire oscillators, was generated using a frequency comb [133]. With knowledge of the comb frequencies and the difference frequency Δf , acquired from the optical beat-note with a laser under investigation, its absolute frequency is deduced. Only the rough wavelength has to be known in advance to determine the number of the nearest tooth.

The comb teeth typically have a large amount of high frequency noise, so the beat-note comparison is short term limited. This prolongs averaging times for frequency comparisons and makes direct laser stabilization to a frequency comb unfavourable. With the transfer oscillator technique [121, 136],

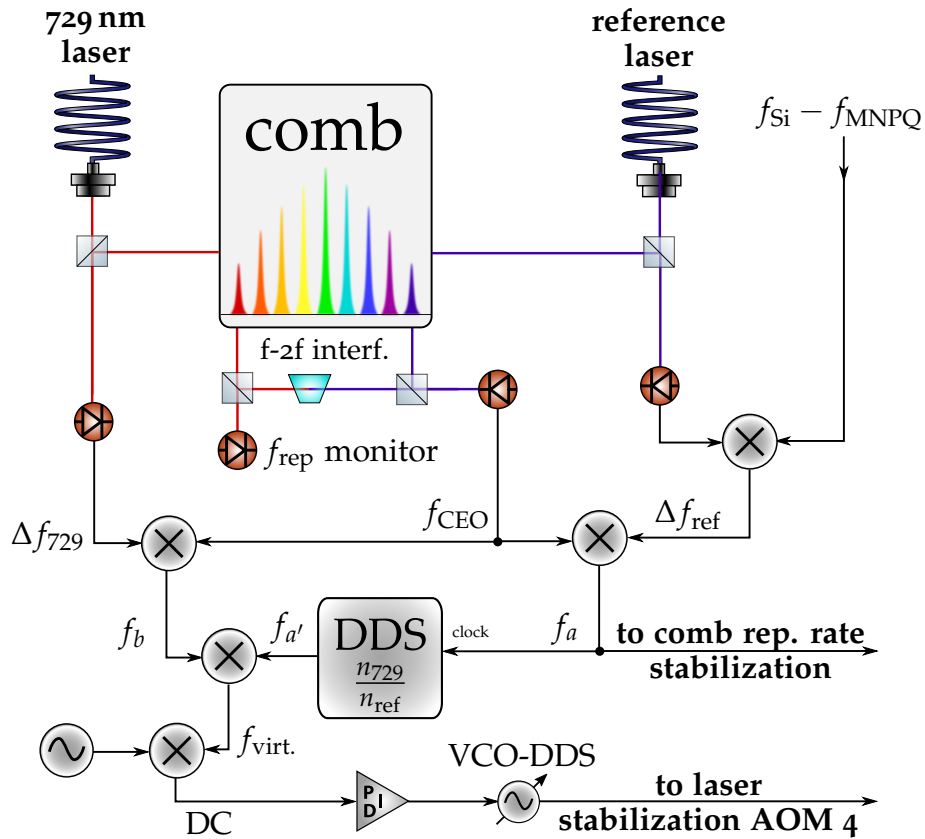


Figure 8.7: Sketch of the transfer-lock laser stabilization. The optical beat notes of 729 nm laser and reference laser with the fibre frequency comb are measured. In order to stabilize the 729 nm light to the reference, the frequency noise induced by the comb is measured and electronically subtracted. Only the relevant steps are displayed. Additional amplification, filtering and mixing electronics are omitted for simplification.

these comb fluctuations are rejected and a virtual, comb noise-free beat-note of the reference laser with the target laser is established. Therefore, the beat-note Δf_{rep} of the comb with the reference laser is measured. This contains information about the instantaneous repetition rate phase $\phi_{\text{rep}}(t)$ excursions. In addition, the instantaneous carrier-envelope offset phase $\phi_{\text{CEO}}(t)$ has to be known. The instantaneous phases of the individual comb modes are tightly linked by the mode coupling mechanism e.g. four-wave mixing. They are given by integrating eq. (8.1) [136]:

$$\phi_n(t) = n\phi_{\text{rep}}(t) + \phi_{\text{CEO}}(t) + \phi_{\text{disp},n}(t).$$

Phase fluctuations of the repetition rate scale with the comb's tooth number n , carrier-envelope offset (CEO) phase noise is common to all modes. The phase $\phi_{\text{disp},n}$ accounts for uncompensated dispersion in the used optical elements. This phase is treated constant for the latter. Fluctuations of this wavelength-dependent phase as well as residual path differences on the way to the individual photodiodes can be compensated with a suitable end-to-end topology [8].

The two absolute frequencies are expressed as

$$\begin{aligned} f_{\text{ref}} &= f_{\text{CEO}} + n_{\text{ref}} f_{\text{rep}} + \Delta f_{\text{ref}}, \\ f_{729} &= f_{\text{CEO}} + n_{729} f_{\text{rep}} + \Delta f_{729} \end{aligned}$$

using the beat-note frequencies Δf_i . These signals are first mixed with the measured carrier-envelope offset signal f_{CEO} (see fig. 8.7). This yields

$$\begin{aligned} f_a &= f_{\text{CEO}} + \Delta f_{\text{ref}}, \\ f_b &= f_{\text{CEO}} + \Delta f_{729}, \end{aligned}$$

removing f_{CEO} and its associated noise contribution.

The reference signal f_a is then scaled with the fraction of the comb teeth numbers. After a last mixing step,

$$\begin{aligned} f_{a'} &= \frac{n_{729}}{n_{\text{ref}}} (f_{\text{CEO}} + \Delta f_{\text{ref}}), \\ f_{\text{virt.}} &= f_b - f_{a'} = f_{729} - \frac{n_{729}}{n_{\text{ref}}} f_{\text{ref}}, \end{aligned}$$

the virtual beat note $f_{\text{virt.}}$ is obtained, which is independent of the combs properties.

This signal can be used for faster frequency comparisons as well as transfer stabilization.

An erbium-doped-fibre frequency comb¹⁰ is used in the presented setup. Carrier-envelope offset is measured with the built-in $f - 2f$ interferometer and stabilized to a fixed value of 40 MHz by feedback to the pump diode current. The stable reference laser¹¹ (*MNPQ-laser*) is transferred via noise-cancelled fibre to the comb laboratory from a neighbouring building. The repetition rate is stabilized with an intra-cavity EOM by fixing the beat-note of the nearest comb line to $\Delta f_{\text{ref}} = 57$ MHz. To benefit from a more stable laser with lower frequency drift

¹⁰ FC-1500-250-WG, Menlo Systems

¹¹ prototype of ORS 1500, Menlo Systems

which is locked to a cryogenic Si cavity (*Si-laser*) [89] we mix in the beat-notes of the two lasers (see fig. 8.7). These lasers are situated in the same neighbouring building, the correction signal is transferred from the other group's laboratory via a twisted wire pair cable. Scaling with the comb teeth number requires the frequency division with a rational number. For this purpose, a DDS chip is used. With singular programming of the frequency tuning word, the ratio of the clock input to the DDS output frequency is set. For the scaling fractions $\frac{n_{729}}{n_{\text{ref}}} = 2.12 > 2$, an aliased frequency component is used. The virtual beat-note is mixed down to dc and is fed into a PID controller¹². Its output voltage steers the clock VCO of a DDS, which is driving AOM 4 (compare fig. 8.2).

Several filters are required to clean the output spectrum from undesired frequency components at the DDS output as well as the mixer outputs. Their total delay limits the bandwidth of the stabilization. With the cavity pre-stabilized laser, the control bandwidth of the PID controller has to be just large enough to take out the residual fluctuations after this stabilization (see fig. 8.4). All relevant signals are permanently measured and recorded with phase-frequency counter modules¹³.

For an independent measurement of the 729 nm stability, the light is transferred via a length-stabilized fibre and measured against another frequency comb (*comb 2*), which is directly locked to the Si-laser. Unfortunately, the available fibre¹⁴ was not suitable for 729 nm, so there was a huge amplitude drift, preventing longer FNC-operation. In addition, a few metres uncompensated fibre was added. Also, the inter-branch comb path fluctuations [8] are not compensated. Therefore, the measurement shown in fig. 8.8 can be treated as an upper limit for the stability of the laser.

The necessity for the transfer stabilization as well as the Si correction can be derived from fig. 8.8. The 729 nm comb stabilization, a measure for residual cavity fluctuations, as well as the difference of Si- and MNPQ-laser experience a drift of $d_{729} = 1.9 \text{ Hz s}^{-1}$ and $d_{\text{MNPQ}} = 14 \text{ mHz s}^{-1}$. This stability is not sufficient for longer spectroscopic measurements e.g. approaching the natural lifetime on the $^2\text{S}_{1/2} \leftrightarrow ^2\text{D}_{5/2}$ transition in $^{40}\text{Ca}^+$. In contrast, the Si-laser achieves a flicker floor stability of 5×10^{-17} for averaging times from 0.8 to 10 seconds and

¹² custom device based on Red Pitaya, STEMLab

¹³ FXE, K+K Messtechnik

¹⁴ HB 1000

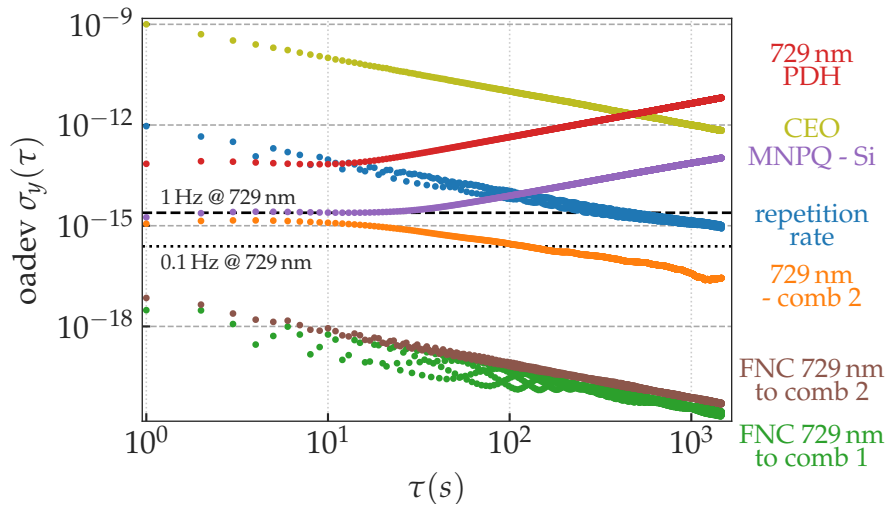


Figure 8.8: Overlapping Allan deviation of the counter data of all relevant signals. All signals are retrieved from associated photodiode signals. They are mixed down and amplified to fit within the counter's bandwidth. A gate time of 1 s was used. The beat-note of the 729 nm laser with comb 2 is the only out-of-loop measurement. For all data, except for the repetition rate and CEO, the fractional frequency was taken with respect to 411×10^{12} Hz. The repetition rate was measured at four times the rate at 1 GHz. Comb teeth across the whole comb spectrum contribute to this signal. Therefore, this measurement is only an indicator for the stability of a single tooth. So it is only used for monitoring purpose.

a drift on the order of $d_{Si} \approx 50 \mu\text{Hz s}^{-1}$ [89, 94]. This known frequency drift is compensated in the presented setup, by ramping the frequency of the *static* DDS in a mixing step of the transfer lock.

The noisy comb tooth, reflected by the stability of CEO and repetition rate, have to be cancelled by the stabilization. The independent beat-note measurement with the second comb poses a lower limit for the applied transfer lock scheme. One observed technical shortcoming is the division step in the DDS-chip. Its input is not fed with a pure sinusoidal signal rather with the residual comb noise spectrum. In dependence of the signal amplitude, occasionally dropouts have been observed, leading to fringe hops of the transfer stabilization. However, the observed stability of $\sigma_{729\text{nm}} < 1 \times 10^{-16}$ for $\tau > 400$ s is sufficient for the spectroscopy measurements presented in this work.

8.5 Beam configuration

The optical path is described in detail in [50], so only a summary is given here. The light of each laser is frequency steered and shuttered by at least one sequencer-controlled AOM. For the infrared lasers at 866 nm and 854 nm, mainly fibre-based components are used. This allows for an optical setup with small footprint. All components including WM and laser-heads are fitting on three 90 cm \times 60 cm breadboards. Delivery of the beams to the ion trap board is done with PM-fibres.

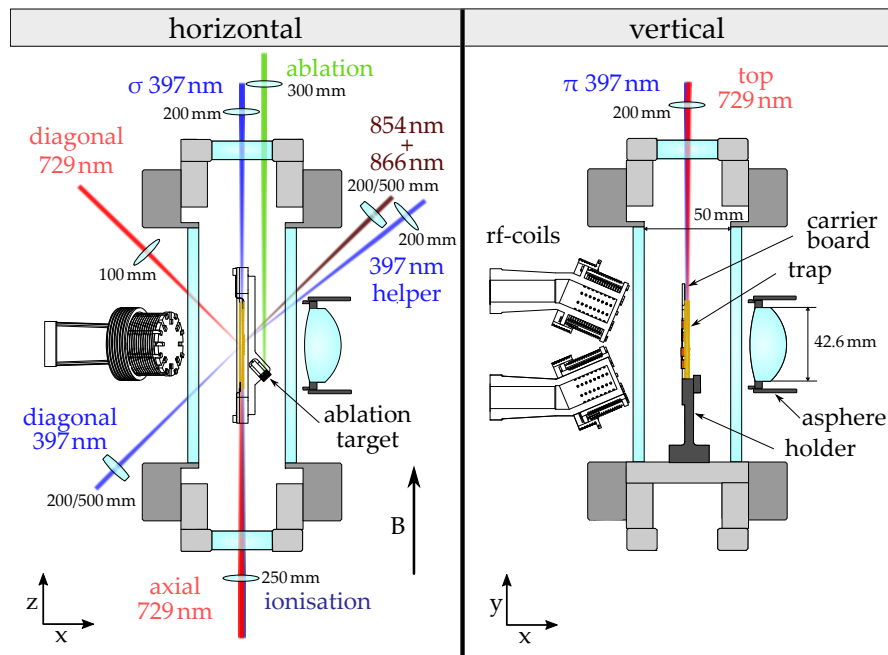


Figure 8.9: Cross-sections of the vacuum chamber setup. The incidence angles of the laser beams with respect to the trap axis and the magnetic field are indicated. The dimensions are true to scale except the laser beam diameters. The focal length of the used focussing lenses are given.

Figure 8.9 shows the laser beams' geometry with respect to the ion trap. With suitable polarization optics after the fibres, the polarization is cleaned and adjusted. A fraction of the light directly illuminates a photo-diode (PD) for intensity stabilization of all paths except the ionization lasers and 729 nm top beam.

Focussing lenses are used to increase light intensity at the ion position and reduce spurious reflections on the trap. As extended ion crystals are investigated (chapter 15), the diagonally applied cooling beams are focused using cylindrical lenses

resulting in axially enlarged beam profiles. This ensures a more even illumination of extended ion crystals.

The incidence angle of the diagonal 397 nm beam is chosen to have a finite projection on all principal axis of motion. The direction and polarization of the σ 397 nm beam is optimized to avoid unwanted polarization components, which would decrease optical pumping yield and cause additional heating after sideband cooling. The diagonal alignment of 854 nm and 866 nm beams is chosen due to spatial restrictions. For state selective clear-out, e.g. to the outermost $^2P_{3/2}$ transition, a defined σ -polarization, and thus axial incidence would be beneficial. The three 729 nm beams allow addressing of all available Zeeman components and the distinct directions allow 3D-probing of the directional micromotion components. The diagonal 729 nm beam is tightly focussed to a beam diameter of $w < 25 \mu\text{m}$ to increase coupling strength for Mølmer-Sørensen gates. The exact determination of the incidence angles of the 729 nm laser beams using their coupling strength with respect to the principal trap axis is shown in appendix B.

Imaging system

State readout of stored ions requires usage of an imaging system. Its purpose is to collect enough photons emitted by the ions to surely differentiate between a bright and dark state. The first is identified by strong fluorescence of 397 nm light, here the transition $S_{1/2} \leftrightarrow P_{1/2}$ is driven and population in $D_{3/2}$ is repumped using 866 nm light. The latter is given if the long-lived $^2S_{1/2} \leftrightarrow ^2D_{5/2}$ transition is excited, but the cooling lasers only cause stray-light but no fluorescence from the ions. With this electron-shelving technique [142], state discrimination approaching 100 % is accomplished.

Beside this dark/bright distinction, the amount of fluorescent light can also reveal information about some properties of the ion crystal and the applied light. For example, the difference of the laser to the transition's frequency is typically optimized with that measure.

Typical distances between ions in a Coulomb crystal are on the order of a few μm . Therefore, the wavelength of 397 nm allows for diffraction limited resolution of individual ions with a high numerical aperture lens without the need for more involved techniques [28, 52]. In the presented setup, a custom-made, bi-aspheric lens¹ optimized for 397 nm light is placed just outside the vacuum vessel in an inverted viewport. The numerical aperture of $\text{NA} = 0.51$ in a minimal working distance of $d_{\text{min}} = 36.6 \text{ mm}$ allows coverage of 7% of the solid angle. More details on the design considerations and characterization of the used lens is found in [49, 50]. The collected light is shone simultaneously onto a scientific complementary metal-oxide-semiconductor (sCMOS) camera² and a PMT³ using a 90/10 beam splitter (fig. 9.1). The imaging path is enclosed to reduce stray light, and an optical bandpass filter⁴ suppresses room light entering from the trap side. Apertures close to the imaging plane reduce stray light at 397 nm from scattering of the cooling beams on the trap.

¹ Asphericon

² PCO.edge 4.2LT, PCO AG

³ H10682-210, Hamamatsu

⁴ FBH 400-40, Thorlabs

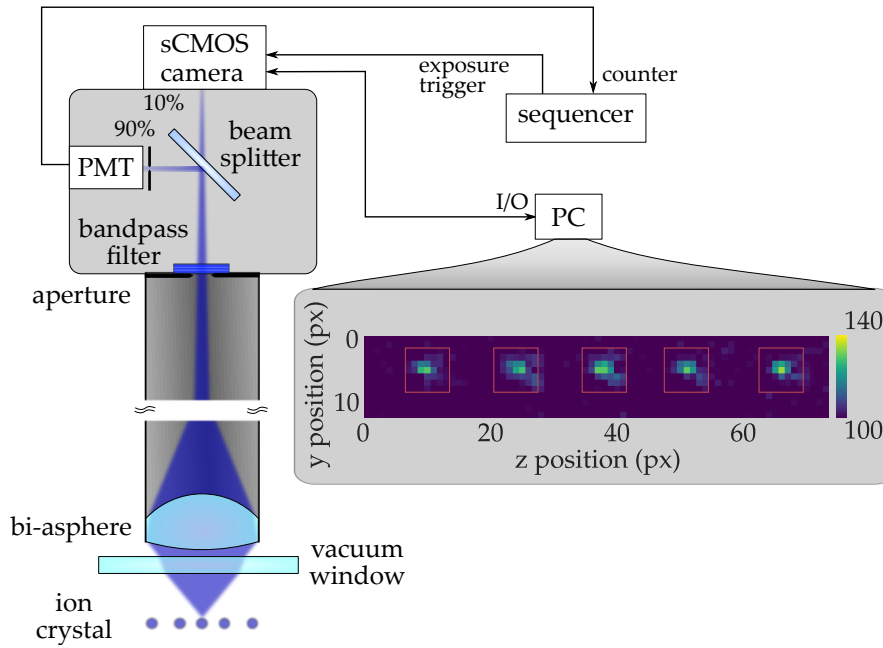


Figure 9.1: Sketch of the imaging system. A bi-aspheric lens outside of the vacuum focusses the collected ion fluorescence onto a sCMOS camera and a PMT. They are housed in a light-tight box containing an optical bandpass filter, apertures and a 90/10 beam-splitter. The PMT is read out using the counter module of the sequencer, which also synchronizes the exposure time of the camera with the detection windows. Camera data is transferred to and analyzed by a computer (inset).

A control computer in combination with the sequencer handles synchronization of the detection windows with the associated laser pulses. PMT-counts are directly recorded by the sequencer's counter input (compare chapter 6). The camera settings and data handling is done using the included software⁵, only the exposure timing is synchronized with suitable TTL pulses by the sequencer. Camera data acquisition is not transferred in real-time, the recorded images are assigned to a particular detection event in post-processing.

9.1 Multi-ion state discrimination

PMT and sCMOS fulfill similar but distinct tasks. Photomultiplier tubes allow fast state readout with relatively high photon count efficiency for the used wavelength as well as low internal background counts. However, they offer no spatial informa-

⁵ pco.camware

tion despite regional filtering by the aperture in the order of $100\ \mu\text{m} \times 30\ \mu\text{m}$. Camera chips in contrast offer the possibility of spatially-resolved information, thus state detection of single ions in a crystal is possible as well as e.g. identification of other ion species within the crystal. Drawbacks, especially from the used camera type, include a low maximal frame-rate⁶ and comparatively large electrical readout noise per pixel. The minimal exposure time to ensure state discrimination is further elongated by usage of an unfavourable splitting ratio between camera and PMT, which will be changed in the future. However, an unresolved short-coming on the camera's acquisition and/or data transfer forces us to choose a usable minimal detection time of $t_{\text{det}} = 10\ \text{ms}$ to avoid data loss due to timing issues caused by the camera's electronic. Because of this effect and the lack of real-time readout, another camera type will have to be installed in the future.

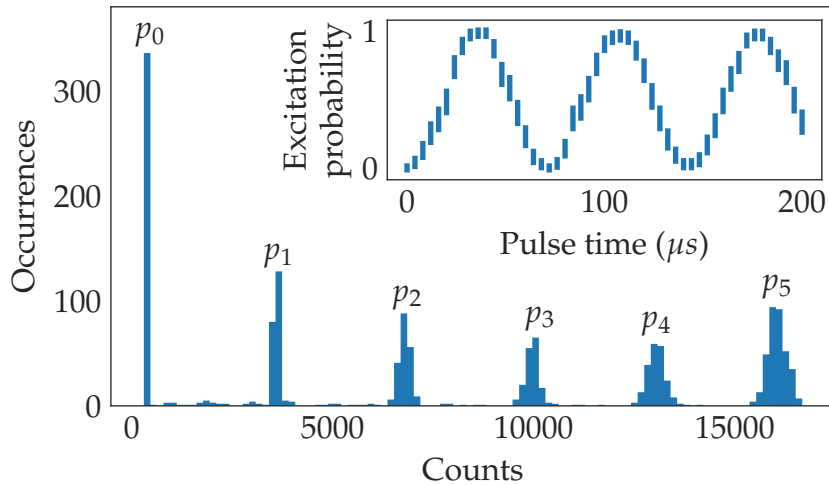


Figure 9.2: PMT count histogram of a five ion crystal with 10 ms detection time. With such a long detection time, the distributions p_i for i bright ions are well separated. Increasing distribution widths for increasing counts are clearly visible. The inset shows the global excitation of the same dataset. A pulse time scan was used to ensure finite excitation contributions for all i . Residual counts between the distributions are probably caused by imperfect cooling after a residual gas collision.

Discrimination of the dark/bright state of an individual ion is often done using the threshold method [53]. Therefore, a histogram for the two states is recorded in order to get a re-

⁶ depending on readout region size, position and binning, compare [102]

alistic, setup-specific photon count distribution. The width of these distributions is mainly given by the amount of collected photons, following a Poisson distribution. Electronic readout noise, laser frequency and intensity fluctuation will broaden the distributions widths. The minimal discrimination error is given if false-bright and false-dark-error are equal. This is approximately attained by placing the discrimination threshold at the intersection of the bright and dark photon distributions. The detection error, for this missattributions are on the level of 0.04 % (fig. 9.3) and therefore neglected. Another detection error arises from state decay during the detection time. For the longest used detection time of 10 ms and the given distributions, this error accounts for 0.6 % false bright detection. The following experiments use the determined threshold for discriminating the state for each detection event. The excitation probability for repeated experiments is given by their mean.

For multiple ions, an extension of the described state discrimination with $N + 1$ thresholds can be done (compare fig. 9.2). But only the number of excited ions can get extracted from measurements using a PMT. The global excitation is given by

$$p_{\text{glob}} = \frac{1}{N} \sum_{n \leq N} n p_n.$$

A limitation for this method is the increasing width of the distributions with increasing count numbers. Therefore, the optimal detection time must be increased to lower the detection error. With increasing detection times, spontaneous decay of the upper state becomes relevant [40], giving rise to a non-Poissonian tail on the dark state distribution, resulting in a larger false-bright-error and therefore, the optimal threshold is altered [113].

For most experiments on multi-ion crystals described in chapter 15, spatial information is very helpful to analyze the inhomogeneous shifts. Therefore, camera data is consequently used. Fluorescence detection of individual ions in a multi-ion crystal requires assignment of pixels of the camera sensor to one of the ions. Therefore, a ROI is placed around each ion's image and the contained pixel values are summed up (compare inlet fig. 9.1). This technique is suboptimal as more pixel than necessary are included, but it is easy to implement and it is robust against small displacements and aberration of the optical elements. With the fixed long exposure time, noise from the extra pixels pose no

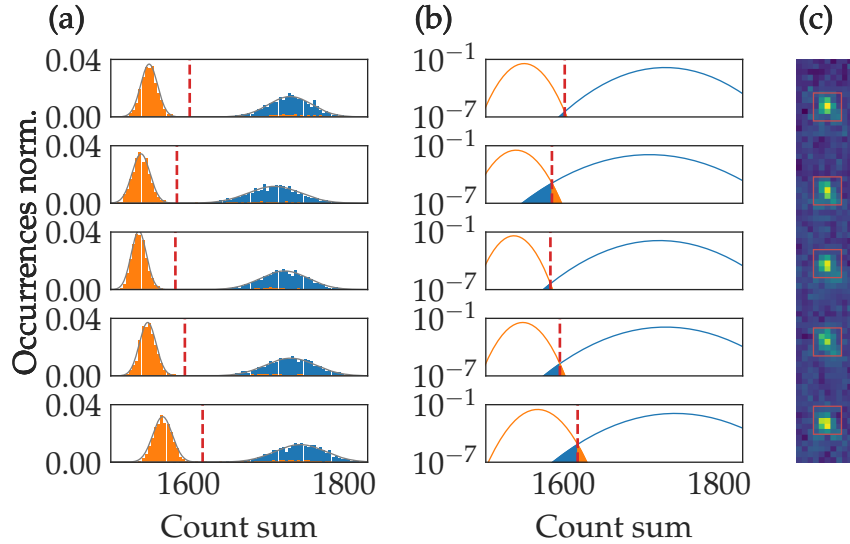


Figure 9.3: **(a)** Histogram of the individual ion's pixel count sums. The dark (orange) and bright (blue) distributions are obtained with a detection time of 10 ms. The distributions were recorded with the 397 nm laser operating close to saturation intensity of the cooling transition. For the dark data set, the ions' states are shelved to the $^2D_{5/2}$ level before detection. The distributions are approximated by a Gaussian function. **(b)** Semi-logarithmic reproduction. The thresholds are set to the intersection of both Gaussian functions. Coloured regions indicate the false bright (orange) or false dark (blue) portions of the distributions. The largest of the individual misattributions accounts for 0.04 %. The offset of the individual histograms is caused by spatial varying background from stray-light and/or pixel array inhomogeneities. The separation between bright and dark distribution means vary by 3 % for the individual histograms, indicating a relatively even laser illumination. **(c)** Mean camera recording with region of interests (ROI) marked in red.

noticeably limitation. Faulty extra counts from neighbouring ions are well below the background level for the separations of the investigated ion crystals using a ROI size of $7 \text{ px} \times 7 \text{ px}$. The following analysis after fluorescence assignment is equal to the PMT-count analysis. The optimal discrimination threshold differs slightly for the individual ions as shown in fig. 9.3.

It has been shown, that detection errors are small compared to statistical uncertainties in most cases therefore they are neglected.

Part III

Setup characterization

Control of the external and internal degrees of freedom of an ion is the main achievement of trapped ion experiments. Optical frequency standards require an atomic system with minimal perturbations of the clock transition. More precisely, the unavoidable frequency shifts induced by residual ion movement (section 11.1), trapping potential (section 11.3) and contributions from external fields (section 11.2) must be characterized, as their uncertainty defines the systematic uncertainty of the frequency standard. These calculations can then be verified by frequency ratio comparisons with other clocks. In chapter 10, relevant concepts of quantum-optical spectroscopy in ion traps are presented in a condensed form. The description of the major effects perturbing the $^{40}\text{Ca}^+$ systems is given together with performed characterization measurements in chapter 11.

Coherent optical spectroscopy

At the heart of a high resolution spectroscopy experiment is the interaction of a narrow-linewidth laser with a long-lived atomic transition. This interaction aims at the manipulation of the dynamics of the atomic two-level system described by the idealized wave function

$$\Phi(t) = c_g(t) |g\rangle + c_e(t) |e\rangle .$$

The complex valued coefficients $c_g(t)$, $c_e(t)$ contain information about the population in the ground $|g\rangle$ and excited $|e\rangle$ states and the phase evolution of the system. In a pure two-level system without loss of population into other states, the populations fulfil the normalization condition $|c_e(t)|^2 + |c_g(t)|^2 = 1$.

For the light interaction with an electric quadrupole transition, which is the most interesting for this work, the coupling is described by [62]

$$\Omega^{(E2)} = \left| \frac{eE_0\nu_a}{2\hbar} \langle g | \hat{r}_i \hat{r}_j | e \rangle \vec{\epsilon}_i \vec{n}_j \right|$$

with laser electric field amplitude E_0 , transition frequency ν_a , valence electron position operator \hat{r} , polarization vector $\vec{\epsilon}$ and unit vector of laser incidence \vec{n} . The special case of interaction with a spectrum of Zeeman sub-states is covered in section 11.2.1.

The population dynamics caused by laser interaction with an atom prepared initially in $|g\rangle$ is described by

$$|c_e(t)|^2 = \left(\frac{\Omega}{\Omega_R} \right)^2 \sin^2(\Omega_R t / 2). \quad (10.1)$$

Here the Rabi frequency Ω is the coupling strength of the ground to excited state transition with the light field and the generalized Rabi frequency $\Omega_R = \sqrt{\Omega^2 + \Delta\nu^2}$ includes the detuning $\Delta\nu = \nu_a - \nu_L$ of the laser frequency ν_L with respect to the atomic resonance frequency ν_a . In contrast to semi-classical light-atom interaction, the coherent quantum-mechanical description allows for a complete population transfer if a so called π -pulse with duration $t_\pi = \pi/\Omega$ is applied without laser detuning $\Delta\nu$.

In real experiments, decoherence and dephasing effects and population loss into other states must be accounted for. The modelling of eq. (10.1) under these conditions is given by

$$P_e(t) = |c_e(t)|^2 = \frac{C}{2} (1 - \cos(2\pi t f) D(t, \tau)) .$$

Here, the shape of the decay function $D(\tau)$ depends on the spectrum and correlation time of the dephasing process with respect to the interrogation time [96]. Another important timescale is the duration of a complete measurement, which consists of several interrogations per data point for averaging. A suitable choice for slow fluctuations with respect to one interrogation time is $D(t, \tau) = e^{-t^2/2\tau^2}$ [115]. For faster noise processes $D(t, \tau) = e^{-t/\tau}$ is a suitable choice. The contrast C accounts for imperfect state preparation and/or laser detuning.

Experiments with varied pulse time are a major tool to analyse and optimize the system's properties. The a priori unknown coupling strength is retrieved, decoherence and dephasing effects can be quantified.

Spectroscopy measurement are performed by observing population transfer under laser frequency variations. The SNR for such a measurement is maximal if the laser pulse duration matches t_π (eq. (10.1)). The description of the resulting spectrum must include the temporal shape of the laser pulse, as this influences the Fourier-spectrum of the applied light. Within this work exclusively square pulse shapes are used. The excited state population of the interrogated atoms is then given by

$$P_e(\Delta\nu) = \left(\frac{\Omega t}{2}\right)^2 \text{sinc}^2\left(\frac{t}{2}\sqrt{\Omega^2 + \Delta\nu^2}\right) .$$

The stability of the transition frequency is measured using the two-sample method. Here, the transition at the left and right flank is probed at the half-values of the spectral peak. Subtracting the signals results in an amplitude insensitive frequency discrimination slope.

A second method of interrogation is Ramsey's method of separated fields [107]. A resonant opening $\pi/2$ -pulse transfers the atom into the superposition state $\frac{1}{\sqrt{2}}(|e\rangle + |g\rangle)$. In the following *dark time* T_i the atom remains unperturbed. A second $\pi/2$ -pulse with relative phase ϕ to the first pulse is applied afterwards. The state after the second pulse depends on laser detuning, dark time as well as decoherence processes. More precisely,

it depends sinusoidally on the accumulated phase difference $\Phi = 2\pi T_i \Delta\nu$ between laser and atomic oscillation. Although this technique was developed especially to avoid inhomogeneities in long interaction regions in atom beam experiments, it is still widely in use because of its benefits over the usage of long Rabi pulses, like higher sensitivity to frequency variations at equal interrogation times and lower sensitivity to laser intensity fluctuations.

10.1 Dynamics of a trapped ion

Trapping of charged particles is not possible by using only static electrical fields. Either a combination of electrical dc- and ac-potentials is used (Paul trap) or a static field is combined with a magnetic field to confine the ion's position (Penning trap). In the following, the operation principles of the linear Paul trap are presented. The derivation of the relations covering the motion of trapped ions is found e.g. in [9, 77, 147].

The electric potential of a suitable linear electrode configuration

$$\Phi(x, y, z, t) = \frac{U_{\text{rf}}}{2} \cos(\Omega_{\text{rf}} t) \left(1 + \frac{x^2 - y^2}{R^2} \right) + \kappa U_{\text{DC}} \left(\frac{z^2 - \alpha x^2 - (1 - \alpha)y^2}{d^2} \right),$$

is formed by an oscillating 2d electric quadrupole field with amplitude U_{rf} and trap drive frequency Ω_{rf} in the radial (xy-plane) and a static field with amplitude U_{DC} in axial (z) direction forming a 3d quasi potential. The electrode geometry is defined by the radial R and axial d trap dimensions, a geometric factor κ and the parameter $0 < \alpha < 1$ accounting for an asymmetry in the dc-field. In the following only the symmetric case with $\alpha = \frac{1}{2}$ is investigated. In practice, a small asymmetry is favourable to lift the degeneracy of the radial modes.

The equation of motion for a particle with mass m and charge q in this potential is given by [9]

$$\begin{aligned} \ddot{u}_i(t) + \frac{\Omega_{\text{rf}}^2}{4} (a_i + 2q_i \cos(\Omega_{\text{rf}}t)) u_i(t) &= \frac{qE_{s,i}}{m}, & (10.2) \\ a_x = a_y &= -\frac{a_z}{2} - \frac{4\kappa q U_{\text{DC}}}{d^2 m \Omega_{\text{rf}}^2}, \\ q_x = -q_y &= \frac{2q U_{\text{rf}}}{R^2 m \Omega_{\text{rf}}^2}, \quad q_z = 0. \end{aligned}$$

This so called Mathieu equation offers stable trajectories depending on the stability parameters a_i and q_i . Typical ion trap experiments operate in the lowest stability region with $|q_i| < 0.4$ and $|a_i| \ll |q_i|$. Stray electric fields \vec{E}_s cause an additional potential contribution. This is accounted for by the right side of eq. (10.2).

In the lowest order approximation, the solution of the Mathieu equation is given by

$$u_i(t) \approx [u_{0,i} + u_{1,i} \cos(\omega_i t + \varphi_{\text{SI}})] \left[1 + \frac{q_i}{2} \cos(\Omega_{\text{rf}} t) \right]$$

with the phase φ_{SI} depending on initial conditions of the solution and with the secular frequencies of motion

$$\begin{aligned} \omega_z &= \sqrt{\frac{2q\kappa U_{\text{DC}}}{md^2}}, \\ \omega_{x,y} &= \sqrt{\omega_p^2 - \frac{1}{2}\omega_z^2}, \\ &\text{with} \\ \omega_p &= \frac{eU_{\text{rf}}}{\sqrt{2}\Omega_{\text{rf}}mR^2}. \end{aligned}$$

The ion's movement can be separated into a *secular* part with amplitudes $u_{1,i}$ and angular frequencies ω_i and a *micromotion* contribution driven with the trap drive frequency. The stray field causes the displacement $u_{0,i}$. This must be compensated by suitable compensation voltages to minimize this so called excess micromotion (EMM) (section 11.3.1). The modulation of the secular part with the trap drive frequency can be minimized by cooling of the secular motion (section 11.1). Another possible contribution to micromotion is a phase shift between the rf-potential of individual electrodes. This effect as well as contributions from imperfections of the trap geometry have been

neglected here, but were considered in the design considerations of the trap type used within this work [55].

Neglecting the micromotion leads to the simplified potential

$$V(x, y, z) = \frac{m}{2}\omega_x^2 x^2 + \frac{m}{2}\omega_y^2 y^2 + \frac{m}{2}\omega_z^2 z^2. \quad (10.3)$$

This *pseudo-potential* approximation takes the form of a 3D harmonic oscillator. The extension of this relation to multi-ion crystals is presented in appendix A together with expressions for calculating their vibrational mode spectrum.

10.2 Ion-light interaction

Now laser interaction of a two-level atom coupled to a harmonic oscillator is investigated (fig. 10.1a). As seen in this section, this is a suitable model to describe an ion with a narrow linewidth transition within a Paul trap. Explicitly the relation $1/\Gamma \ll \omega_i \ll \Omega_{\text{rf}}$ should be fulfilled and the micromotion is neglected. Using the well known expression for the quantum harmonic

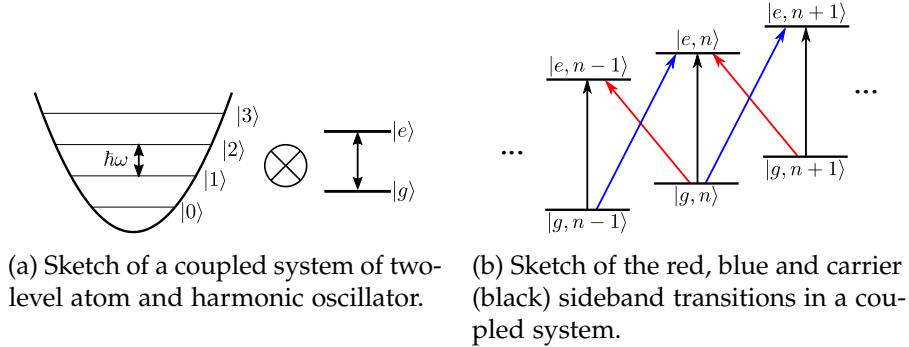


Figure 10.1: Sketch of coupled system

oscillator, the 1D Hamiltonian is described by [113]

$$\begin{aligned} H &= H_a + H_m + H_c, \\ H_a &= \frac{1}{2}\hbar v_a \sigma_z, \\ H_m &= \frac{p^2}{2m} + \frac{1}{2}m\omega^2 x^2 = \hbar \left(a^\dagger a + \frac{1}{2} \right) \\ H_c &= \frac{1}{2}\hbar\Omega (\sigma^+ + \sigma^-) \left(e^{i(kx - v_L t + \varphi)} + e^{-i(kx - v_L t + \varphi)} \right) \end{aligned}$$

where the Pauli spin matrices $\sigma_z, \sigma^+, \sigma^-$ and creation a and annihilation a^\dagger operators of vibrational modes are used. H_a is the

Hamiltonian of the internal state of the ion. The state of the external vibrational modes are described by the quantum harmonic oscillator H_m . H_c contains their interaction by near-resonant laser radiation. This expression is known as Jaynes–Cummings model. Transforming the system in an interaction picture with respect to the atomic frequency ν_a and applying the rotating wave approximation (RWA) to neglect terms oscillating at $2\nu_L$ the last expression yields

$$H_c = \frac{\hbar}{2}\Omega \left(e^{i\eta(a+a^\dagger)}\sigma^+ e^{-i\nu_L t} + e^{-i\eta(a+a^\dagger)}\sigma^- e^{i\nu_L t} \right). \quad (10.4)$$

Here, the Lamb-Dicke parameter η defined as

$$\eta = k \cos(\beta) \sqrt{\frac{\hbar}{2m\omega}} \quad (10.5)$$

is used with the angle β accounting for the general case with an angle between laser incidence and secular mode direction. This parameter relates the recoil energy of a laser photon to the energy of a trap phonon. Therefore, it is an important measure to quantify the coupling between internal and external degrees of freedom.

Further transformation of eq. (10.4) is done by applying the interaction picture $H_c^I = U^\dagger H_c U$ with $U = e^{iH_a t/\hbar}$. In addition, the Lamb-Dicke limit $\eta^2(2n+1) \ll 1$ is assumed, where the vibrational occupation n of the Fock state $|n\rangle$ is sufficient small to neglect contributions of order $\mathcal{O}(\eta^2)$.

$$H_c^I \approx \frac{\hbar}{2}\Omega\sigma^+ \left(1 + i\eta \left(a e^{-i\omega t} + a^\dagger e^{i\omega t} \right) e^{-i\Delta\nu t} \right) + \text{H.c}$$

Depending on the laser detuning $\Delta\nu = \nu_a - \nu_L$ three transitions with vibrational occupation-dependent coupling strength are possible:

- Carrier: $|g, n\rangle \leftrightarrow |e, n\rangle$ at $\Delta\nu = 0$, with $\Omega_{n,n} = \Omega$.
- Blue sideband: $|g, n\rangle \leftrightarrow |e, n+1\rangle$ at $\Delta\nu = +\omega$, with $\Omega_{n,n+1} = \Omega\eta\sqrt{n+1}$.
- Red sideband: $|g, n\rangle \leftrightarrow |e, n-1\rangle$ at $\Delta\nu = -\omega$, with $\Omega_{n,n-1} = \Omega\eta\sqrt{n}$.

Driving a red sideband (RSB) transition may remove one quantum of motion¹, whereas a blue sideband (BSB) transition adds one quantum. Therefore, cooling by addressing a RSB transition is possible (section 11.1.2). In order to remove motional quanta from the system, an additional dissipative process is needed (compare section 11.1.1).

In addition, the vibrational occupation number can be measured by exploiting its dependency on the sideband coupling. For a thermally distributed state within the Lamb-Dicke regime the average quantum number becomes [77, 95]

$$\bar{n} = \frac{P_{\text{RSB}}(t)}{P_{\text{BSB}}(t) - P_{\text{RSB}}(t)}$$

independent of Ω , t and η . Here, P_{BSB} and P_{RSB} are blue and red sideband excitation probability. In general, after ground state cooling, a non-thermal distribution must be assumed. A pulse time signal of e.g. the ground state occupancy of a BSB [77]

$$P_{\text{BSB}}^g(t) = \frac{1}{2} \left[1 + \sum_{n=0}^{\infty} P_n \cos(\Omega_{n,n+1}t) \right] \quad (10.6)$$

can be measured to extract information about the motional state. It contains spectral contributions of all the Fock-state occupancies n with probability P_n .

¹ for an ion prepared in $|g\rangle$ and appropriate pulse time

Systematic shifts

In this chapter, important systematic shifts of the unperturbed transition frequency of a clock transition are summarized. Although the presented concepts are general, the contribution to the total uncertainty is highly dependent on the used atomic species and their used clock transitions.

The section is separated into the origin of these shifts. Prior to the evaluation of the motional shifts an overview over the applied cooling techniques is given in section 11.1. Following on, the influence of external fields is discussed in section 11.2. Perturbations caused by the trapping potential as well as their characterization are treated in section 11.3.

Not all possible systematic shifts are treated within this work. For example the ac-Stark shift from coupling of probe light to other transitions, collisional shifts caused by background gas collisions and gravitational corrections are not characterized.

11.1 Motion induced frequency shifts

Especially for the lighter clock candidate species, motionally induced shifts are a major limiting factor for the accuracy. For the applied cooling techniques described within this chapter the scaling of the crucial Lamb-Dicke parameter is unfavourable with the ion's mass. The kinetic energy from residual secular ion movement around their equilibrium positions cause a 2nd order Doppler-shift also known as *time-dilation shift*. In addition, a high SNR is desired for probing the clock transition. Therefore, a transition which is unperturbed by motionally induced dephasing is advantageous.

11.1.1 Doppler cooling

The first step after photo-ionization of neutral calcium is Doppler cooling. The method was proposed by two groups [51, 143] and demonstrated with Mg^+ and Be^+ ions experimentally in 1978 [97, 141]. This paved the way to high precision spectroscopy and facilitates a large variety of quantum optical experiments. The technique exploits the frequency shifts of an atomic transition

by the Doppler effect in conjunction with dissipation of mechanical energy by spontaneous emission. Although this technique works for free particles [79] and trapped neutral atoms [124] the following description is specialized on trapped ions, mainly following [34].

In a simplified picture, a trapped ion is described as combination of 1D harmonic oscillator and two level system as depicted in fig. 10.1a. For discrimination cooling techniques, the ratio of the cooling transitions natural linewidth Γ to the secular mode frequencies ω is important. For weak confinement $\Gamma \gg \omega$, the motional sidebands are not resolved. This is the regime of Doppler cooling (fig. 11.1). In contrast, with $\Gamma \ll \omega$ sidebands can get resolved individually and this can be exploited for cooling to lower temperatures. This regime of resolved sideband cooling (SBC) is covered in the next paragraph. The cooling

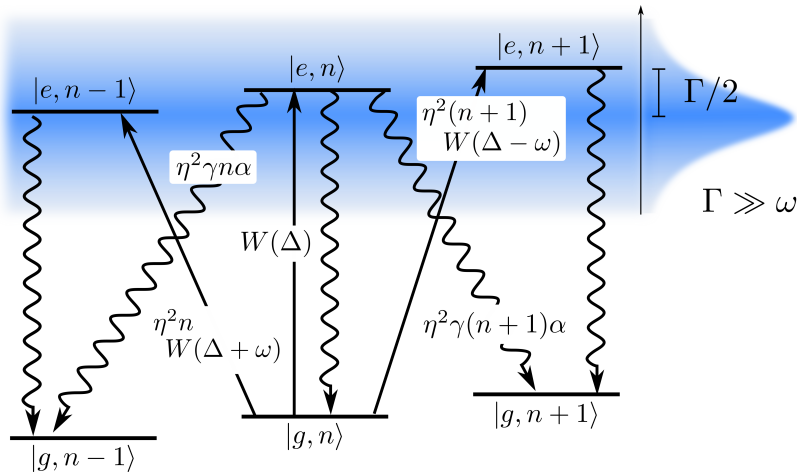


Figure 11.1: Overview of the rate coefficients for Doppler cooling. The combined motional and atomic level system is displayed. Several motional modes are within the absorption spectrum of the broad transition (not to scale).

rate as well as the final temperature are determined by the rate equation of the underlying absorption and emission processes as they alter the mechanical energy of the system. The absorption is described by the dimensionless Lorentzian

$$W(\Delta) = \frac{1}{4\Delta^2/\Gamma^2 + 1},$$

with the laser detuning from resonance Δ . The transition linewidth determines the rate of spontaneous decay. The Raman transition $|g, n\rangle \rightarrow |g, n \pm 1\rangle$ with rate coefficients of

$$A_{\pm} = \frac{\Omega^2}{\Gamma} \eta^2 \left(\cos^2(\theta) W(\Delta \mp \nu_L) + \alpha W(\Delta) \right),$$

increased or decreased motional quantum number with the rates $R_+ = (n+1)A_+$ and $R_- = nA_-$. The sum accounts for two sequential absorption and emission processes neglecting higher order terms. In addition, the laser direction angle θ was added to account for the overlap of the laser direction with the motional direction. The rates of the individual events are summarized in fig. 11.1. The Rabi frequency $\Omega = \vec{d}\vec{E}/\hbar$ has to be smaller than the transition linewidth to avoid over-saturation. The steady-state mean phonon number is given by $\bar{n} = \frac{A_+}{A_- - A_+}$ whose minimum is given at $\Delta = -\Gamma/2$ with $\bar{n}_{i,\min} = \Gamma/2\omega_j$.

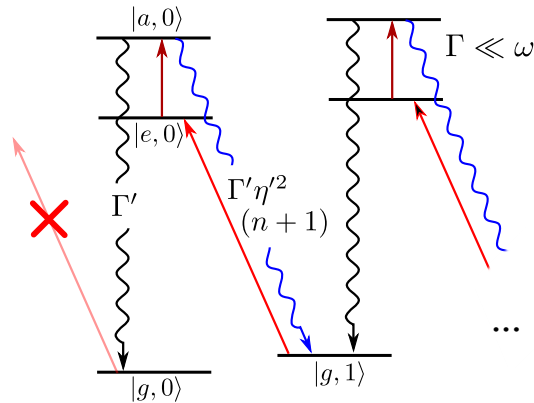
Poorly compensated micromotion (details in section 11.3.1) can degrade cooling performance, as the spectral position of micromotion sidebands are comparable to the linewidth of the atomic transition, thus it's possible to heat on such a transition rather than cool. A useful technique for getting hot ions (e.g. after loading) under this condition pre-cooled effectively, is over-saturating the transition in conjunction with a far red detuned laser beam. Deviations from the presented theory are arising from the additional $^2S_{1/2}$ and $^2P_{1/2}$ transitions, making it a 4-level system as well as the finite spectral width of the laser radiation.

In $^{40}\text{Ca}^+$ the $^2S_{1/2} \leftrightarrow ^2P_{1/2}$ transition is used for Doppler cooling. Therefore, a 397 nm beam, diagonally aligned with respect to all secular mode direction is applied to cool the ion from all directions. The laser frequency ν_L is set at $\Delta \approx -\Gamma/2$ being the theoretical optimum. A laser at 866 nm is needed to repump the population from $^2D_{3/2}$ back to the cooling cycle. To avoid 866 nm light-induced dark resonances, it is blue detuned from resonance. In addition, the repumping laser at 854 nm is shone in, for depopulation of the rarely excited $^2P_{3/2} \rightarrow ^2D_{5/2}$ loss channel. For optimizing the frequencies and coupling strengths of the involved laser pulses on a daily basis, the 2nd and 3rd motional axial red 729 nm sideband excitation is minimized.

11.1.2 Side-band cooling

In the limit $\Gamma \ll \omega_i$, we can address a single sideband by a narrow linewidth laser (fig. 11.2). As a downside, the scattering rate and with it the cooling rate would be very low using only a narrowband transition. Typically, an auxiliary, fast decaying transition is driven to shorten lifetimes. In $^{40}\text{Ca}^+$ the $^2\text{P}_{3/2}$ level is addressed by a 854 nm laser for this purpose.

Figure 11.2: Sideband cooling sketch. A narrow-band laser selectively addresses the red sideband of a long-lived state $|e\rangle$. An auxiliary state $|a\rangle$ with lifetime Γ' and Lamb-Dicke parameter η' is used to artificially shorten the lifetime of this state.



Outside the resolved sideband regime, one major heating mechanism is a carrier excitation followed by a spontaneous emission with excitation of a phonon $|e, n\rangle \rightarrow |g, n+1\rangle$. In the Lamb-Dicke regime, this process is suppressed with $\eta^2(n+1)$, so the motional ground state excitation is reached with high probability. The theoretical cooling limit for $\Gamma \ll \omega_i$ is $\bar{n} \simeq (\Gamma/\omega_i)^2$. In most experiments, however, the minimal temperature is limited by light exciting the carrier or blue sideband from residual fast laser noise or by Fourier broadening (chapter 10) by e.g. square shaped pulses. This effect can limit both, the cooling itself, and/or the temperature measurement (chapter 10) of the cooled mode. In addition, decay to both $^2\text{S}_{1/2}$ ground state can occur if this is not excluded by 854 nm laser polarization and frequency. The needed subsequent optical pumping pulse can degrade motional ground state population, especially if the 397 nm-beam has imperfect σ^- -polarization.

Two conceptually different pulse sequences can be used for SBC. For the first concept, the 729 nm and 854 nm laser illuminate the ion simultaneously. Depending on the coupling strength of the 854 nm laser, the lifetime of the resulting coupled state is shortened (*quenched*). Thus, the linewidth and with it the cooling rate and minimal average phonon number can be varied at will. The 854 nm light causes an ac-Stark shift depending on

the quenching laser parameters, which has to be calibrated and compensated.

In contrast, with pulsed sideband cooling, the 729 nm and 854 nm pulses are sequentially. Thus, the cooling rate is decreased. As a benefit, the frequency and amplitude requirements for the 854 nm laser are less stringent. For this reason this cooling strategy is used in the presented setup.

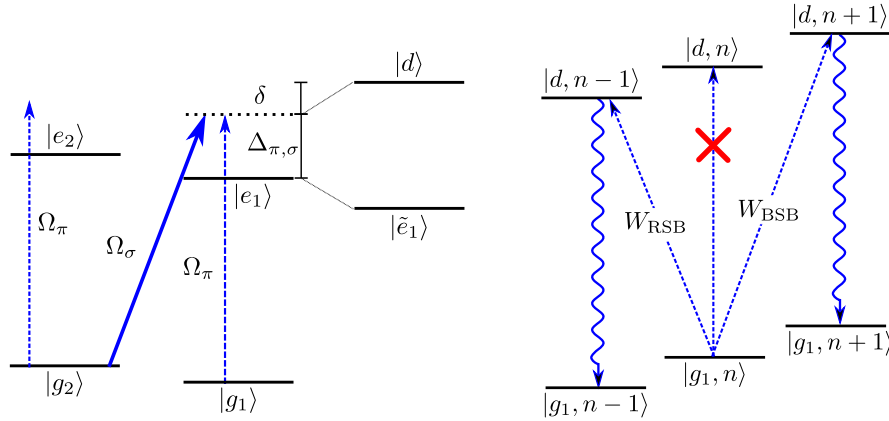
The pulse time has to match the red sideband Rabi frequency $\Omega_{n,n-1} = \eta\sqrt{n}\Omega$ for optimal cooling performance. The optimal pulse time changes during the cooling process with changing motional excitation n . This might cause a huge calibration overhead if the initial mean phonon number is high and/or uncertain. Depending on the available laser power and laser stability, mode temperature after Doppler cooling and number of modes, SBC is relatively slow. Faster and reliable ground state cooling is achieved by using EIT-pre-cooling. In the presented experiment fast pre-cooling of all modes to $\bar{n}_i \approx 0.2$ is achieved, so only a few additional SBC-pulses with fixed pulse length are needed to reach low excitation of the motional modes.

11.1.3 EIT cooling

The presented methods of Doppler and SBC cooling have some drawbacks. While Doppler cooling is fast, robust and can cool several motional modes simultaneous, the achievable mean photon number is typically high ($\bar{n} \gg 1$) for typical trapping parameters. In contrast, SBC is relatively slow, especially if several modes, e.g. in larger ion crystals, must be cooled. One possibility to circumvent this is simultaneous SBC with individual single ion addressing beams [19]. In addition, the frequency of the addressed motional states must be known to a few kHz, potentially making frequent calibration scans necessary.

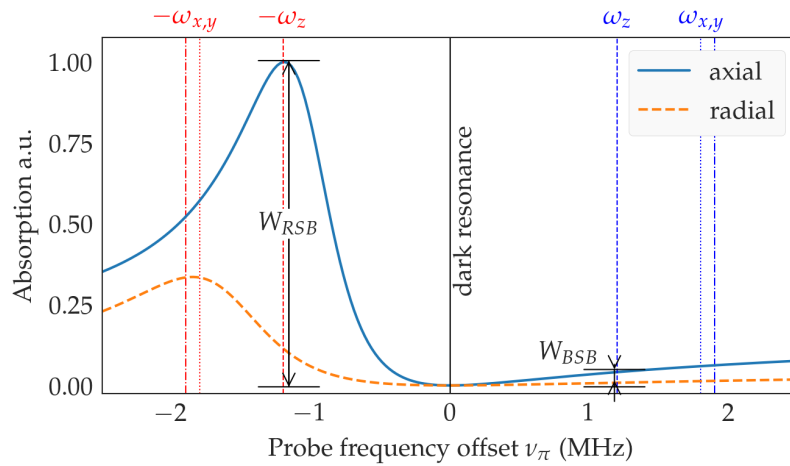
Electromagnetically induced transparency (EIT) cooling in contrast can be treated as an intermediate cooling technique. It can cool reliably and relatively fast all modes in a range of several 100 kHz to $\bar{n}_i < 1$. It was first demonstrated in $^{40}\text{Ca}^+$ by [112]. EIT-cooling uses the same atomic levels as Doppler cooling, but exploits the name-giving quantum interference phenomenon EIT [37] to avoid heating by suppressing the carrier transition (compare fig. 11.3(b)).

For this purpose, two 397 nm laser beams are used. A strong blue detuned σ^- polarized beam couples the $|S_{1/2, \frac{1}{2}}\rangle$ and $|P_{1/2, -\frac{1}{2}}\rangle$ levels and produces a *Fano* absorption profile for the



(a) EIT-cooling level scheme. A strong σ -polarized coupling beam, with blue detuning Δ_σ and coupling strength Ω_σ , couples the $|g_2\rangle \leftrightarrow |e_1\rangle$ transition. The newly produced dressed states $|d\rangle$ and $|\tilde{e}_1\rangle$ are displaced by the ac-Stark shift δ . They are addressed with a π -polarized probe beam with coupling strength Ω_π .

(b) Phonon picture of the artificial cooling transition. Due to a dark resonance at the carrier frequency, only blue and red sidebands are excited. In first order they decay without phonon excitation.



(c) Calculated absorption spectrum for the probe beam for realistic experimental parameters. The two curves reflect optimized parameter sets for cooling the radial or axial modes with typical secular frequencies $\omega_{x,y,z}$. The difference in the absorption amplitudes for the two directions is due to different effective Lamb-Dicke factors $\eta_{\text{ax(rad)}} = 0.16(0.09)$ for these modes. At the dark resonance at the centre position, scattering is highly suppressed whereas at the bright resonance at the red axial (radial)-sideband the scattering rate is maximal. From the difference of the absorption coefficients of red and blue sidebands W_{RSB} and W_{BSB} , the cooling limit can be deduced.

Figure 11.3: EIT-cooling schematic

weaker π polarized beam (see fig. 11.3). For equal detuning $\Delta_\sigma = \Delta_\pi$ from the $|P_{1/2}, +\frac{1}{2}\rangle$ level, the absorption vanishes (*dark resonance*). The coupling laser produces a *bright resonance* at the ac-Stark shift detuning $\delta = \frac{1}{2}\sqrt{\Omega_\sigma^2 + \Delta_\sigma} - |\Delta_\sigma|$. By choosing its coupling strength Ω_σ and detuning appropriate, the bright resonance can be shifted to a motional mode frequency $\delta = \omega_i$. As a consequence, absorption is predominantly on the red sideband. Carrier absorption is highly suppressed, and blue sideband absorption is only possible with reduced probability. Thus, the rate equation is more favourable compared to Doppler cooling. The rate coefficients are given by [75]

$$A_\pm = \frac{\Omega_\pi^2}{\Gamma} \frac{\Gamma^2 \omega_i^2}{\Gamma^2 \omega_i^2 + 4 \left(\frac{\Omega_\sigma^2}{4} - \omega_i (\omega_i \mp \Delta_\sigma) \right)^2}.$$

The cooling rate $R = \eta_{\text{eff}}(A_- - A_+)$ depends on the effective Lamb-Dicke parameter

$$\eta_{\text{eff}} = |(\vec{k}_\pi - \vec{k}_\sigma) \vec{e}_i| \sqrt{\frac{\hbar}{2m\omega_i}}$$

of both laser beams on the i^{th} motional mode.

In the presented setup, a dedicated 397 nm beam with $\vec{k}_\pi \perp \vec{B}_0$ is used. The coupling beam is the same as used for optical pumping. The difference wavevector $\vec{k}_{\text{diff}} = \vec{k}_\pi - \vec{k}_\sigma$ has overlap with all motional modes and a pure polarization can be ensured. In order to optimize for a minimal mode temperature, the coupling strengths $\Omega_\pi, \Omega_\sigma$ are varied via the corresponding AOM driving power. A measurement of the cooling rate in the presented setup is shown in fig. 11.4.

The limitations of the minimal achievable temperature is off-resonant scattering to the $|P_{1/2}, +\frac{1}{2}\rangle$ level and laser frequency instabilities. Laser frequency deviations cause variations of the optimal cooling condition, as they alter $\Delta_\sigma, \Delta_\pi$, and therefore $\delta \neq \omega_i$. But the broad cooling bandwidth makes the scheme more robust against smaller laser frequency fluctuations compared to SBC.

With a phase coherent 866 nm laser, it is possible to form another dark resonance with the ${}^2D_{3/2} \leftrightarrow {}^2P_{1/2}$ transition to enhance red sideband absorption at another motional frequency [120]. In addition, this prevents off-resonant scattering on the $|P_{1/2}, +\frac{1}{2}\rangle$ transition.

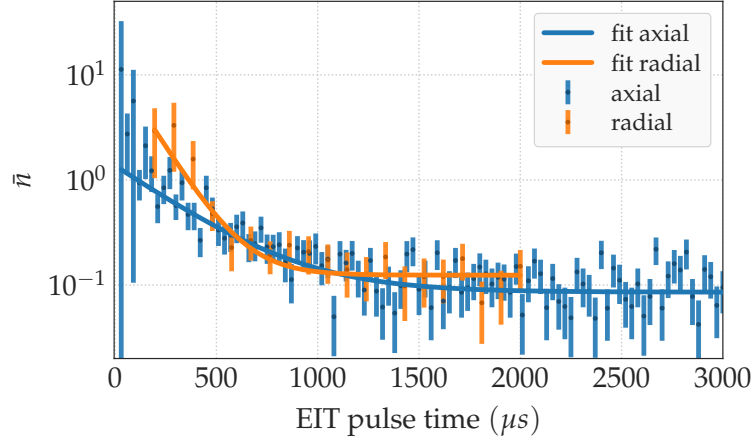


Figure 11.4: EIT-cooling rate measurement. The temperature of a single ion of the axial (radial) mode is measured for varying EIT pulse times. The EIT beam coupling strength $\Omega_{\sigma(\pi)}$ was optimized separately for each secular frequency $\omega_{z(y)} = 2\pi \times 0.605$ MHz and 1.350 MHz. A detuning $\Delta_{\sigma,ax} = 80$ MHz, $\Delta_{\sigma,rad} = 102$ MHz of the pump beam was chosen for axial and radial EIT, respectively. From an exponential fit of the form $\bar{n}(t) = Ae^{-Rt} - n_{ss}$, the cooling rates $R_{axial} = 3.1(3) \text{ ms}^{-1}$, $R_{radial} = 7(1) \text{ ms}^{-1}$ and steady state mean phonon numbers $n_{ss,axial} = 0.085(6)$ and $n_{ss,radial} = 0.12(1)$ were found.

In fig. 11.5 a comparison of axial sideband excitation is shown after Doppler, EIT and SBC. Modelling of the BSB excitation with eq. (10.6) contains the probability of the individual Fock state occupation. In practice, for the low coupling strength, motional dephasing is not unambiguously separable from laser or magnetic-field noise caused dephasing. The determination of mean vibrational occupation from the comparison of sideband excitation (section 10.2) yield $\bar{n}_{\text{EIT}} = 0.2(1)$ and $\bar{n}_{\text{SBC}} = 0.03(3)$. Here the four closest data-points to the BSB π -time were averaged to account for small fluctuations and make use of the largest SNR. The uncertainties are derived from the QPN-limited measurement uncertainty.

The EIT-technique is particular useful for cooling several modes within a limited frequency range. This applies to the near degenerate radial modes of a single ion, bunching modes of mixed species crystals [119, 120] and even larger separated motional modes of a pure multi-ion crystal.

If the separation of different modes is too large, it's possible to use several EIT-pulses with different settings subsequently. This result in a suboptimal temperature for the first cooled modes [120]. Therefore, cooling of the mode with lowest motional

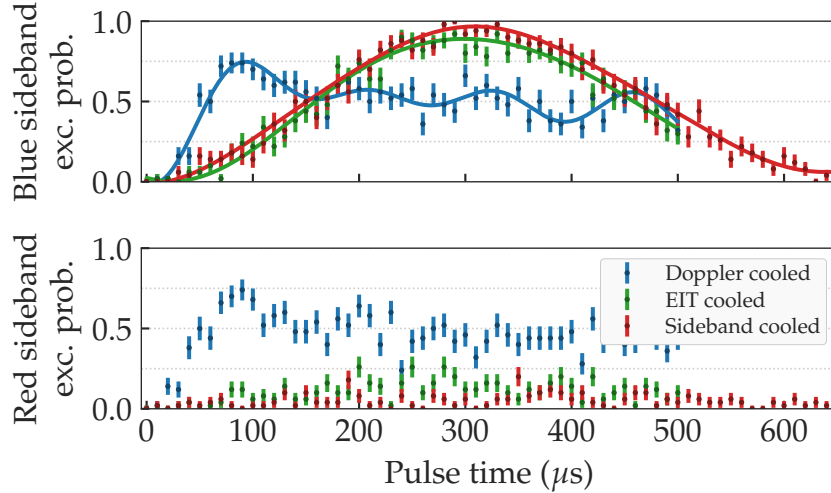


Figure 11.5: Pulse time scan comparison of axial BSB and RSB excitation probability for consecutive cooling methods. The blue sidebands are modelled using eq. (10.6) with a summation over Fock states up to $n_{\max} = 10$. Doppler cooling, as first step, is performed with a 1.5 ms pulse of the diagonal 397 nm laser. For EIT, a detuning $\Delta_{\sigma} = 102$ MHz of the pump beam was chosen. The coupling strength Ω_{σ} , Ω_{π} was adjusted to minimize the temperature of the mode with the chosen cooling time of 1 ms. After EIT pre-cooling, only 10 sideband pulses with a total duration of 1.7 ms (including pulses for quenching and optical pumping) are needed to reach low temperatures.

frequency with the last pulse may be advantageous, depending on the specific experimental requirements. Nevertheless, with typical parameters, sub-Doppler temperatures can be reached even for the first cooled modes, therefore SBC could be used more effectively afterwards. In fig. 11.6, a pulse time scan comparison of the axial carrier transition on a five ion crystal is shown. The transition on the Doppler cooled crystal is subject to fast dephasing due to motional excitation. In contrast, with three subsequent EIT-pulses a reduced mode temperature is reached by optimizing the probe beam coupling to different portions of the 1.8 MHz spanning motional spectrum. The reduced mode temperature is indicated by the lower carrier dephasing after EIT-cooling. A quantitative analysis of the temperature of the individual crystal modes was not performed within this work.

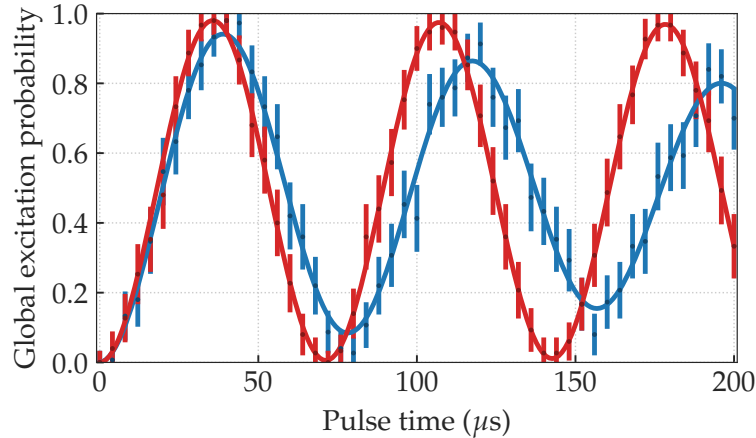


Figure 11.6: Pulse time scan comparison of the axial carrier transition of a five ion crystal. The joint global excitation probability in dependence of Rabi pulse time for a EIT-cooled transition (red) and a faster dephasing (blue) Doppler cooled transition is displayed. The EIT-sequence uses three sub-sequential pulses optimized for the highest, middle and lowest axial secular mode of $[\omega_{z,5}, \omega_{z,3}, \omega_{z,1}] = 2\pi \times [2.433, 1.598, 0.662]$ MHz (in that order).

11.1.4 Heating rates

Spectroscopy pulse times are typically long in metrology experiments. In order to avoid motionally induced frequency shifts, not only low motional excitation after ground state cooling, but also heating over longer time scales without cooling is important for optical clocks. Even for multi-species ion crystals [92, 127], where simultaneous sympathetic cooling is possible, cooling lasers will cause ac-Stark shifts on the transition under investigation [119], so cooling during clock interrogation should be avoided if possible.

Vibrational mode heating is caused by stray fluctuating electrical fields at the vibration mode frequency coupling to the charge of the ions. These fields are caused by various noise sources:

- Pickup from external sources.
- Dc-voltage supply of the trapping electrodes.
- Modulation of the rf-drive of the trap.
- Varying patch potentials on the electrode surfaces.
- Thermally induced electrical (Nyquist) noise.

Especially the latter two effects are dependent to a high degree on the ion-electrode distance d . Furthermore, the electric field spectral density $S_E(d, \omega_i, T)$ of the electric field noise depends mainly on the secular mode frequency ω_i and the electrode temperature T [16].

In the presented setup, the relatively large electrode separation, on-chip filtering of dc-voltages and a high quality factor of the used helical resonator is advantageous for low heating rates.

The rate of heating is measured by adding a variable waiting time after ground state cooling of a single ion. After this period, the excitation of BSB and RSB are compared to deduce the temperature of the ion. In fig. 11.7, the motional heating for three modes is displayed together with deduced heating rates for a typical confinement. Frequency drifts of the sidebands

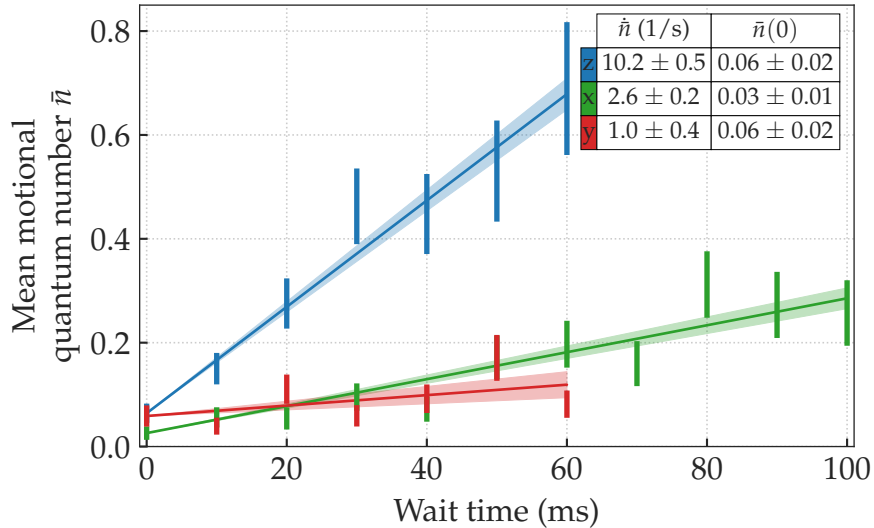


Figure 11.7: Heating rates of the three motional modes of a single ion crystal. The secular mode frequencies are $(\omega_x, \omega_y, \omega_z) = 2\pi \times [1.559(2), 1.407(2), 1.078(1)]$ MHz. The heating rate is given by the linear approximation of the mean motional excitation slope.

by magnetic field fluctuations as well as fluctuations of the mode frequencies limit the measurement's accuracy. Especially the radial modes are prone to frequency drifts by varying rf-amplitude fluctuations, e.g. from temperature changes of the helical resonator. Therefore, the field amplitude within the helical resonator is actively stabilized via feedback to the driving source (compare section 4.2).

From the measured heating rates \dot{n} , the electric field spectral density

$$\dot{n}(\omega_i) = \frac{Ne^2}{4m\hbar\omega_i} S_E(\omega_i)$$

for the investigated mode frequency ω_i is derived [66]. For multi-ion crystals with N ions, this relation is only valid for the centre of mass modes, where all ions oscillate in phase. Coupling of electric fields to out-of-phase-modes requires a significant gradient with respect to the ion crystal's size. Therefore, the heating rates of these modes are typically small.

The deduced electric field spectral density of $S_E([\omega_x, \omega_y, \omega_z]) = [1.1(4), 2.5(2), 7.5(4)] \times 10^{-14} (\text{V/m})^2/\text{Hz}$ is comparable to measurements on $^{172}\text{Yb}^+$ using a similar trap design [16, 66]. The higher axial heating rate cannot be accounted for by the assumed $1/\omega$ scaling of the electric noise [66]. Therefore, an axially directed and/or near-resonant noise effect must be assumed.

Motion of the ion causes Doppler shifts. Interrogation pulses are long compared to the vibration period, therefore the first order Doppler shift of the ion's secular motion averages out. But residual shifts are given for slow motions of the ion with respect to the interrogation laser. These are caused by e.g. changes of the dc-potential of the trap. Therefore, high precision ion clocks typically probe alternating with two counter-propagating beams [15].

The thermal motion of the ion also causes a second order Doppler shift also known as *time-dilation shift* [67]¹

$$\left\langle \frac{\Delta v}{v} \right\rangle_i(t) = \sum_{\alpha} \frac{\omega_{\alpha} \beta_{\alpha,i}^2}{2c^2 m_i} \left(\bar{n}_{\alpha}(0) + \dot{n}_{\alpha} t + \frac{1}{2} \right) \left(1 + \frac{\omega_{pm,i}^2}{\omega_{\alpha}^2} + \frac{\omega_{pm,i}^2}{\Omega_{\text{rf}}^2} \right)$$

with

$$\omega_{pm,i} = |q_i| \Omega_{\text{rf}} / \sqrt{8} \quad \text{and} \quad \sum_i \beta_{\alpha,i}^2 = 1. \quad (11.1)$$

Here, the general expression for the ion i in a crystal with normalized mode vector $\beta_{\alpha,i}^2$ of the mode α is given (compare appendix A). The shift contains contributions of the mean vibration quantum number after ground state cooling $\bar{n}_{\alpha}(0)$ and the time-dependent heating rate contribution $\dot{n}_{\alpha} t$ for each mode. The terms in the second parentheses account for the contribu-

¹ According to the author, there is a typo in the publication. The mode vectors squares are normalized.

tions of the pondermotive trap potential in radial direction. The ground state motion, accounted for with the rightmost summand $\frac{1}{2}$ in eq. (11.1), is unavoidable even with perfect cooling and in the absence of heating.

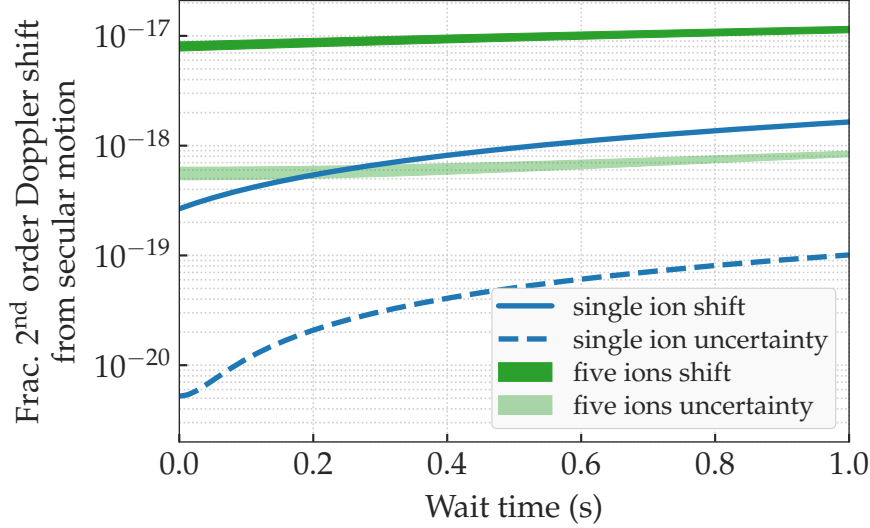


Figure 11.8: Time dilation shift by thermal mode excitation over time without cooling. The calculated shift of a single ion with measured vibrational occupation and heating rate is compared to a crystal of five ions cooled to the Doppler limit. The shaded areas for the multi-ion crystal contain the contributions for all ions.

In fig. 11.8, the 2nd order Doppler shift is shown for a single ion with motional parameters from fig. 11.7. It is compared with a five ion crystal in a potential with secular frequencies $(\omega_{\text{rad},x}, \omega_{\text{rad},y}, \omega_{\text{ax}}) = 2\pi \times [1899, 1827, 622]$ kHz with mode temperatures corresponding to a crystal cooled to the Doppler limit. Based on the heating rate of the single ion measurement, the heating rates of the three centre of mass modes were estimated with

$$\dot{n}_{i,\text{single}} = N \times \dot{n}_{i,\text{multi}} \left(\frac{\omega_{i,\text{single}}}{\omega_{i,\text{multi}}} \right)^2$$

with assumed relative uncertainty of the heating rate of 25%. Based on the findings of [66], the heating rate scales with the number of ions N and the exponent reflecting typical power law scaling of the heating rate with secular frequencies. Heating rates of any other out-of-phase mode can be neglected. For all modes, a mean vibration quantum number after cooling of $\bar{n}_i(0) = \Gamma/2\omega_i$ was used corresponding to the minimal Doppler-cooling temperature for each mode.

11.2 External field shifts

11.2.1 Zeeman shift

$^{40}\text{Ca}^+$ has a nuclear spin quantum number of $I = 0$, therefore its level scheme consists only of fine structure transitions. Each transition splits up into $2J + 1$ magnetic sub-levels within a non-zero magnetic field \vec{B} . The total angular momentum quantum number $J = L + S$ of a particular transition determines the possible magnetic quantum numbers $|m_J| \leq J$. The energy spectrum for the Zeeman interaction in a weak field (anomalous Zeeman effect) is given by

$$E_Z = -\mu_B g_J m_J |\vec{B}|$$

with Bohr magneton μ_B and Landé g-factor g_J . For the $^2\text{S}_{1/2}$ and $^2\text{D}_{5/2}$ levels the Landé g-factor can be calculated approximately $g_{S_{1/2}} = g_S = 2$ and $g_{D_{5/2}} = g_D = \frac{6}{5}$. Accurately measured values are given by $g_S = 2.002\,256\,64(9)$ [138] and $g_D = 1.200\,334\,0(3)$ [20]. The possible $^2\text{S}_{1/2} \leftrightarrow ^2\text{D}_{5/2}$ transitions must obey selection rules for electrical quadrupole transitions $|m_D - m_S| = |\Delta m| \leq 2$, therefore ten different transitions are possible. Here, the abbreviation $m_{D_{5/2}} = m_D$ and $m_{S_{1/2}} = m_S$ are used. In addition, the relative coupling strength to these transitions depends on the absolute difference of magnetic quantum numbers Δm and the incidence angle ϕ and polarization angle γ with respect to the magnetic quantization field (fig. 11.9). The geometric factors for the relative coupling strength $g^{\Delta m}$ are given by [113]

$$\begin{aligned} g^0 &= \frac{1}{2} |\cos(\gamma) \sin(2\phi)|, \\ g^{\pm 1} &= \frac{1}{\sqrt{6}} |\cos(\gamma) \cos(2\phi) + i \sin(\gamma) \cos(\phi)|, \\ g^{\pm 2} &= \frac{1}{\sqrt{6}} \left| \frac{1}{2} \cos(\gamma) \sin(2\phi) + i \sin(\gamma) \sin(\phi) \right|. \end{aligned}$$

The sensitivity to magnetic field shifts

$$\frac{\delta E}{\delta B} = (g_D m_D - g_S m_S) \mu_B$$

ranges from $|\frac{1}{h} \frac{\delta E}{\delta B}| = 5.6 \text{ Hz nT}^{-1}$ to 39.2 Hz nT^{-1} depending on the chosen transition. The high sensitivity to magnetic field fluctuations pose a serious limitation to the operation of $^{40}\text{Ca}^+$

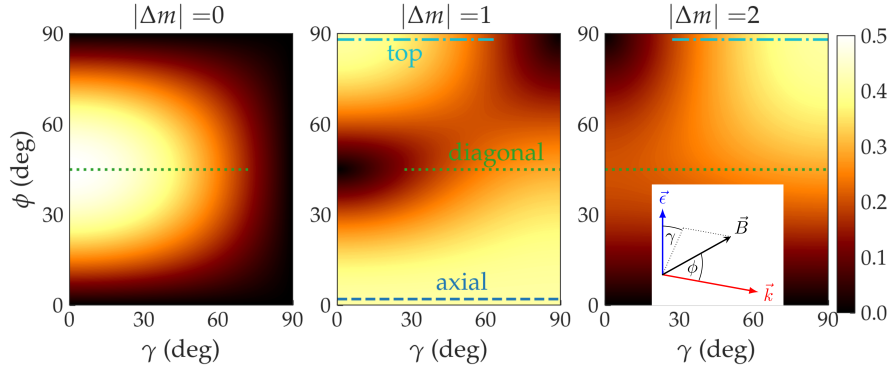


Figure 11.9: Relative optical coupling strength of the ${}^2S_{1/2} \leftrightarrow {}^2D_{5/2}$ Zeeman sub-levels with magnetic quantum number difference Δm . The angle γ is spanned between magnetic field vector \vec{B} projected into plane of incidence and laser polarization \vec{e} . The angle ϕ denotes the laser incidence with respect to the B-field. Possible polarization directions for adequate coupling strength are indicated for the three used beam directions.

clocks [57] and quantum information experiments [115]. Typically multiple layers of magnetic shielding are required to enable long probe times. In contrast, many clock candidates like ${}^{199}\text{Hg}^+$ or ${}^{171}\text{Yb}^+$ use hyperfine states with $m_F = 0 \rightarrow m_{F'} = 0$ or states with vanishing angular momentum like the ${}^1S_0 \rightarrow {}^3P_0$ transition in ${}^{27}\text{Al}^+$ and ${}^{115}\text{In}^+$ as magnetic field-insensitive clock transition [80].

The quadratic component of the Zeeman effect is caused by the coupling of the ${}^2D_{5/2}$ to the ${}^2D_{3/2}$ sub-levels and can be calculated from perturbation theory [21, 32]

$$\begin{aligned} \Delta\nu_{Z^2} &= \frac{K_{m_j}}{\hbar^2(\nu_{D_{5/2}} - \nu_{D_{3/2}})} (\mu_B B)^2 \\ &= \left[108 \text{ Hz/mT}^2 \right] \times K_{m_j} B^2, \end{aligned}$$

with

$$\begin{aligned} K_{\pm\frac{1}{2}} &= \frac{6}{25}, \\ K_{\pm\frac{3}{2}} &= \frac{4}{25}, \\ K_{\pm\frac{5}{2}} &= 0 \end{aligned}$$

and the transition-dependent scaling factor K_{m_j} . The shift does not average out by probing different Zeeman states and is on the order of few Hz for typical fields.

11.2.2 Black body radiation shift

For most clock candidate species the blackbody radiation (BBR) shift is amongst the limiting factors for clock accuracy [30, 59]. It is caused by the mean square electric field caused by the ambient temperature radiation [31]

$$\langle E^2 \rangle_T = \frac{8\pi^5(k_B T)^4}{15\epsilon_0(hc)^3}.$$

The radiation also causes a negligible shift caused by its rms-magnetic field.

In $^{40}\text{Ca}^+$ the BBR shift of the clock transition is calculated from the differential static electric-dipole polarizabilities $\Delta\alpha_0$ of the two involved levels

$$\Delta\nu_{\text{BBR}} = -\frac{1}{2h} \langle E^2 \rangle_T \underbrace{\left(\alpha_0(D_{\frac{5}{2}})(1 + \eta_D) - \alpha_0(S_{\frac{1}{2}})(1 + \eta_S) \right)}_{\Delta\alpha_0},$$

with the static electric-dipole polarizabilities $\alpha_0(i)$, and the temperature-dependent dynamic correction factors η_i accounting for the levels' response to the BBR spectrum [117]. With a measured value $\Delta\alpha_0 = -7.2677(21) \times 10^{-40} \text{ Jm}^2\text{V}^{-2}$ [56] and a temperature estimate $T = 299.5(25) \text{ K}$, the fractional blackbody radiation shift is $\frac{\Delta\nu_{\text{BBR}}}{\nu_a} = -9.22(32) \times 10^{-16}$ in our setup. The shift's uncertainty is mainly limited by the conservative temperature estimate. The fraction of the solid angle of thermal radiation reaching the ion is given by $\approx 40\%$ from the vacuum chamber and from $\approx 60\%$ from the trap electrodes [49]. The former is predominantly determined by the temperature of the room, the latter is also heated by rf-losses in the trap chip material by $\Delta T_{\text{trap}} \approx 5 \text{ K}$ depending on the applied voltages. The temperature sensors placed on the chip (compare chapter 4) ease determination of the electrode temperature, but a detailed measurement of the thermal distribution across the trap must be done. Such an analysis was performed using a similar trap design based on aluminium nitride chip carriers [100]. With the larger thermal conductivity and lower rf-losses, a smaller chip temperature with reduced uncertainty of $\Delta T = 80 \text{ mK}$ could be achieved. Using these values, the shift uncertainty in $^{40}\text{Ca}^+$ would reach $\frac{\delta\Delta\nu_{\text{BBR}}}{\nu_a} \approx 1 \times 10^{-18}$, but therefore, the temperature of the surrounding vacuum chamber has to be known also to this level.

11.3 Trapping potential shifts

11.3.1 Excess micromotion

Residual rf-fields caused by the trapping potential cause motion induced shifts. The amplitude of the present ac-potentials depends on the displacement of the ion from the rf-node of the trapping potential as well as residual fields caused by imperfect trap geometries. A displaced ion is subject to a driven motion at the trap drive frequency with velocity $\vec{v} = \vec{v}_0 \cos(\Omega_{\text{RF}}t + \phi)$. This phenomenon is called excess micromotion (EMM). Thus, all lasers are phase modulated and the spectrum in the laboratory frame is expressed as [69]

$$\begin{aligned} E(\omega_a) &\propto J_0(\beta)\delta(\omega_a - \omega_L) \\ &\quad + J_1(\beta)(\delta(\omega_a - \omega_L - \Omega_{\text{RF}}) - \delta(\omega_a - \omega_L + \Omega_{\text{RF}})) \\ &\quad \dots \end{aligned}$$

with the Bessel function of the first kind J_i , and Dirac delta function δ . For small modulation index $\beta = \vec{k}\vec{v}/\Omega_{\text{RF}} \ll 1$ with wavevector \vec{k} , contributions from higher Bessel functions can be neglected.

Minimization of this inhibitory EMM is desirable. Therefore, the modulation index

$$\beta_i \approx \frac{J_1(\beta_i)}{J_0(\beta_i)} = \frac{1}{2} \frac{\Omega_{\text{EMM},i}}{\Omega_{\text{car},i}}$$

is analysed for three laser beam directions i (compare section 8.5). The distinct directional contributions are determined by comparing the coupling strengths $\Omega_{\text{car},i}$ and $\Omega_{\text{EMM},i}$ of the carrier and 1st order micromotion sideband transitions. The residual rf-electric field amplitude

$$E_{\text{rf},i} = \frac{m\Omega_{\text{rf}}^2}{|\vec{k}_i|q} \beta_i$$

is deduced from the modulation indices. In fig. 11.10, the residual fields for axial displacement are displayed. The equivalence of field measurements with a single displaced ion with measurements on an extended ion crystal has been shown in [68].

As the beam size of the diagonal 729 nm beam is small compared to the scanned region in fig. 11.10, only the modulation of the top beam was used for this measurement.

For determination of the coupling strength, the excitation probability $P(t)$ at a given Rabi pulse time t must fulfil $P(t) > \frac{1}{2} (1 - e^{-t/\tau_{\text{dec}}})$ with the dephasing time τ_{dec} from e.g. magnetic field noise. The decoherence was determined at the outer points of the graph with strong amplitude by fitting a model function to the pulse time scan. This condition is not always met, depending on available laser power and decay rate for low EMM sideband amplitudes. Data points not fulfilling this condition are left out in the figure.

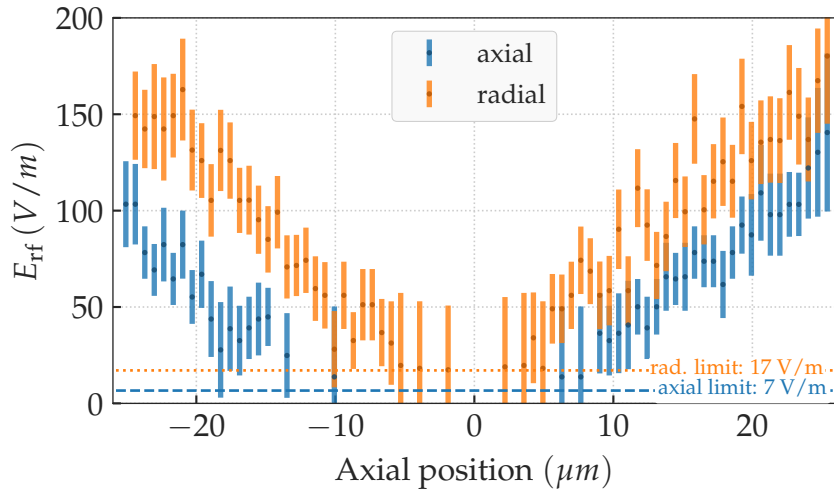


Figure 11.10: Residual rf-electric fields for an axially displaced ion for axial and radial directions. The limitations of the used resolved sideband method by dephasing from e.g. magnet field fluctuations are indicated and data-points below that threshold are neglected. Different limitations arise from the direction-dependent carrier coupling strength and beam intensities.

During operation of the trap, drifting dc-potentials caused by e.g. deposit stray charges from deposition of ablated atoms or ultraviolet-beam interaction with the trap are unavoidable. Thus, the ion position with minimized EMM must be re-measured occasionally. Therefore, the ion position is shifted by altering the DC trapping potential while observing the EMM-amplitude. This is subsequently repeated for the three displacements and laser directions in order to reach the optimal position in three spatial dimensions.

In fig. 11.11, the rf-electric field components of diagonal and top 729 nm beam are displayed in dependence of the radial compensation voltages U_{ec} and U_{tc} (compare chapter 4). The directions of displacement are not orthogonal for the two compen-

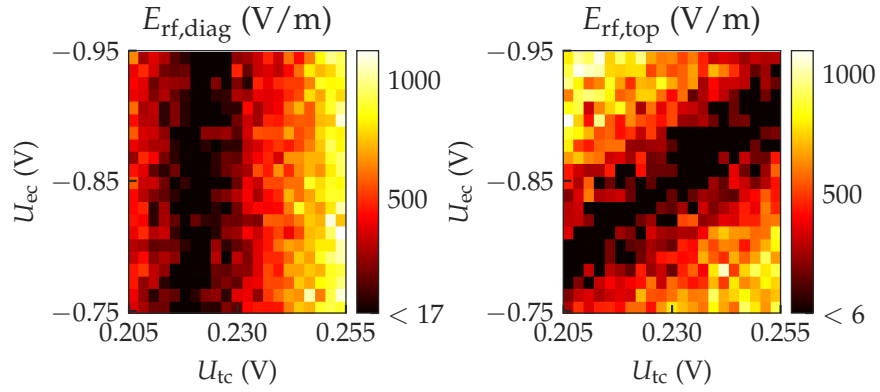


Figure 11.11: Residual rf-electric fields for a radial displaced ion for two laser directions. For the axial direction, the EMM sideband amplitude is too small to quantify.

sation voltages, therefore an iterative minimization is performed to find the voltages of minimal EMM contribution.

Some short-comings of the resolved-sideband technique, especially the limitation by magnet-field drifts are overcome by the photon-correlation technique. This makes usage of the correlation between Doppler cooling fluorescence and the trap drive [69]. This method allows for EMM measurements during Doppler cooling. Therefore, the implementation of this method is planned for the future.

11.3.2 Magic trap drive

The trapping field-induced frequency shift caused by uncompensated EMM and ac-Stark shift is given by [9, 31]

$$\frac{\Delta\nu_{\text{rf}}}{\nu_a} = -\frac{1}{2} \sum_{i=x,y,z} \sum_{n=1} \underbrace{\left[\frac{\Delta\alpha_0}{h\nu_a} + \frac{1}{n^2} \left(\frac{e}{mc\Omega_{\text{RF}}} \right)^2 \right]}_{\zeta} \langle E_i^2(n\Omega_{\text{RF}}) \rangle,$$

with the mean-squared electric field $\langle E_i^2(n\Omega_{\text{RF}}) \rangle$ at multiples of the trapping drive frequency and the differential static electric-dipole polarizability $\Delta\alpha_0$.

For the clock transition of $^{40}\text{Ca}^+$, the differential polarizability $\Delta\alpha_0$ is negative, therefore the micromotion-induced scalar Stark shift (first summand) and the 2nd order Doppler shift (second summand) counteract each other. For the *magic* trapping frequency

$$\Omega_{\text{magic}} \simeq \frac{e}{mc} \sqrt{-\frac{h\nu_a}{\Delta\alpha_0}}$$

the scaling factor ζ vanishes (neglecting higher order terms).

A comparison of two $^{40}\text{Ca}^+$ clocks revealed the magic trapping frequency $\Omega_{\text{magic}} = 2\pi \times 24.801(2)$ MHz by altering the drive frequency in one setup [56].

In the presented setup, the resonance frequency of the helical resonator prevents operation on this magic frequency. The replacement with a matched resonator is in preparation. The actually used trap frequency $\Omega_{\text{RF}} = 2\pi \times 33.00(5)$ MHz leads to a scaling factor $\zeta = -1.162(1) \times 10^{-21} (\text{V/m})^{-2}$, which is approximately 1000-fold higher compared to an optimal magic trap drive with the same uncertainty. The chosen trap drive uncertainty reflects the design goal of the newly produced helical resonator's resonance frequency. Higher harmonics on the rf-drive alter the magic frequency; this contribution is neglected for this assumption.

In fig. 11.12, the combined 2nd order Doppler and ac-Stark shift is displayed for axial displacement. Again, missing points are below the decoherence threshold. The displayed shift uncertainty includes QPN and fitting errors. Equal contributions in both radial directions was assumed. The shift is well below the natural lifetime limit for a five ion crystal close to the zigzag phase transition (compare section 15.1). Thus, individual ion

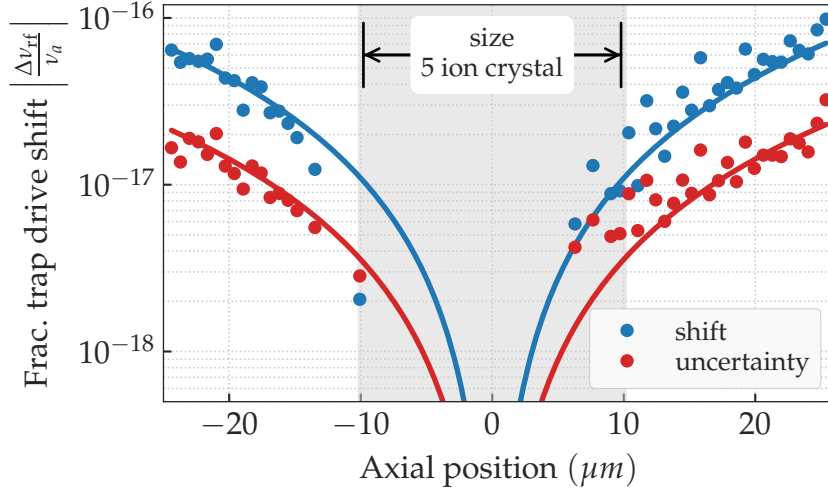


Figure 11.12: Contribution of the combined trap drive-induced 2nd order Doppler and ac-Stark shift from EMM. The shift (blue) and uncertainty (red) is compared to the extension of a five-ion crystal with confinement of $(\omega_{ax}, \omega_{rad,x}, \omega_{rad,y}) = 2\pi \times [622, 1827, 1899]$ kHz. Missing points are below the decoherence limit. The data is approximated with two quadratic functions.

shifts pose no serious limitation to joint interrogation of multi-ion crystals of this size. The shift uncertainty is determined by the precision of the underlying measurement. Thus, lower magnetic field noise, reduced QPN through a larger dataset, as well as larger coupling by e.g. higher available laser power, would decrease this uncertainty. In addition, the parameters of this measurement were optimized for covering a large axial region. A measurement of a smaller region around the optimum point can be found in [49, 50]. Using a trap drive frequency closer to the magic frequency would reduce the shift and uncertainty significantly.

The cancellation of these rf-induced shifts becomes crucial for multi-ion crystals in a 3D configuration as proposed in [1]. A high rf-field is unavoidable at ion positions far from the nodal axial line in radial extended crystals.

11.3.3 Quadrupole shift

Tensorial shifts depending on the field gradients, present at the position of the ions, pose a limitation to a clock's accuracy. In a multi-ion clock, these inhomogeneous shifts limit the usable probe times and even prevent the typically employed averaging

schemes if the shift is not probed and averaged on the level of an individual ion. The quadrupole shift (QPS) caused by trapping rf-field averages out, so only the static field must be accounted for if second order effects are neglected.

The quadrupole shift

$$\Delta\nu_{\text{QPS}} = \frac{\Theta}{\hbar} \times f(\alpha, \beta, \gamma) \times h(J, m_J)$$

can be divided into three parts: The species and transition dependent quadrupole moment Θ is the first contribution. The quadrupole moment for the $^2D_{5/2}$ level in $^{40}\text{Ca}^+$ is $\Theta = 1.8(1)ea_0^2$ [111] with Bohr radius a_0 and elementary charge e . A list of moments for widely used ionic clock species can be found in [80]. The second term

$$\begin{aligned} f(\alpha, \beta, \gamma) = & \frac{\partial E_z}{\partial z} \frac{1}{4} \left(3 \cos(\beta)^2 - 1 \right) \\ & + \frac{1}{2} \sin(2\beta) \left(\frac{\partial E_x}{\partial z} \cos \alpha + \frac{\partial E_y}{\partial z} \sin \alpha \right) \\ & + \frac{1}{4} \sin^2 \beta \left[\left(\frac{\partial E_x}{\partial x} - \frac{\partial E_y}{\partial y} \right) \cos(2\alpha) + 2 \frac{\partial E_x}{\partial y} \sin(2\alpha) \right] \end{aligned} \quad (11.2)$$

includes the gradient of the electric field $\frac{\partial E_i}{\partial r_j}$ and the Euler angles (α, β, γ) [61], parametrizing the clock laser incidence direction. For the QPS measurements described in this work, only the axial direction is used, so $\alpha = \beta = \gamma = 0$ applies. Therefore, this expression simplifies to $f(0, 0, 0) = \frac{1}{2} \frac{\partial E_z}{\partial z}$. For multi-ion crystals, the field gradients arise from a combination of the external field generated by the Paul trap and the joint field of the ions. Therefore, the equilibrium positions of the ions for given trapping parameters must be known (compare appendix A) for calculation of the shift for a given configuration. The last term reflects the dependency of the magnetic sublevel m_J for a state with total spin J

$$h(J, m_J) = \frac{J(J+1) - 3m_J^2}{J(2J-1)}. \quad (11.3)$$

There are two options to average out this shift according to eq. (11.2) and eq. (11.3). The shift vanishes for three perpendicular B-field orientations [61] as well as a sum over the Zeeman states. The latter benefits from a simultaneous cancellation of

the Zeeman shift. As the electric field gradient stays constant to a high degree, this shift can be cancelled to a high degree in single ion clocks [20, 85]. However, in multi-ion clocks, the inhomogeneous nature of the shift poses a limitation for the resolution of the joint linewidth. For clock transitions with $L < 1$, quadrupole moment vanishes and therefore the shift can be neglected.

11.3.4 *Tensor ac-Stark shift*

For a EMM compensated, linear crystal the rf-amplitude at the nodal line is small (section 11.3.1), so Stark shift contribution arising from the rf-amplitude can be neglected. However, for a radially extended crystal a significant field is present, thus a significant scalar and tensor ac Stark shift (TASS) will arise. The scalar contribution is cancelled if the trap is operated at the magic frequency (see section 11.3.2). The shift of the tensorial part [1]

$$\Delta\nu_{\text{TASS}} \propto h(J, m_J) \times \alpha_{\text{DC}} \times \langle E^2 \rangle,$$

with the time averaged electric field $\langle E^2 \rangle$ and the dc tensor polarizability α_{DC} . This term has the same dependency $h(J, m_J)$ from the quantum numbers as the QPS. Thus, these shifts are suppressed simultaneously.

Part IV

Continuous dynamical decoupling

In the previous parts it was shown, that the statistical uncertainty of a $^{40}\text{Ca}^+$ clock is limited by magnetic-field noise. Without magnetic shielding, the probe time of the clock transition is limited by this to few milliseconds, resulting in a low duty cycle and large statistical uncertainty. In chapter 13, a continuous dynamical decoupling technique is introduced, which suppresses the sensitivity to magnetic-field shifts. The properties of the artificial transition generated by this technique are investigated on a single ion in chapter 14. The scheme is also capable of suppressing tensorial frequency shifts, caused by inhomogeneous transition broadening in multi-ion crystals. This is investigated in chapter 15.

Clock ions like $^{40}\text{Ca}^+$ suffer from many unwanted shifts like the linear Zeeman shift and inhomogeneous QPS and TASS. The linear Zeeman shift could be controlled by technical means e.g. magnetic shielding and/or offset field generation with low drift permanent magnets [115]. But the inhomogeneous shifts are an intrinsic limitation for the seamless operation of multi-ion optical clocks for ionic species with non-vanishing quadrupole moment. Due to the unavoidable electrical field gradient in a Paul trap, the magnitude of these is $\delta\nu \approx 1\text{ Hz}-100\text{ Hz}$ for typical trapping potentials.

There are several approaches how to mitigate these shifts even without exact knowledge of the electric field gradient. The simplest is to use the different scaling of the shift with m_j^2 or the alignment of the probe laser to the quantization B-field to sequentially average over different transitions or directions [61, 126]. This approach is often employed for single ion clocks, but is of limited use for multi-ion clocks, as the inhomogeneous shift limits the probe time and the shift must be analysed for each ion individually. Another method dynamically changes the static offset B-field direction within the clock interrogation [74] to mimic the magic angle spinning technique from nuclear magnetic resonance spectroscopy [3].

In contrast to those techniques, we employ continuous rf-magnetic fields, near-resonant to the Zeeman-levels of the $^2\text{S}_{1/2}$ and $^2\text{D}_{5/2}$ manifolds. These fields drive transitions among the bare Zeeman states, mimicking the above-mentioned subsequent averaging, but within a single interrogation. As the timescale of these transitions, namely the inverse Rabi frequency of the rf-coupling, is much faster than an experimental cycle, suppression of fast noise processes becomes possible. Such dynamic decoupling techniques are a common tool for protection of the system's coherence against unwanted coupling to a noisy environment. The simplest implementation, the so-called spin echo, is used in nuclear magnetic resonance spectroscopy for over half a century [47]. Since then, a variety of dynamic decoupling methods have been employed to suppress different noise pro-

cesses in systems like nitrogen vacancy centres [42], solid state quantum-information processing [130], or trapped ions [99].

For non-continuous dynamical decoupling a sequence of strong external control pulses is used to rewind the dephasing of the atomic system under environmental noise processes. To achieve this, opposing sensitivities of the states are exploited. Here, the timescale of the noise must be slow compared to the interval between refocusing pulses to ensure a high degree of cancellation.

Instead of a sequence of pulses, a continuous external control field is applied in continuous dynamical decoupling. Although the intuitive picture of the noise suppression is similar, the dressed states picture is better suited for the theoretical description. Here, the coupling of the rf-field with the Zeeman manifold generates a set of new eigenstates the so-called dressed states with an energy gap between them. A stronger coupling is equivalent to a faster rotation between opposing states or a larger energy gap in the dressed states picture. Analogous to the non-continuous case, a faster state change improves suppression of fast dephasing processes, but this description is only valid if the energy gap is small compared to the splitting of the Zeeman states. Therefore, the static magnetic offset field was chosen as compromise between large state splitting and practicality of its low noise implementation.

The dressed states have altered sensitivities to different environmental perturbations depending on the chosen parameters of the rf-drives. For example, a certain detuning from resonance of the $^2D_{5/2}$ states generates dressed states with suppressed rank two tensor shifts. This can be treated similarly to the magic angle spinning technique [3]. The theoretical description of the scheme is depicted in chapter 13. In the following chapters is shown, that the linear Zeeman shift (section 14.3.1) as well as QPS and TASS (section 15.3) get suppressed by tailoring of the new eigenstates of a dressed system. Therefore, these new robust eigenstates enable long interrogation times, even for multi-ion crystals, through a prolonged duty cycle in contrast to interleaved interrogation schemes (chapter 14).

Kaewuam et al. [65] and Shaniv et al. [128] have demonstrated a suppression of these inhomogeneous shifts in $^{88}\text{Sr}^+$ and $^{176}\text{Lu}^+$ using similar dynamical decoupling techniques.

Continuous dynamical decoupling theory

This section deals with the interaction of magnetic rf-fields with atoms. The focus is on near-resonant interactions with the Zeeman sub-levels $^2S_{1/2}$ (S) and $^2D_{5/2}$ (D) of $^{40}\text{Ca}^+$, although many of these concepts are transferable to other species. The theoretical treatment in this section is following Aharon et al. [1] and Martínez-Lahuerta et al. [88], and is inspired by private communication with their authors.

In an external magnetic dc field with amplitude B_0 , the $^2S_{1/2}$ and $^2D_{5/2}$ levels split up, which is described by the Hamiltonian

$$H_{0,i} = \hbar \underbrace{g_i \mu_B B_0}_{\omega_{0,i}} J_{z,i} \quad \text{with } i = S, D,$$

with Bohr magneton μ_B , gyromagnetic factors $g_{S(D)}$ and spin-Z operator $J_{z,S(D)}$. The following steps are equal for the S- and D-manifold, so the level index is omitted for now. Applying an additional oscillating magnetic field with frequency ω_1 and amplitude Ω_1 perpendicular to the static field can be described by the interaction Hamiltonian

$$H_{\text{rf}} = \hbar g \Omega_1 \cos(\omega_1 t) (\cos(\alpha) J_x + \sin(\alpha) J_y),$$

with the angle α_i accounting for an angle relative to the chosen coordinate system. Without loss of generality, we choose $\alpha_S = 0$ and $\Delta\alpha = \alpha_D$. It is convenient to separate the driving frequency ω_1 into the resonant ω_0 and detuned Δ_1 contributions

$$\omega_1 = \omega_0 - \Delta_1.$$

In order to analyse the joint Hamiltonian $H_1 = H_0 + H_{\text{rf}}$ further, we apply a unitary rotation $U_{\vec{r}}(\phi)$ around z using

$$\begin{aligned} H^I &= U_z(\theta) H_1 U_z^\dagger(\theta), \\ U_z(\omega_1 t) &= e^{-i\omega_1 t J_z} \end{aligned}$$

to change to a rotating frame with frequency of the drive frequency ω_1 . If we neglect for now the fast oscillating term at $2\omega_1$ (RWA), the equation takes the form

$$H^I = (\Delta_1 + \omega_1) J_z + \frac{g\Omega_1}{2} (J_x \cos(\alpha) + J_y \sin(\alpha)) . \quad (13.1)$$

Another rotation is applied to transform into the basis states of the dressed transition:

$$\begin{aligned} H^f &= U_{\vec{r}_1}(\theta) H^I U_{\vec{r}_1}^\dagger(\theta) , \\ U_{\vec{r}_1}(\theta_1) &= e^{-i\theta_1 \vec{r}_1 \cdot \vec{J}} = e^{-i\theta_1 (-J_x \sin(\alpha) + J_y \cos(\alpha))} , \end{aligned}$$

with the rotation vector

$$\vec{r}_1 = \begin{pmatrix} -\sin(\alpha) \\ \cos(\alpha) \\ 0 \end{pmatrix} ,$$

and first stage mixing angle θ_1 defined by

$$\cos(\theta_1) = \frac{\Delta_1}{\bar{\omega}_1} .$$

Here, the frequency splitting of the first stage dressed states

$$\bar{\omega}_1 = \sqrt{\Delta_1^2 + \left(\frac{g\Omega_1}{2}\right)^2}$$

is used. With these two transformations, the single dressed Hamiltonian takes the simple form

$$H^f = \bar{\omega}_1 J_z ,$$

corresponding to an ac-Zeeman shift.

A drawback is the large sensitivity of the energetic splitting to rf-amplitude fluctuations

$$\delta\bar{\omega}_1 \underset{\Delta_1 \rightarrow 0}{\propto} \delta\Omega_1 .$$

As a high coupling strength is required for suppression of magnetic field noise as described in section 13.1, a technique for mitigating the driving noise shift has to be found. Therefore, a second driving stage with frequency ω_2 near-resonant to the first stage state splitting $\omega_2 = \bar{\omega}_1 - \Delta_2$ and reduced coupling

strength Ω_2 and relative phase shift of $\frac{\pi}{2}$ is used (see eq. (C.4)). The modified Hamiltonian for a modulated drive waveform is

$$H_{\text{rf},2} = \hbar g (\Omega_1 \cos(\omega_1 t) - \Omega_2 \sin(\omega_1 t) \cos(\omega_2 t)) \times (J_x \cos(\alpha) + J_y \sin(\alpha)) . \quad (13.2)$$

The total Hamiltonian $H_2 = H_0 + H_{\text{rf},2}$ is transformed similar to the first stage approach. Two additional rotations are applied to transform the Hamiltonian into the rotating frame and afterwards into the basis of the 2nd stage:

$$H_2^I = U_2 U_1 H_2 U_1^\dagger U_2^\dagger . \quad (13.3)$$

Here analogous definitions for the second stage rotations

$$\begin{aligned} U_1 &= U_{\vec{r}_1}(\theta_1) U_z(\omega_1 t) , \\ U_2 &= U_{\vec{r}_2}(\theta_2) U_z(\omega_2 t) , \\ U_I &= U_z(\bar{\omega}_2) , \\ \vec{r}_2 &= \begin{pmatrix} \cos(\alpha) \\ \sin(\alpha) \\ 0 \end{pmatrix} , \end{aligned} \quad (13.4)$$

with second stage mixing angle and frequency splitting of the second stage dressed states

$$\cos(\theta_2) = \frac{\Delta_2}{\bar{\omega}_2} , \quad (13.5)$$

$$\bar{\omega}_2 = \sqrt{\Delta_1^2 + \left(\frac{g\Omega_1}{4}\right)^2} \quad (13.6)$$

are used.

The resulting Hamiltonian becomes

$$H_2^I = \bar{\omega}_2 J_z . \quad (13.7)$$

The spectrum of the newly produced transitions is given by

$$\begin{aligned} E_M/\hbar = \omega_M &= m_{0D}\omega_{1D} + m_{1D}\omega_{2D} + m_{2D}\bar{\omega}_{2D} \\ &\quad - m_{0D}\omega_{1S} - m_{1S}\omega_{2S} - m_{2S}\bar{\omega}_{2S} , \end{aligned} \quad (13.8)$$

with abbreviation

$$M \hat{=} (m_{0D}, m_{0S}, m_{1D}, m_{1S}, m_{2D}, m_{2S})$$

for the Z-components of the total angular momentum m_{0D} , m_{0S} , first stage quantum numbers m_{1S} , m_{1D} and second stage quantum numbers m_{2S} , m_{2D} specifying a particular transition. The transitions frequencies of the first stage are given by modifying eq. (13.8) with $m_{2D} = m_{2S} = 0$ and $\omega_{2S(D)} \rightarrow \bar{\omega}_{1S(D)}$. With the quadrupole transition selection rule $|m_{0D} - m_{0S}| \leq 2$ and $-\frac{1}{2} \leq m_{1(2)S} \leq \frac{1}{2}$ for the S-level and $-\frac{5}{2} \leq m_{1(2)D} \leq \frac{5}{2}$ for D-level manifold. There are no selection rules for CDD-transitions between S- and D-level of first and/or second stage for one manifold. However, the selection rules of the underlying Zeeman transition are still valid. The modification of the optical coupling strength for all these transitions is shown in section 14.2. The spectrum as well as the properties of the mixed states are characterized by a set of nine parameters $(B_0, \omega_{1S}, \omega_{1D}, \omega_{2S}, \omega_{2D}, \Omega_{1S}, \Omega_{1D}, \Omega_{2S}, \Omega_{2D})$. An overview is given in fig. 13.1.

Here, one might identify the resonance frequencies ω_{0i} with the bare Zeeman splitting. But there are two corrections to this: We have neglected fast oscillating terms in eq. (13.1). This is not strictly fulfilled as line splitting and coupling strength are not well separated $2\omega_1 \not\gg g\Omega_1/2$. Treating the system's full dynamics is computationally intensive, as many timescales must be taken into account. Thus, corrections are made to account for the major contributions. As described in [1] and [88] this can be taken into account by a resonance frequency modified by the Bloch-Siegert shift [12]

$$\omega_{0i}^* = \omega_{0i} \left(1 + \frac{g_i}{8} \frac{(\Omega_{1i})^2 + (\Omega_{2i})^2}{\omega_{0i}(\omega_{0i} + \omega_{1i})} \right). \quad (13.9)$$

The second correction is the cross-coupling of the S-drive on the D-manifold and vice versa. This leads as well to a shift of the resonance frequency of

$$\begin{aligned} \omega_{0S}^\# &= \omega_{0S} \left(1 + g_S \frac{(\Omega_{1D})^2 + (\Omega_{2D})^2}{(\omega_{0S})^2 - (\omega_{0D})^2} \right), \\ \omega_{0D}^\# &= \omega_{0D} \left(1 + g_D \frac{(\Omega_{1S})^2 + (\Omega_{2S})^2}{(\omega_{0D})^2 - (\omega_{0S})^2} \right). \end{aligned} \quad (13.10)$$

For the second stage, these corrections are small, so they are neglected.

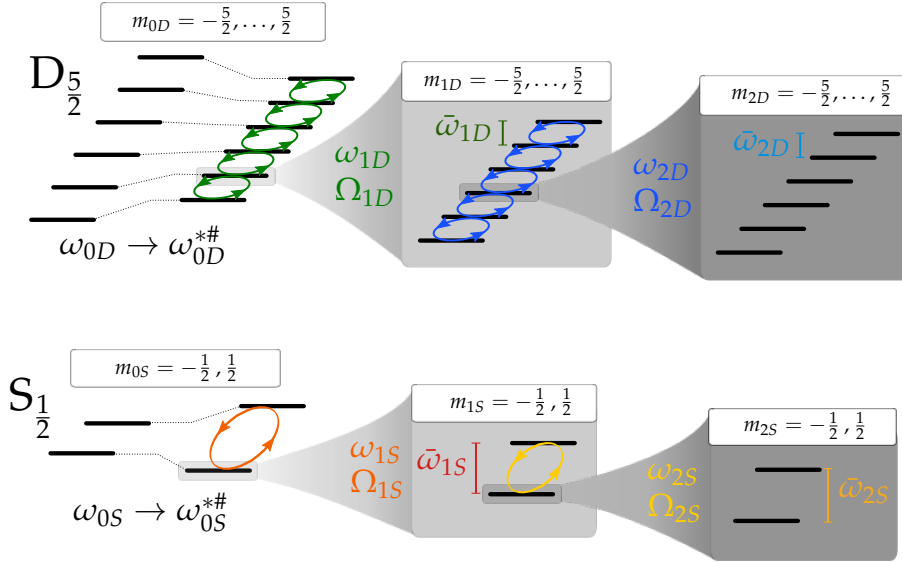


Figure 13.1: Sketch of the CDD level-scheme for a two stage drive. Starting from the bare Zeeman levels, the cross-coupling and Bloch-Siegert shift corrected levels with splittings $\omega_{0i}^{*#}$ with $i = S, D$ are coupled by near-resonant magnetic fields with frequencies $\omega_{1(2)i}$ and coupling strength $\Omega_{1(2)i}$. The spectra of the 1st and 2nd coupling stage are shown detailed in a region around a particular base transition. The associated state splittings $\bar{\omega}_{1(2)i}$ are indicated for each manifold.

13.1 Magnetic field suppression

In order to obtain an expression for the frequency shift due to magnetic field fluctuations δB_0 , a Taylor expansion of the line splitting $\bar{\omega}_1$ is used. With given CDD parameters only the detuning from the resonance condition is affected by this noise process:

$$\bar{\omega}_1(\delta B_0) = \sqrt{(\Delta_1 + g\mu_B\delta B_0)^2 + \left(\frac{g\Omega_1}{2}\right)^2}.$$

Up to second order, the Taylor expansion for the first stage is

$$\begin{aligned} \bar{\omega}_1(\delta B_0) &= \bar{\omega}_1(0) + \left. \frac{\partial \bar{\omega}_1}{\partial \delta B_0} \right|_{\delta B_0 \rightarrow 0} \delta B_0 + \frac{1}{2} \left. \frac{\partial^2 \bar{\omega}_1}{\partial \delta B_0^2} \right|_{\delta B_0 \rightarrow 0} \delta B_0^2 + \mathcal{O}(\delta B_0^3) \\ &= \bar{\omega}_1(0) + \frac{\Delta_1}{\bar{\omega}_1} g\mu_B \delta B_0 + \left(\frac{\bar{\omega}_1^2 - \Delta_1^2}{2\bar{\omega}_1^3} \right) (g\mu_B \delta B_0)^2 + \mathcal{O}(\delta B_0^3). \end{aligned}$$

The suppression of magnetic field noise is in first order dependent on the detuning from the resonance condition Δ_1 and is proportional to $1/\Omega_1$. For the suppression of the QPS, a dif-

ferent detuning is needed (compare eq. (13.13)), therefore high suppression of both effects is not possible with a single drive. This relationship is illustrated in fig. 13.2.

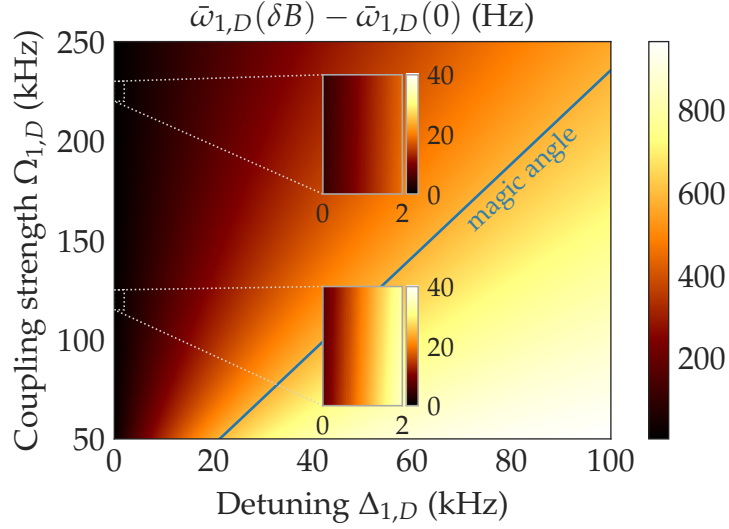


Figure 13.2: Relative B-field shift of the relative line splitting of the single dressed D transition in dependence of the coupling strength and detuning from resonance condition. This illustrates the transition's sensitivity to magnetic field noise. The underlying magnetic field deviation $\delta B = 60$ nT was chosen to match the amplitude of the mains field fluctuation in our setup (compare section 5.2), which would cause a frequency shift of $|\delta\nu| = 672$ Hz on the bare $|S_{1/2, -\frac{1}{2}}\rangle \leftrightarrow |D_{5/2, -\frac{3}{2}}\rangle$ transition. For the magic angle, at which the QPS is suppressed, the B-field sensitivity suppression is small compared to the resonant case with $\Delta_{1,D} \approx 0$. The two insets quantify the dependency of the shift for a small detuning for two different coupling strength.

Next, the B-field suppression of the second stage is investigated. The Taylor expansion of the second stage line splitting

$$\bar{\omega}_2 = \sqrt{\left(\sqrt{(\Delta_0 + g\mu_B\delta B)^2 + \left(\frac{g\Omega_1}{2}\right)^2} - \omega_2 \right)^2 + \left(\frac{g\Omega_2}{4}\right)^2}$$

is given by

$$\begin{aligned} \bar{\omega}_2(\delta B_0) = & \bar{\omega}_2(0) + \frac{\Delta_1\Delta_2}{\bar{\omega}_1\bar{\omega}_2}g\mu_B\delta B_0 + \\ & \left[\frac{\Delta_1\Delta_2}{\bar{\omega}_1\bar{\omega}_2^3} + \frac{1}{\bar{\omega}_2} \left(\left(\frac{\Delta_1}{\bar{\omega}_1}\right)^2 + \Delta_2 \left(\frac{\bar{\omega}_1^2 - \Delta_1^2}{\bar{\omega}_1^3}\right) \right) \right] (g\mu_B\delta B_0)^2 \\ & + \mathcal{O}(\delta B_0^3), \quad (13.11) \end{aligned}$$

with the second stage detuning $\Delta_2 = \bar{\omega}_1 - \omega_2$. The maximal suppression is achieved with a double-resonant drive with $\Delta_1 = 0$ and $\Delta_2 = 0$ as seen on fig. 13.3. But even with only one drive at resonance, the suppression is still large. The relative shift of the optical frequency is given by $\nu(\delta B) - \nu(0) = m_{2D}\bar{\omega}_{2D}(\delta B) - m_{2S}\bar{\omega}_{2S}(\delta B)$. So a higher B-field sensitivity caused by the magic angle detuning on the D-level can be compensated with an equal shift gradient on the S-level.

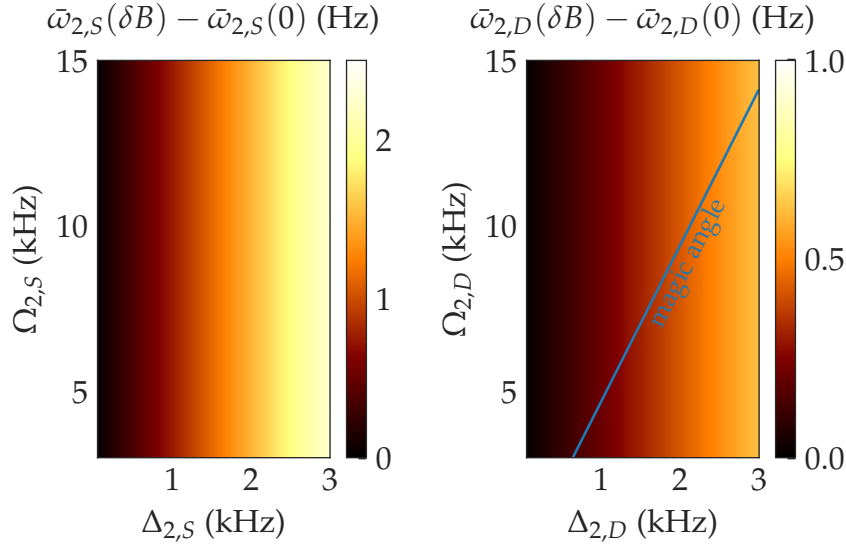


Figure 13.3: B-field shift of the relative line splitting of the doubly-dressed S-and D-transition. For the first stage $\bar{\omega}_{1S(D)} = 47$ kHz (115 kHz), a detuning of $\Delta_{1S(D)} = 1$ kHz and a magnetic field deviation $\delta B = 60$ nT are used for accounting of suboptimal first stage parameters.

It is important to also consider the influence of the timescales of the noise processes t_{noise} . In order to neglect its influences on the dynamics of the dressed states $\omega_i \gg 1/t_{\text{noise}}$ should be fulfilled. Therefore, the stronger drive should be used to suppress fast magnetic field noise with the bandwidth of $1/t_{\text{noise}} = n \times 50$ Hz, with n accounting for higher order terms of the mains line field.

13.2 Tensor shift suppression

In order to derive the QPS suppression in the dressed System, the quadrupole operator

$$Q_{ij} = \frac{3}{2} (J_i J_j + J_j J_i) - J^2$$

is used. Applying the transformations analogously to eq. (13.4) yields

$$Q^I = U_I U_2 U_1 Q U_1^\dagger U_2^\dagger U_I^\dagger \\ = \underbrace{(1 - 3 \cos^2 \theta_1)}_{\chi_1} \underbrace{(1 - 3 \cos^2 \theta_2)}_{\chi_2} \frac{3}{8} (J(J+1) - 3J_z^2).$$

The RWA was applied and off-diagonal terms are neglected. The degree of suppression is given by χ_1 for the first stage and χ_2 for the second. The suppression is maximal for the so-called *magic angle* θ_{χ_i} , defined by the condition $\cos \theta_{\chi_i} = \frac{1}{\sqrt{3}}$. The resulting detunings are given by

$$\Delta_{1,D} = \pm \frac{1}{\sqrt{8}} g_D \Omega_{1D}, \quad (13.12)$$

$$\Delta_{2,D} = \pm \frac{1}{\sqrt{32}} g_D \Omega_{2D}. \quad (13.13)$$

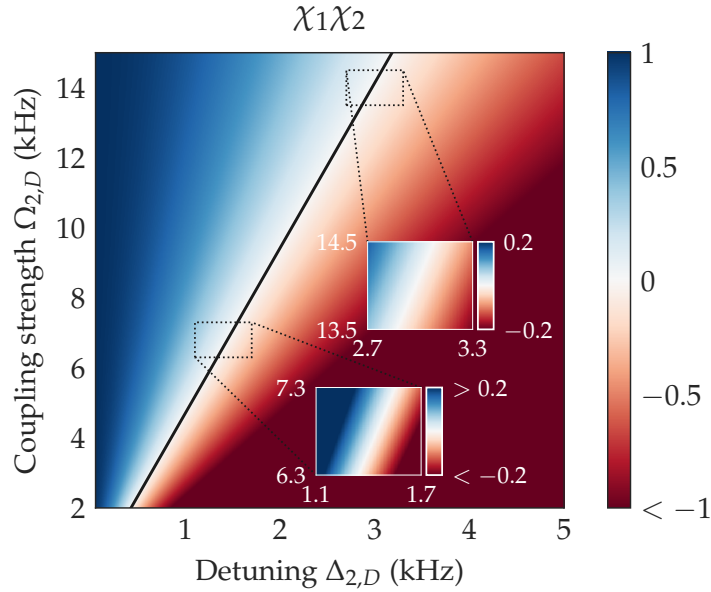


Figure 13.4: Suppression factor product $\chi_1 \chi_2$ of the QPS of a doubly-dressed transition with $\Delta_{1,D} = 0$ in dependence of the second stage detuning and coupling strength. The inset elucidates the needed parameter accuracy for a certain QPS suppression close to the magic angle. For stronger coupling the required accuracy decreases.

In this work, we apply the magic angle detuning on the second stage. This is justified by the larger frequency shift caused by magnetic field noise compared to the QPS. In the

next two chapters, measurement of the interplay between various frequency shift and their suppression using different CDD parameter sets are presented. The theoretical QPS suppression depending on the drive parameter for typical parameters is shown in fig. 13.4. For a 10-fold suppression of the QPS, the accuracy of the detuning has to match the magic angle condition within $\delta\Delta_{2D,\text{magic}} < 100$ Hz using $\Omega_{2D} = 6.8$ kHz. For a 100-fold suppression, this condition tightens to $\delta\Delta_{2D,\text{magic}} < 10$ Hz.

As seen in section 11.3.4, the TASS obeys the same dependency to the state's quantum numbers $\nu_{\text{TASS}} \propto h(J, m_J)$, therefore it is also suppressed by the CDD scheme.

Single ion results

14.1 Calibration

For estimating the dressed system's transition energies and properties, adequate knowledge of the used parameters is crucial. The frequencies ω_i of the driving fields can be chosen with high precision, whereas the coupling strengths Ω_i must be determined experimentally. A sequence of measurements is performed to characterize these values. The dressed system was investigated with different parameter sets. The complete sets can be found in table D.1.

First, the offset B-field is chosen so that the frequency splitting between the $|S_{1/2}, \frac{1}{2}\rangle$ and $|S_{1/2}, -\frac{1}{2}\rangle$ states is equal to 10 MHz or $B_0 = 0.3568$ mT. The frequency difference of two neighbouring ${}^2S_{1/2} \leftrightarrow {}^2D_{5/2}$ transitions is probed and the reference voltage of the static B-field stabilization is set accordingly. The accuracy of this is limited by magnetic field deviations on longer timescales as well as by the resolution of the voltage reference to $\delta B_0 + \Delta B_0 \lesssim 25$ nT. Additionally, fast fluctuations from the ac-mains line are present (section 5.2).

If not stated otherwise, the 729 nm laser beam is aligned parallel to the quantization B-field, so only $|\Delta m| = 1$ transitions can be addressed (compare fig. 11.9). Mostly, the dressed system close to the $|S_{1/2}, -\frac{1}{2}\rangle \leftrightarrow |D_{5/2}, -\frac{3}{2}\rangle$ transition is investigated in more detail.

First stage drive

At first, the 1st stage dressed system in the S- and D-manifold are investigated separately for a coarse calibration. After state preparation in $|S_{1/2}, -\frac{1}{2}\rangle$, the population is transferred with a 729 nm π -pulse to the $|D_{5/2}, -\frac{3}{2}\rangle$ state. Afterwards, an rf-pulse resonant to the ${}^2S_{1/2}$ splitting is applied together with another, frequency scanning 729 nm pulse. The splitting of the states $\bar{\omega}_{1S}$ is extracted and the coupling strength is given by:

$$\Omega_{1S} \underset{\Delta_{1S} \rightarrow 0}{=} \frac{2\bar{\omega}_{1S}}{g_s}.$$

Similar steps are taken for the D-stage calibration with resonance frequency $\omega_{1D} = 2\pi \times 10 \text{ MHz} * \frac{g_d}{g_s} = 2\pi \times 5.994\,905 \text{ MHz}$. No initial 729 nm pulse is needed for the D calibration. From the six newly produced states, the outer ones are probed for higher resolution with state splitting

$$5 \times \Omega_{1D} \Big|_{\Delta_{1D} \rightarrow 0} = \frac{5 \times 2\bar{\omega}_{1D}}{g_d}.$$

The usable pulse time is limited by dephasing of the non-dressed transitions under magnetic field fluctuations to $t_{\text{rf}} \approx 2.5 \text{ ms}$.

With knowledge of these parameters, the transition frequencies of all 12 1st stage transitions per Zeeman-level can be calculated approximately. This first step eases the unambiguous identification of the transitions, however, for a complete characterization, the corrections eq. (13.9) and eq. (13.10) have to be taken into account, so modified resonance frequencies must be used.

In order to refine the coupling strength determination from measured state splittings, both rf-drives are applied simultaneously. The transition frequencies of the four opposing transitions with quantum numbers

$$|m_{1S}, m_{1D}\rangle = \left(\left| +\frac{1}{2}, -\frac{5}{2} \right\rangle, \left| +\frac{1}{2}, +\frac{5}{2} \right\rangle, \left| +\frac{1}{2}, +\frac{1}{2} \right\rangle, \left| -\frac{1}{2}, +\frac{1}{2} \right\rangle \right)$$

are probed, and the line splittings are extracted.

In contrast to the coarse calibration explained above, this interrogation scheme allows for higher precision of the calibrated parameters, as here the cross-coupling effects are included. The full 1st stage states are also more robust against B-field variations. Thus, interrogation times of $t_r \lesssim 10 \text{ ms}$ without significant lost of contrast are possible.

If not denoted otherwise, the transition connecting dressed states with quantum numbers $m_{1S} = +\frac{1}{2}$, $m_{1D} = +\frac{1}{2}$ is investigated further.

Second stage drive

One major downside of CDD is the sensitivity to rf-drive fluctuations (compare section 14.3.2). Suppression of these is achieved with a weaker second stage coupling. Therefore, a modulated waveform is applied (see eq. (C.4)). The calibration of the 2nd stage parameters is done similar to the first ones. By observing

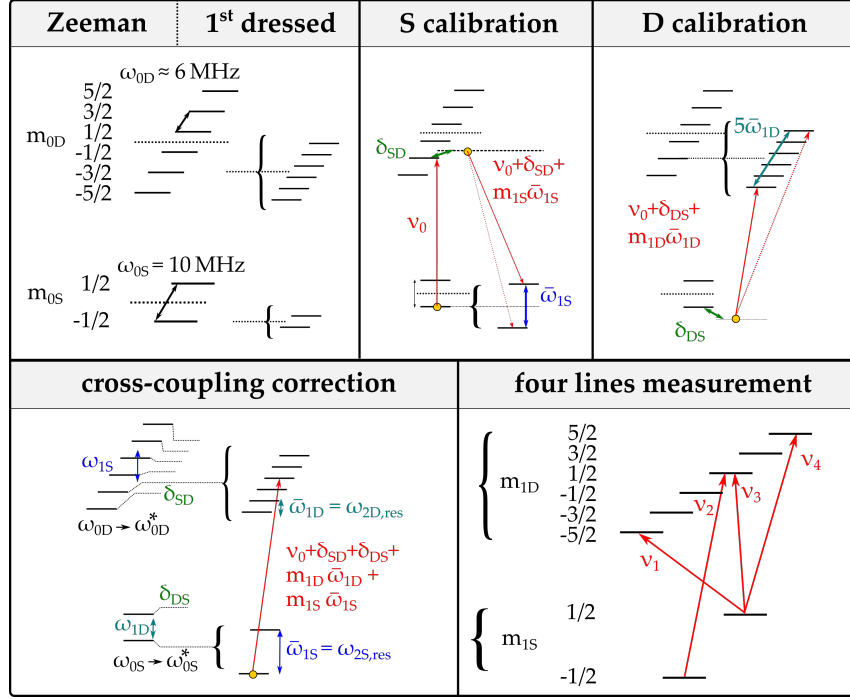


Figure 14.1: Sketch of the 1st-stage CDD calibration steps. Based on the Zeeman sub-levels of the $^2S_{1/2}$ and $^2D_{5/2}$ transitions the dressing fields are applied. For coarse calibration the S- and D-drives are applied separately. For finer calibration, both drives are applied simultaneously. Here, the cross-coupling effects have to be accounted for by a changed resonance frequency. Four lines are probed to deduce the coupling strengths of the full singly dressed transition. For simplicity, only the resonant case without detuning is displayed.

the line-splittings with respect to the first dressed state with resonantly chosen modulation frequency eq. (C.3)

$$\omega_{2S(D)} = \bar{\omega}_{1S(D)},$$

the 2nd-stage coupling strengths

$$\Omega_{2S} = \frac{4\bar{\omega}_{2S}}{g_s},$$

$$5 \times \Omega_{D2} = \frac{5 \times 4\bar{\omega}_{2D}}{g_d}$$

are characterized. Cross-coupling and Bloch-Siegert shifts are negligible for the second stage.

Several considerations have to be taken into account for choosing the driving parameters. The first stage coupling strength

determines the B-field noise suppression but also adds drive noise to the generated transitions. The 2nd stage coupling has to be strong enough to suppress this 1st stage noise, but weak enough to minimize its own drive noise. In addition, the second stage driving strength determines the maximal usable optical Rabi frequency Ω_{729} as the condition $\Omega_{2S(D)} \gg \Omega_{729}$ has to be fulfilled in order to average over the dynamic effects of the coupling and treat the dressed transition as quasi-static with respect to the laser frequency.

Adiabatic ramp

Abruptly switching on the S-drives will cause an unrestrained spread of the population of the dressed states. So, a two-stage

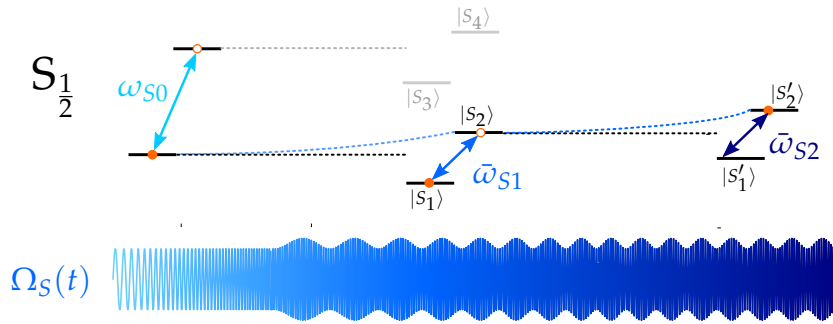


Figure 14.2: Sketch of the adiabatic sweep for preparation of the dressed ground state. Starting from the Zeeman ground state, a sequential frequency sweep of the carrier and modulation frequency transfers the population via the intermediate $|S_2\rangle$ level to the target level $|S'_2\rangle$. The simultaneous amplitude ramp is not shown for simplicity. Adapted from [103].

amplitude and frequency sweep on the S-drive (see eq. (C.1) and eq. (C.3)) is utilized to adiabatically transfer the population to the desired level. The target level $|S'_2\rangle$ is reached with high yield if the phase of the whole waveform is continuous without discontinuities between their individual parts (fig. 14.2). Therefore, the offset phases ϕ_{slow} , ϕ_{fast} of the carrier and modulation signal are adapted when combining the sweep and final waveforms. Simultaneously with the last step, the D-drive is switched on without need for adiabatic ramping. Typically, sweep times of $t_{\text{sw},1} = 500 \mu\text{s}$ and $t_{\text{sw},2} = 7 \text{ms}$ are used to ensure $\omega_i, \Omega_i \gg \frac{1}{t_{\text{sw},i}}$. Faster state preparation should be possible using quantum optimal control schemes [146] in the future. Changing the direction

of the frequency sweep populates the opposite transition. With this technique the target state is occupied with $P > 98\%$.

14.2 Optical coupling

The optical coupling strength of the individual dressed states is modified from the bare Zeeman levels (compare chapter 10). This section is adapted from [88]. The combined Hamiltonian for both ensembles is analogous to eq. (13.7) given by

$$H_{2,\text{tot}}^I = \bar{\omega}_{2S} J_{z,S} + \bar{\omega}_{2D} J_{z,D}.$$

The interaction of the laser with frequency ν_L with the electric quadrupole-allowed $^2S_{1/2} \leftrightarrow ^2D_{5/2}$ transition at frequency ν_a is described by

$$V_{E2} = \frac{iev_a}{2} \left(r_i r_j \partial_i A_j(\vec{R}, t) - \text{h.c.} \right),$$

with the vector potential $A(\vec{R}, t) = A^+(\vec{R})e^{i\nu_L t}$. Transforming to the rotating frame of the atomic transition frequency ν_a yields

$$V_{E2}^I = i \sum_{m_{0S}, m_{0D}} \left(\Omega_{m_{0S}, m_{0D}} |m_{0D}\rangle \langle m_{0S}| e^{-i\Delta\nu t} - \text{h.c.} \right),$$

with $\Delta\nu = \nu_L - \nu_a$. This equation is transformed by the rotations given in eq. (13.3) separately for each manifold,

$$\begin{aligned} V_{E2}^{\text{CDD}} &= \underbrace{(U_{ID} U_{2D} U_{1D})}_{U_D} \otimes \underbrace{(U_{IS} U_{2S} U_{1S})}_{U_S} V_{E2}^I \\ &\quad \underbrace{(U_{1S}^\dagger U_{2S}^\dagger U_{1S}^\dagger)}_{U_S^\dagger} \otimes \underbrace{(U_{1D}^\dagger U_{2D}^\dagger) U_{ID}^\dagger}_{U_D^\dagger} \\ &= i \sum_{m_{2S}, m_{2D}} \left(\bar{\Omega}_{m_{2S}, m_{2D}} |m_{2D}\rangle \langle m_{2S}| e^{-i\Delta\nu t} - \text{h.c.} \right), \end{aligned}$$

with

$$\begin{aligned} \bar{\Omega}_{m_{2S}, m_{2D}}(t) &= \sum_{m_{0S}, m_{0D}} \Omega_{m_{0S}, m_{0D}} \langle m_{2D}| U_D |m_{0D}\rangle \langle m_{0S}| U_S |m_{2S}\rangle \\ &= \sum_{m_{0S}, m_{0D}} \sum_{m_{2S}, m_{2D}} \bar{\Omega}_{2M} e^{iE_M t/\hbar}, \end{aligned}$$

using the abbreviation from eq. (13.8) and the state dependent bare Zeeman coupling strength $\Omega_{m_{0S}, m_{0D}}$. Here, the optical

coupling to an individual 2nd-stage transition $\bar{\Omega}_{2M}$ is introduced. For the intended use case, only one of the transitions is resonant with the applied laser.

The optical coupling to a individual 2nd-stage transition is simplified using Wigner D-matrix

$$\begin{aligned}
 d_{m_j, m_i}^j(\theta_i) &= \langle j, m_j | e^{-i\theta_j y} | j, m_i \rangle \\
 &= \sqrt{(j+m_i)!(j-m_i)!(j+m_j)!(j-m_j)!} \times \\
 &\sum_{k=k_{\min}}^{k_{\max}} (-1)^{m_j-m_i+k} \frac{\cos(\frac{\theta_i}{2})^{2j-2k+m_j-m_i} \sin(\frac{\theta_i}{2})^{m_j-m_i+2k}}{(j+m_i-k)!k!(m_i-m_j+k)!(j-m_i-k)!} ,
 \end{aligned} \tag{14.1}$$

with

$$\begin{aligned}
 k_{\min} &= \max(0, m_j - m_i) , \\
 k_{\max} &= \min(j + m_j, j - m_i) .
 \end{aligned}$$

The relative optical coupling strength is then given by

$$\begin{aligned}
 \frac{\bar{\Omega}_{2M}}{\Omega_{m_{0S}, m_{0D}}} &= \\
 &d_{m_{1D}, m_{2D}}^D(\theta_{2D}) d_{m_{0D}, m_{1D}}^D(\theta_{1D}) e^{-i\alpha_D(m_{2D}-m_{0D})-i\frac{\pi}{2}(m_{2D}-m_{1D})} \\
 &\times d_{m_{1S}, m_{2S}}^S(\theta_{2S}) d_{m_{0S}, m_{1S}}^S(\theta_{1S}) e^{i\alpha_S(m_{2S}-m_{0S})+i\frac{\pi}{2}(m_{2S}-m_{1S})} .
 \end{aligned} \tag{14.2}$$

Analogously, the relative optical coupling strength of the first stage transition is given by

$$\begin{aligned}
 \frac{\bar{\Omega}_M}{\Omega_{m_{0S}, m_{0D}}} &= d_{m_{0D}, m_{1D}}^D(\theta_{1D}) e^{-i\alpha_D m_{0D} - i\frac{\pi}{2} m_{1D}} \\
 &\times d_{m_{0S}, m_{1S}}^S(\theta_{1S}) e^{i\alpha_S m_{0S} + i\frac{\pi}{2} m_{1S}} ,
 \end{aligned} \tag{14.3}$$

following similar derivations.

It is worth to notice that the coupling strength for each ensemble scales with the underlying bare Zeeman coupling strength. Therefore, each ensemble inherits its selection rules as well as the dependence of the laser direction and polarization with respect to the quantization axis from the bare states. This has been verified experimentally. In fig. 14.3, the comparison of the measured and calculated optical coupling strengths for the first stage is displayed for two Zeeman ensembles addressed from two different laser-beam directions.

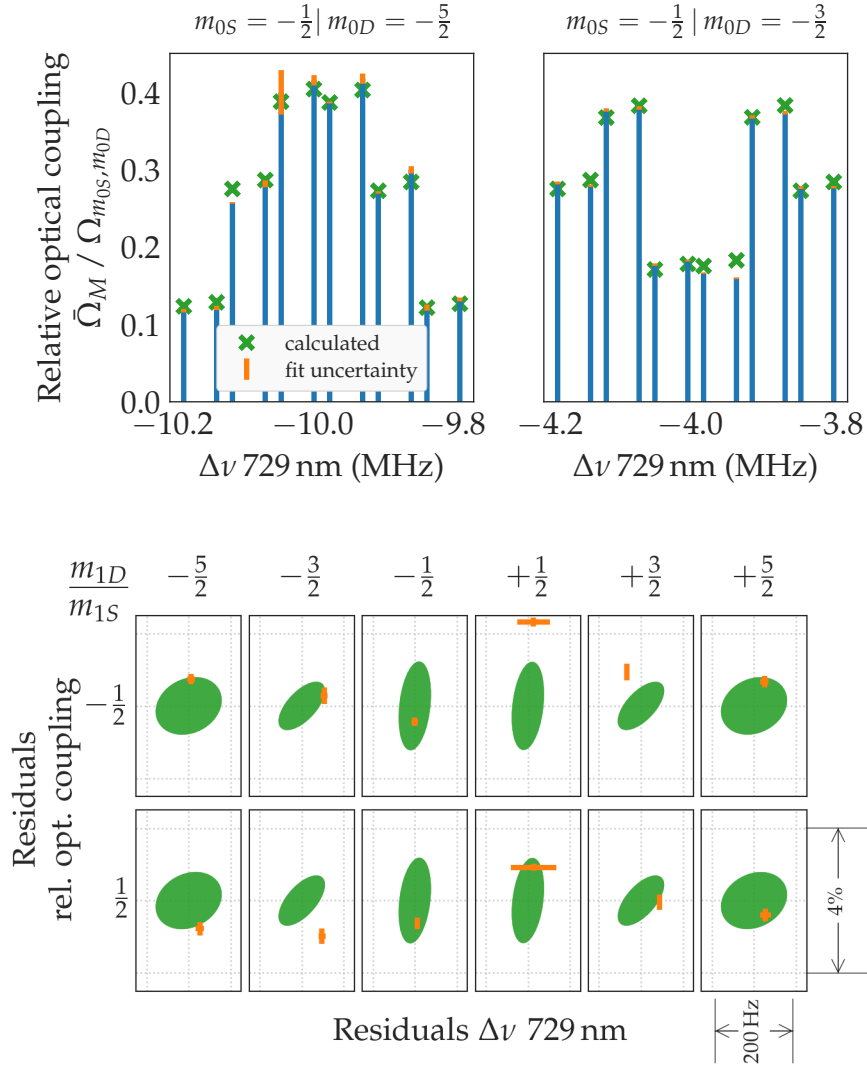


Figure 14.3: (a) Relative optical coupling strength of two 1st stage ensembles with $\theta_{1S(D)} = 90(3)^\circ(90(1)^\circ)$. Pulse length spectroscopy was used to determine the optical coupling strength of each transition. The relative coupling strength of the 729 nm beam with respect to the associated Zeeman transition is plotted against the frequency offset from the zero B-field transition frequency. (b) Residuals for the $m_{0S} = -\frac{1}{2}, m_{0D} = -\frac{3}{2}$ ensemble. The measured transitions values (orange) and the calculated (green) are compared. For the calculated uncertainty region, a fractional driving strength uncertainty of $\frac{\Delta\Omega_i}{\Omega_i} = 4 \times 10^{-4}$ and B-field uncertainty of $\Delta B_0 = 60$ nT is assumed. For the measured data, only the fitting uncertainty was taken into account [88].

The right ensemble with $m_{0D} = -\frac{3}{2}$ was probed axially, the other one diagonally (compare section 8.5). The centre frequen-

cies of the transitions are probed with spectroscopic pulses with $t_r > 1$ ms. The exact pulse time was adapted to maximize the excitation probability for each transition. The coupling strength was determined by a pulse length spectroscopy on the frequency centred transition. The fitting error for both measurements is displayed in fig. 14.3 (b). The theoretical predictions (eq. (13.8) and eq. (14.3)) are verified with the assumed uncertainty of calibration. Exact values can be found in table D.1. Deviations arise from calibration imperfections and thermally induced drive strength fluctuations (see section 14.3.2). Further predictions of eq. (14.2) like vanishing of dressed states for non-addressable Zeeman transitions (e.g. $|\Delta m| \neq 1$ for axial interrogation) and comparable relative scaling of the same ensemble illuminated from a different direction were qualitatively confirmed.

14.3 Frequency shift suppression

Suppression of the various frequency shifts depends on the chosen set of CDD-parameters. In addition, the drive noise induces a new artificial shift of the dressed transitions. The influence of different parameter sets on the suppression of these effects is described in this section. Suppression of the tensorial QPS on a five ion crystal is shown in section 15.3.

14.3.1 *B-field sensitivity*

Suppression of B-field variations on different timescales is influenced by the coupling strength as well as the detunings of the CDD drives. The largest suppression is achieved with an all-resonant driving scheme (see fig. 14.4), thus a first stage mixing angle of $\theta_i = 90^\circ \forall i$.

In fig. 14.4, the relative frequency deviation with changing static magnetic field is displayed for three different parameter sets. A quadratic approximation reveals the sensitivity of $-1.2(1) \times 10^{-4} \text{ Hz/nT}^2$ for full coupling and $-1.4(2) \times 10^{-3} \text{ Hz/nT}^2$ for half coupling and magic angle drive (section 15.3). The used parameter sets are summarized in table D.1.

In order to measure the sensitivity of the doubly dressed transition to B-field deviations $\frac{\partial \nu_i}{\partial B_0}$, the static magnetic field is altered by varying the offset B-field current, and the resulting frequency shift of one doubly dressed transition is observed. For each B-field value, the 729 nm laser frequency was scanned and the centres of the transitions are determined. With altered Zeeman

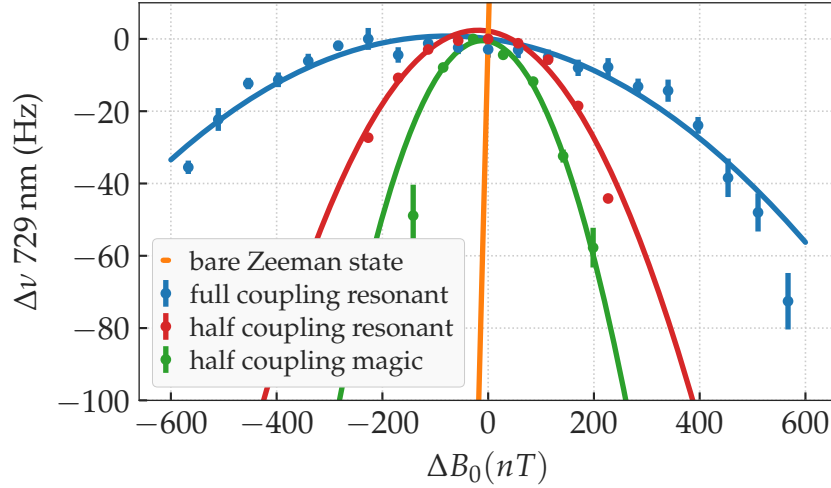


Figure 14.4: Suppression of magnetic field sensitivity on the 2nd stage CDD transition. Comparison of static B-field sensitivity for different parameter sets (compare appendix D). The data was approximated with a 2nd degree polynomial function. For comparison, the calculated shift of the least sensitive bare atomic Zeeman transition $|S, -1/2\rangle \leftrightarrow |D, -1/2\rangle$ with $\frac{\Delta\nu_a}{\Delta B_0} = 5.6 \text{ Hz nT}^{-1}$ is shown.

splitting, all detunings Δ_i are changed, therefore the optical coupling is also affected via the mixing angle variation (eq. (13.5)). Thus, side-of-fringe measurements must be corrected for this effect (see appendix F). The fitted transition centres obtained by laser frequency scans are less effected by optical coupling strength changes. However, this method takes longer, so it is prone to long term laser drifts and/or B-field deviations if the resolution is not drastically reduced.

Typical slow magnetic field deviations are shown in fig. 14.5. In connection with the measured magnetic field sensitivity, the frequency stability caused by magnetic field deviations can be estimated (fig. 14.6). Here, also the limited resolution of the B-field stabilization ΔB_0 , thus the deviation from the minimum sensitivity was taken into account.

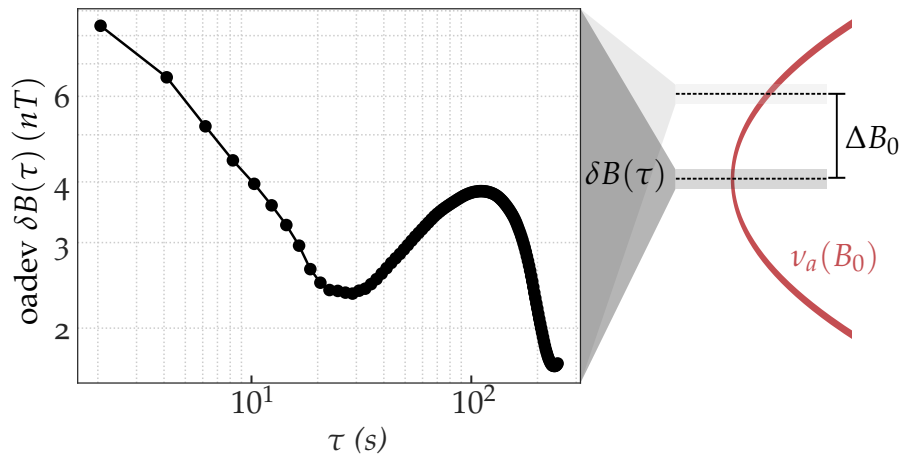


Figure 14.5: Overlapping Allan deviation of typical magnetic field noise δB_0 with active B-field stabilization. Measured at the $|D_{5/2}, -\frac{3}{2}\rangle$ transition with the Ramsey method. On the right side, the influence of such fluctuations on a decoupled line with magnetic offset field-dependent frequency shift $\nu_a(B_0)$ is indicated. Here, also any static B-field offset ΔB_0 from the minimum of the shift sensitivity influences the spread of the resulting shift.

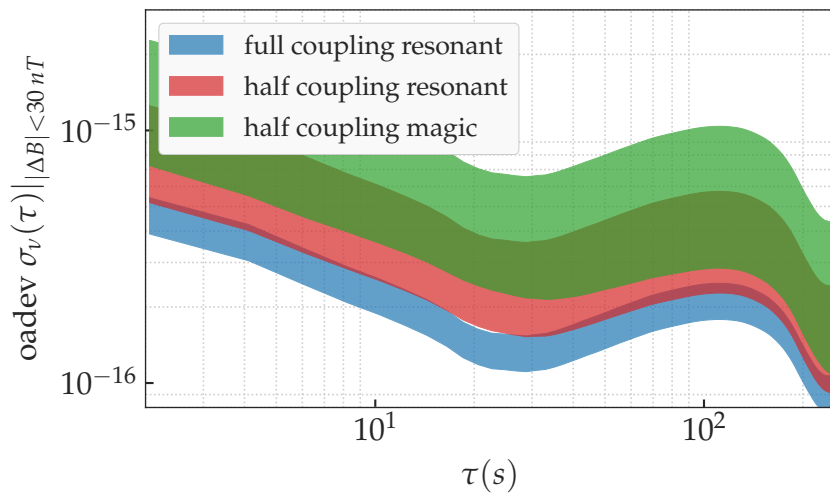


Figure 14.6: Simulated overlapping Allan deviation of the CDD-transition under magnetic field noise $\delta B_0(t)$ depending on the static offset ΔB_0 from the field with minimal sensitivity (compare fig. 14.5 and fig. 14.4). Frequency shifts are simulated for typical B-field fluctuations $\delta B(t)$ for three different CDD-parameter sets within a region $|\Delta B_0| \leq 30$ nT around the minimal shift sensitivity. The coloured bands represent the calculated stabilities extrema within this region.

14.3.2 Coupling strength fluctuations

The second important measure for temporal and spatial variation of the transition is the sensitivity to changes in coupling strength. They can have different causes. The presented driving source as well as the rf-coils (see chapter 7) are prone to environmental perturbations, primarily thermal changes. The sensitivity is characterized by observing frequency shifts of the doubly dressed transition with respect to amplitude changes (fig. 14.7). The amplitude change was applied on the AWG output stage, resulting in a common rf-amplitude change on S- and D-drive.

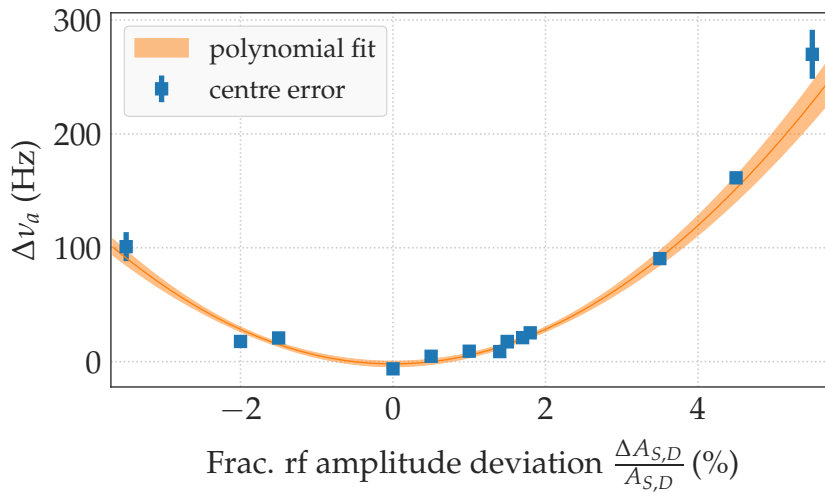


Figure 14.7: Frequency sensitivity to AWG output amplitude changes of the doubly dressed transition. The polynomial approximation reveals a sensitivity of $3.0(2) \times 10^5 \text{ Hz} \left(\frac{\Delta A_{S,D}}{A_{S,D}} \right)^2$

The stability of the coupling strength is inferred by measuring the time dependence of four first stage transitions using the Ramsey method (fig. 14.8). As the four interrogations were performed successively within one experimental cycle, their relative frequency difference is independent of slow magnetic field and laser fluctuations. The frequency resolution is limited by QPN at the used probe time. Therefore, it can only be seen as an upper bound for shorter times. The long term stability of $\frac{\Delta \Omega_i}{\Omega_i} \lesssim 6 \times 10^{-5}$ is caused by a combination of the amplitude stability of the used AWG, amplifier and changes in the RLC of the rf-coils.

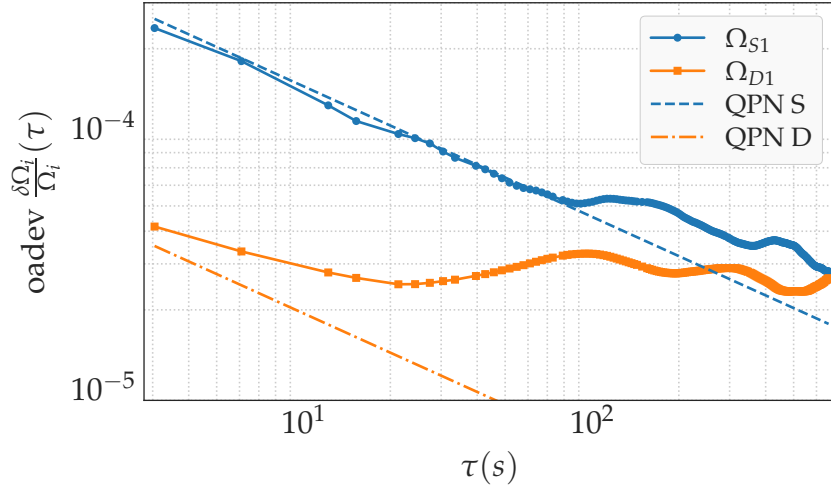
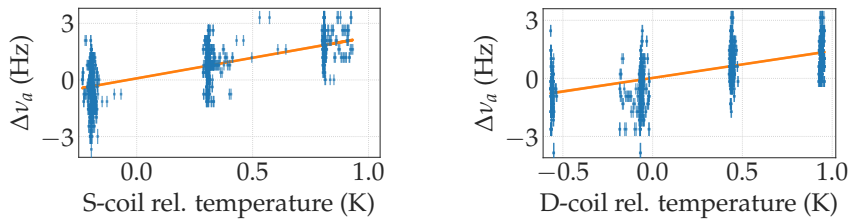


Figure 14.8: Overlapping Allan deviation of the fractional coupling strength Ω_{S1} , Ω_{D1} . The coupling strength is extracted from the frequency splitting of four 1st stage lines. The lower short time stability for the D-state coupling is due to the larger absolute frequency splitting of the outer states of the manifold and equal absolute QPN for each line. In contrast, for the S-levels QPN limits the measurement up to $\tau \lesssim 100$ s.

Due to the superimposed QPN, no significant correlation between $\Omega_S(t)$ and $\Omega_D(t)$ is visible in the dataset for short times. Nevertheless, due to the proximity of the two rf-chains, a common dependence on e.g. laboratory temperature changes is reasonable, making common fluctuations likely.



(a) S-coil temperature sensitivity $\frac{\Delta\nu}{\Delta T_S} = 2.18(7) \text{ Hz K}^{-1}$ (b) D-coil temperature sensitivity $\frac{\Delta\nu}{\Delta T_D} = 1.39(5) \text{ Hz K}^{-1}$

Figure 14.9: Sensitivity of the doubly dressed transition to coil temperature changes. The set-point of the included temperature stabilization was altered and the frequency deviation of the transition was observed via the Ramsey method with 50 ms dark time. Individual points are limited by QPN.

Measurements with a previous coil design showed a 10 times higher drive instability. So using components with low temperature coefficient, a low Q-factor and temperature stabilization of the RLC-electronic parts made a big impact on the performance (see chapter 7). The frequency response to temperature changes of the rf-coil temperature stabilization is shown in fig. 14.9. Faster amplitude noise can not be measured with this method, since the frequency resolution is limited by QPN. However, a coarse prediction can be made with the minimal attainable linewidth of a frequency scan on a first stage dressed transition. The minimal linewidth was 44(3) Hz for the parameters displayed in table D.1 giving a coarse estimated limit for the short term stability of $\frac{\Delta\Omega_{D1}}{\Omega_{D1}} \approx \frac{\Delta\tilde{\omega}_{D1}}{\tilde{\omega}_{D1}} = \frac{\Delta\tilde{\omega}_{D1}}{g_D\Omega_{D1}/2} = 6 \times 10^{-4}$. Here, only the larger coupling strength $\Omega_{D1} = 115$ kHz was taken into account and B-field contributions are neglected.

A drawback of the used design is that the rf-power of up to 3 W is dumped into the RLC-circuit, causing a significant heating of up to 10 K. Especially, large changes in the rf-pulse duty cycle cannot be fully compensated by the temperature stabilization. Alternative designs similar to [118] may prevent this shortcoming in the future by splitting the circuit into a radiating transfer line and a dedicated termination. Amplitude noise of the driving source and amplifier could be stabilized in the future with a suitable power stabilization. An alternative is lowering the distance to the ions and therefore lessening the power demand. This would make a dedicated in-vacuum electric path mandatory. All dc-electrodes of the used trap are filtered on chip and the trap components are carefully optimized, therefore a new chip design with dedicated rf-signal lanes is advisable. Another option to further mitigate the effect of amplitude noise is the usage of an additional 3rd-stage CDD drive with reduced amplitude [1].

14.4 Linewidth and stability

In the presented experiment, the clock laser was not actively stabilized to the clock transition due to shortcomings in the experimental control system. Nevertheless, as the 729 nm laser was referenced to the stable Si cavity (section 8.4.4), we can treat the laser as a stable reference for the shown measurements even for longer times. The achievable linewidth of the $|S_{1/2}, m_{1S} = +\frac{1}{2}, m_{2S} = +\frac{1}{2}\rangle \leftrightarrow |D_{5/2}, m_{1D} = +\frac{1}{2}, m_{2D} = +\frac{1}{2}\rangle$ transition as well as its shape reveal the performance of the CDD

scheme. The linewidth of the transition was probed by a frequency scan of the steering AOM. The frequency scan shown in fig. 14.10 was taken in three runs over a period of 77 min and averaged afterwards. The frequency resolution is already limited by the resolution of the used DDS¹ to 0.4 Hz.

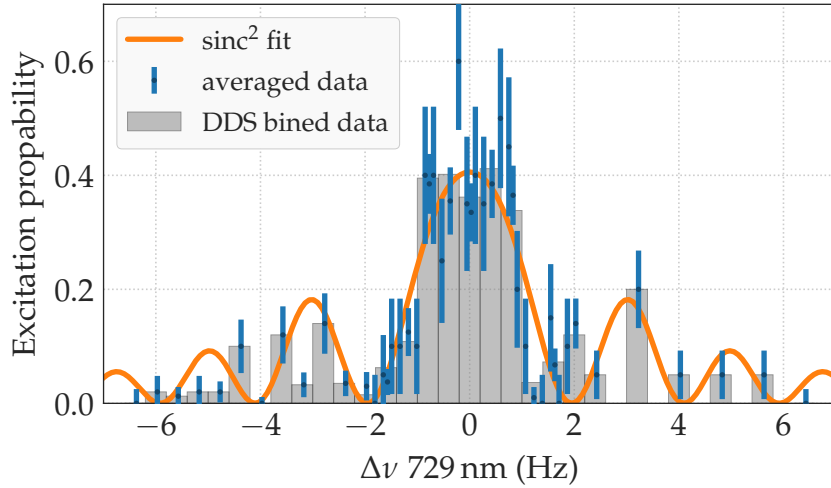


Figure 14.10: Frequency scan of one doubly dressed transition. The data points of three measurements with different resolution is averaged (blue). The frequency steps in software are finer resolved than possible with the DDS, therefore the data is binned according to the limited resolution (grey). The sinc^2 fit (orange) provides a linewidth of 2.2(4) Hz, with the uncertainty given by the smallest possible frequency step.

The measured linewidth of $\Delta\nu_{\text{FWHM}} = 2.2(4)$ Hz is close to the Fourier limit of the applied rf-pulse with length $t_{\text{rf}} = 620$ ms. The latter is only technically limited by the memory size of the used AWG. Deviation from the Fourier limit might arise from a mismatch of the optimal Rabi pulse area as well as residual B-field and drive noise. The maximum excitation probability of $P = 0.44(4)$ is lower than the expected decay limit of 0.588 associated with the natural life-time of $\tau = 1168(9)$ ms [72]. Also leaking light of the clear-out laser at 854 nm can reduce the contrast and linewidth. Without a shutter for the clear-out and re-pumper lasers, state decay of the $^2\text{D}_{5/2}$ was limited to $t_{\text{coh}} \lesssim 100$ ms by insufficient suppression of leaking light through the used AOMs.

A Ramsey interrogation on the same transition is used for a long term stability measurement (see fig. 14.11). The rf-signals

¹ based on AD9910, Analog Devices

are applied as described in section 14.1, but with an alternative 729 nm pulse sequence: The opening and closing $\frac{\pi}{2}$ pulses have a duration $t_{\text{puls}} = 1 \text{ ms} \gg \frac{1}{\Omega_{2S(2D)}}$ to avoid population of nearby dressed states. The Ramsey dark time $t_{\text{dark}} = 60 \text{ ms}$ was chosen so that frequency deviations are small enough to stay on one slope of the Ramsey fringe for longer periods, even without feedback to the clock laser. A previous frequency scan was used for calibration of the shape of the given Ramsey fringe.

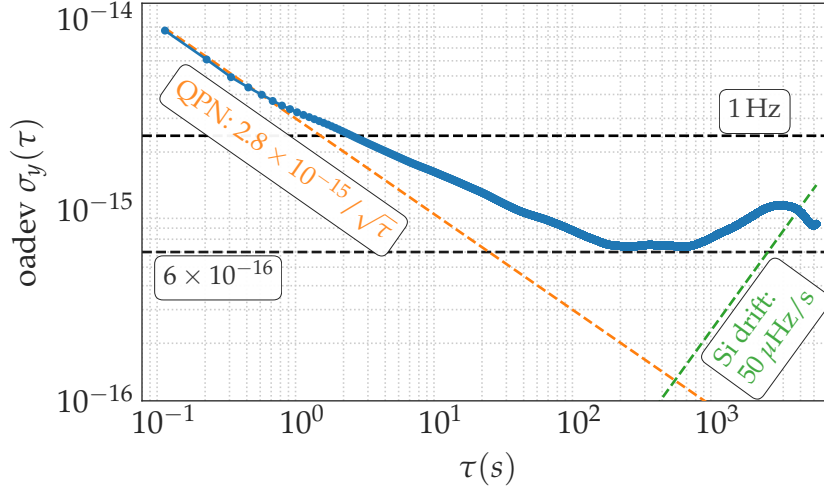


Figure 14.11: Overlapping Allan deviation of the doubly-dressed transition with Ramsey interrogation using 60 ms dark time.

For short averaging times, the Allan deviation scales with $\sigma_y(\tau) \propto 1/\sqrt{\tau}$ according to the QPN-limit of $2.8 \times 10^{-15}/\sqrt{\tau}$ (compare eq. (3.1)). The scaling changes at $\tau \gtrsim 1 \text{ s}$ to $\sigma_y(\tau) \propto \tau^{-1/3}$ and flattens out to $\sigma_y(\tau) \approx 6 \times 10^{-16}$ from 200 s to 700 s. For longer times, a frequency drift is visible. For comparison, the linear drift of the Si-cavity is shown, although it is compensated in our setup as described in section 8.4.4.

The flicker frequency scaling at a few 100 s is caused by the coupling strength instability (see. fig. 14.8).

The medium term scaling cannot be described by standard noise processes [110]. Since the reason for the limited performance and unique scaling is not clear, several possible sources are discussed in the following.

From the simulation shown in fig. 14.6, stability limitation by magnetic field fluctuations are at $\sigma_y \lesssim 2 \times 10^{-16}$ around 100 s, so they are not the limiting factor for this measurement. However, altered parameter sets provide less magnetic field suppression.

729 nm laser noise might also limit the stability. Although transfer-locking to the Si cavity should result in a non-limiting stability for the shown measurements (compare section 8.4.4) a permanent closed-loop comparison of the transfer-lock performance is missing. The used transfer-lock scheme is sensitive to the amplitude of the fast noise of the comb lines, which typical changes on a timescale of days. As a consequence, occasional fringe hops of the phase of the locked laser are possible, which leads to a drift of the laser frequency. To track this in real time, fast recording and analysis of the error signal or a close-loop comparison via another comb is needed.

Another origin of frequency noise are residual unstabilized optical paths (see section 8.4.3) between the stable referenced point and the position of the ion crystal. As shown in section 8.4.3, they pose no limitation on the scale of the shown measurement. Phase chirps induced by large power changes of the drive source of the AOMs [23] are qualitatively excluded, by comparing a Ramsey with a Rabi interrogation. The measured stability for the two measurements is comparable, although for the Ramsey pulses, shorter, much stronger driving pulses are applied to the AOM.

A possible explanation is the unsteady heating of the rf-coils. The temperature stabilization of the coils has a time constant of few 10 s, but short-term temperature fluctuations depend strongly on the length of the pulses and the gaps without an rf-signal. Within these gaps convective and conductive heat transfer cools the coils. In contrast to the strictly timed core sequence, there is an erratic temporal gap, after each cycle-bunch. Within this gap, transfer of PMT counts from the FPGA to the control PC and upload of new sequence control files is done (chapter 6). As a consequence, the duty cycle of the rf-drive and with it the coil temperature is slightly changed for each data point. Within each cycle-bunch, there is a steady heat build-up until the next gap. This behaviour was not investigated in detail, but with the planned new experimental control hardware and software (chapter 17), the nondeterministic timings will be eliminated.

14.4.1 *Rabi oscillations*

Rabi oscillations are a frequently used tool for determining the a priori unknown coupling strength on the ion's transitions (chap-

ter 10). In addition, information about decoherence processes can be extracted.

In the case of the presented dressed states system it is of particular interest because its state density is high. The ten bare Zeeman $^2S_{1/2} \leftrightarrow ^2D_{5/2}$ states split up in $10 \times 12 \times 12 = 1440$ lines for the 2nd stage, from which a quarter remains after S-level state preparation. Selection rules depending on the laser direction reduce this number further. The spectrum of the 729 nm laser needs to have sufficient low phase noise over a large frequency band to avoid off-resonant excitation from these transitions. In addition, power broadening of laser intensity as well as the bandwidth-limited linewidth have to be small enough to ensure sole excitation of one transition. For long pulse durations and low laser intensity, long coherence times could be observed (fig. 14.12). Deviations from the natural lifetime limit arise from incomplete noise suppression.

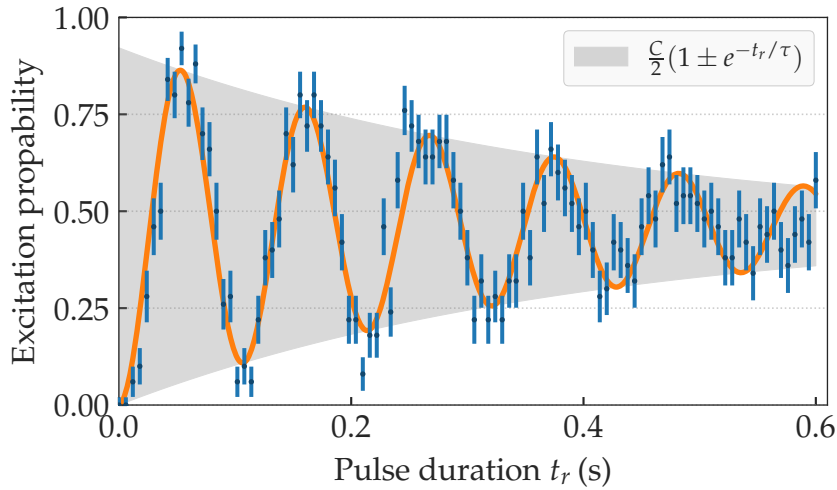


Figure 14.12: Pulse time scan on the 2nd stage dressed transition. The data was modelled with the function $P(t) = \frac{C}{2}(1 - \cos(2\pi f t_r)) e^{-\frac{t_r}{\tau}}$. The coherence decay time $\tau = 0.397(33)$ s is approximately a third of the natural lifetime decay limit of the $^2S_{1/2} \leftrightarrow ^2D_{5/2}$ transition of $t_{\text{nat}} = 1.165(11)$ s [72].

For stronger optical coupling, off-resonant scattering to nearby dressed states becomes important. Figure 14.13 illustrates this limitation. For optical coupling strengths $\Omega_{\text{opt}} \lesssim 250$ Hz, excitation of nearby states is only a minor perturbation. With increasing coupling strength this becomes more significant. Here the contrast of the Rabi-oscillations decays significantly. The exact limit depends on the spectrum of the CDD-transitions,

thus from the chosen parameter set and the shape of the 729 nm pulse. In practice, the ultimate usable minimal coupling strength of the second stage drive is limited by this addressability of a sole transition. For this reason, the choice of a dressed transition with large relative optical coupling strength is advantageous.

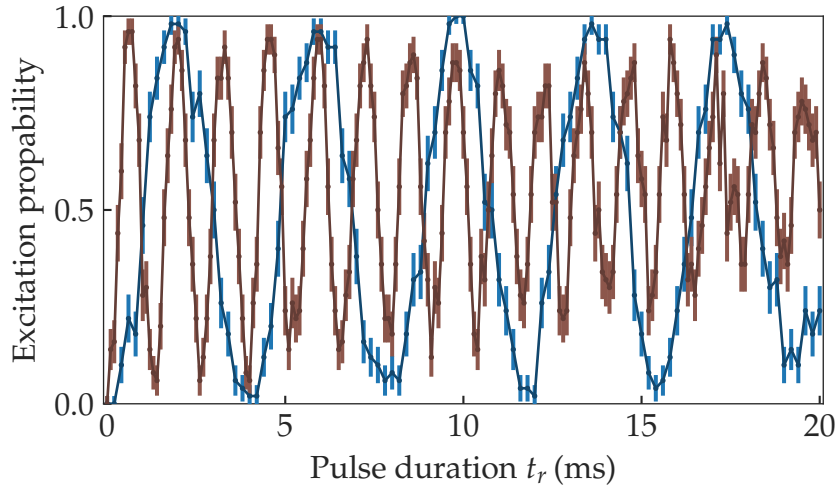


Figure 14.13: Rabi oscillations of the 2nd stage dressed transition for two 729 nm light intensities. With optical coupling strengths of $\Omega_{\text{opt}} = 257.7(3)$ Hz (blue) only small deviations from full contrast Rabi oscillations are visible. For $\Omega_{\text{opt}} = 777.1(12)$ Hz (brown) a significant dephasing from spurious excitation of neighbouring states occurs. Lines are a guide for the eye.

In this section it was shown that the magnetic-field suppression of the first order Zeeman shift by CDD enables usage of a long coherence time on the artificial transition. In fact, the data used for fig. 14.12 and fig. 14.10 was taken without any active or passive magnetic-field stabilization. The measured residual magnet-field sensitivity of $-1.2(1) \times 10^{-4}$ Hz/nT² is comparable to e.g. the quadratic Zeeman shift in $^{27}\text{Al}^+$ of $-7.1988(48) \times 10^{-5}$ Hz/nT². This emphasizes the potential of designing artificial transitions with tailored properties.

Multi-ion results

Multi-ion operation of optical frequency standards is favourable to overcome the high statistical uncertainty by QPN for a single ion clock [78]. Several challenges must be overcome to accomplish this. The inhomogeneous line shifts caused by strong trapping field gradients (section 13.2) pose a limitation to some species, while e.g. $^{27}\text{Al}^+$ and $^{115}\text{In}^+$ benefit from a negligible quadrupole moment Θ . The excess micromotion along the axial nodal line is sufficiently small for the trap design used in our setup [67] to support several ions. Especially for lighter elements, motional shifts need to be reduced by suitable multi-ion cooling schemes. This is counteracted by lower axial trapping frequencies needed for storing larger linear ion strings by the increasing Lamb-Dicke parameter. Designed non-harmonic trapping potentials offer an altered mode structure [63], which might be beneficial for some aspects. We have experienced a shorter duration of an ion crystal staying crystallized for larger crystals. This effect is explained by a combination of more frequent collisions with residual gas atoms and anomalous heating if the condition $\Omega_{\text{rf}} = n_x\omega_x + n_y\omega_y + n_z\omega_z$ with $n_{x,y,z} \in \mathbb{Z}$ is fulfilled [27]. After a collision, the ion is displaced, thus sampling a larger volume of the residual anharmonic contribution of the trapping potential. With increasing ion number, these conditions are fulfilled more often. For a five-ion crystal these events happen on a minute timescale. A change of the radial trapping potential can force re-crystallization of the ions. However, for larger crystals this might pose a serious limitation for the operation of long spectroscopic experiments.

This section focuses on the investigation of the QPS as well as other inhomogeneous frequency shifts.

15.1 Crystal shape

The inherent inhomogeneous quadrupole shift (QPS) broadens the $^2\text{S}_{1/2} \leftrightarrow ^2\text{D}_{5/2}$ transition in an ion crystal due to different electric field gradients at the ion positions. The shape of the electric field is composed by the potentials generated by the voltages applied to the Paul trap and the charge distribu-

tion of the trapped ions. So the shift is calculated for a given crystal configuration. The energy of the combined potential is minimized with respect to the ion positions for given secular trapping potentials and ion number to simulate the ion positions (appendix A). With this, the electric field gradients at the ion positions

$$\left. \frac{\delta E_i}{\delta r_{j,n}} \right|_{\vec{r}_n = \vec{r}_{n,\min}}$$

is calculated, and the quadrupole shift is determined (fig. 15.1).

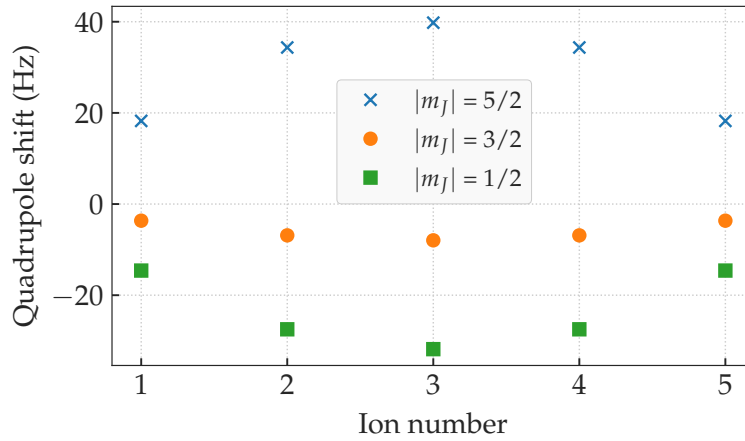


Figure 15.1: Calculated quadrupole shift of the ${}^2D_{5/2}$ transition for a linear five-ion crystal with $(\omega_{\text{ax}}, \omega_{\text{rad},x}, \omega_{\text{rad},y}) = 2\pi \times (662, 1827, 1899)$ kHz and 729 nm Euler angles of $\alpha, \beta, \gamma = 0$ depending on the Z-component of the total angular momentum m_J .

First, we identify an ion crystal with advantageous parameters. This configuration should offer a large relative quadrupole shift and small axial Lamb-Dicke factor for efficient cooling. From simulations of the QPS, a linear crystal close to the phase transition to a 2D-configuration is preferable, because this maximizes the relative electric field gradient along the ion string. The phase transition point is determined by the critical anisotropy parameter $\alpha = \left(\frac{\omega_{\text{ax}}}{\omega_{\text{rad}}}\right)^2$ and number of ions, N . An empirical approximation is given by [33]:

$$\begin{aligned} \alpha_{\text{crit}} &= 2.94 N^{-1.80}, \\ \omega_{\text{ax,crit}} &= \sqrt{\alpha_{\text{crit}}} \omega_{\text{rad,max}}. \end{aligned} \quad (15.1)$$

For the exact solution, the potential is minimized with respect to the ion positions (appendix A). In practise, with a given limi-

tation of the radial confinement, we have to choose an adequate ion number for acceptable axial confinement. For low confinement, the Lamb-Dicke parameter becomes too large, resulting in worse laser cooling performance. In our setup, these requirements are fulfilled with a confinement of $(\omega_{ax}, \omega_{rad,x}, \omega_{rad,y}) = 2\pi \times [622(2), 1827(10), 1899(10)]$ kHz and five ions. With this configuration, the linear ion crystal has an axial expansion of $20.4 \mu\text{m}$. The simulated QPS for this configuration is displayed in fig. 15.1. In the following, the transition to $m_J = -\frac{3}{2}$ is investigated.

15.2 Inhomogeneous fields

Despite the QPS, there are two major inhomogeneous line shifts to take into account on linear crystals: The static B-field inhomogeneity $\frac{\partial B_0}{\partial z}$ along the crystal as well as the inhomogeneous coupling strength $\frac{\partial \Omega_i}{\partial z}$ arising from the shape of the dressing coils. Although these inhomogeneities are only technically induced, their magnitude has to be characterized for a complete evaluation.

To characterize the rf-field inhomogeneities, the same measurement on four 1st stage transitions as described in section 14.1 is employed, but now on a string of ions. Synchronized camera data readout enables state detection of individual ions, described in section 9.1. If the coupling strength is much larger than the inhomogeneous resonance shift caused by the static B-field differences, thus $\Omega_i \gg \Delta_{i,n}$ for all ions, the latter can be neglected. The relative deviations per ion are displayed in fig. 15.2a. This kind of measurement was used to optimize the pointing of the coils for minimal inhomogeneity, limited by centre prediction of the broadened transition. This could be improved by longer averaging. In addition, the RLC-circuits of the two coils are coupled by near field interactions, so even slight position changes on one coil influences the field of the other making accurate adjustments difficult.

A larger coil-diameter to ion-distance ratio should improve the homogeneity, despite local distortions of the field by the Paul trap electrodes counteracting this.

A linear approximation of the fractional coupling strength inhomogeneity gives $\frac{\delta \Omega_S}{\delta z} \frac{1}{\Omega_S} = -6.2(53) \times 10^{-6} \mu\text{m}^{-1}$ for S-levels and $\frac{\delta \Omega_D}{\delta z} \frac{1}{\Omega_D} = 6.0(5) \times 10^{-6} \mu\text{m}^{-1}$ for the D-level along the five ion crystal.

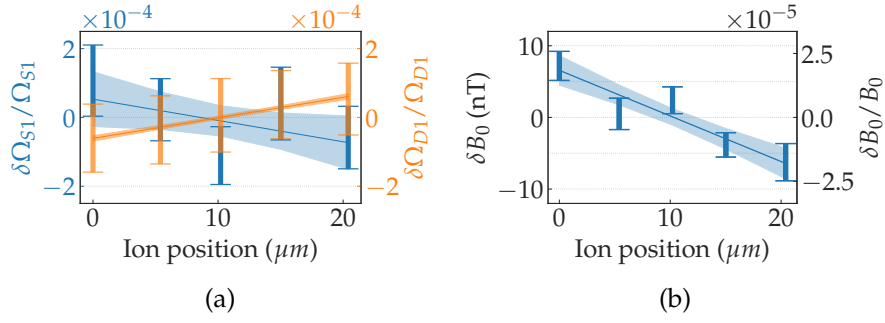


Figure 15.2: Fractional spatial inhomogeneity of (a) coupling strength and (b) B-field along a five ion string. The position of the ions in the crystal was simulated. For each ion the centre of the transition lines was fitted and the associated field shift was calculated. The error-bars reflect the uncertainty in finding the line centres. Shaded areas reflect the confidence intervals of the linear approximations.

The B-field inhomogeneity was measured on the $|D_{5/2}, -\frac{3}{2}\rangle$ transition without suppression of the field by CDD. So here, fast magnetic field fluctuation pose the major uncertainty to the line centres. The evaluation of these inhomogeneous effects along the ion crystal is shown in fig. 15.2b. The measured static B-field inhomogeneity is $\frac{\delta B_0}{\delta z} = -0.64(14) \text{ nT } \mu\text{m}^{-1}$ along the crystal at an offset field of $B_0 = 0.35680(3) \text{ mT}$. This inhomogeneity is larger than estimated from field simulations (compare chapter 5). Even if an unrealistically large displacement of the ion crystal centre with respect to the field centre of 5 cm is assumed, the simulated inhomogeneity is $\frac{\delta B_0}{B_0} < 2 \times 10^{-5}$ for the five ion crystal. The discrepancy might arise from distortion by the surrounding opto-mechanical components and the vacuum chamber parts. This could be compensated in the future with an additional inhomogeneous external field.

15.3 Quadrupole shift suppression

Resolution of small relative frequency shifts of the CDD transition was shown in section 14.4 with a measured linewidth of a CDD transition of 2.2(4) Hz. However, the absolute accuracy is limited by the calibration process as discussed in section 14.1. Therefore, measuring the relative QPS along a crystal is preferred over e.g. frequency shift measurements of a single ion with altered trapping potential [126]. Additionally, this is a more stringent test for the envisioned application of frequency stabilization to the CDD transition in larger crystals, as it in-

cludes also all other inhomogeneous effects like static B- and rf-field inhomogeneities (section 15.2).

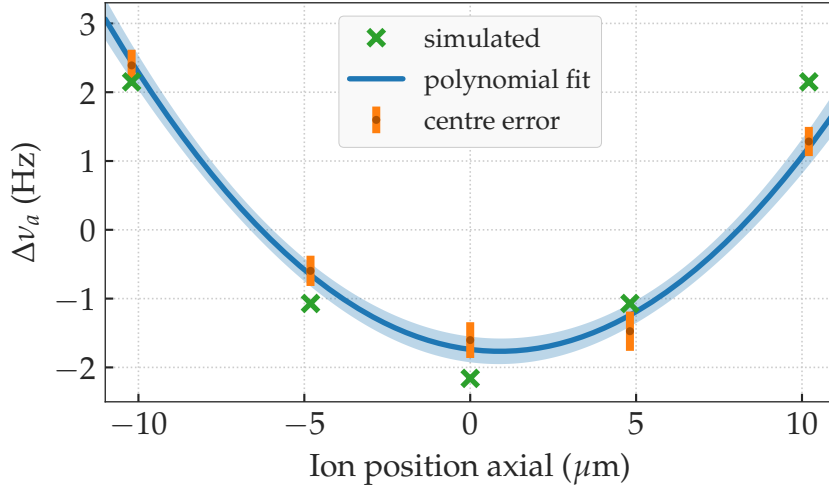


Figure 15.3: Frequency shift of the 2nd stage dynamical decoupling transition of a five ion crystal with resonant parameter set (table D.1). The centres of the spectroscopic lines of the camera data are shown for the individual ions. Measured data is compared with the simulated QPS on the $|D_{5/2}, -\frac{3}{2}\rangle$ transition. The 2nd degree polynomial fit $f(x) = c_0 + c_1x + c_2x^2$ reveals parameters of $c_1 = -0.06(1)$ Hz/ μm and $c_2 = 0.034(2)$ Hz/ μm^2 . The shaded area reflects its confidence interval.

First, the all resonant CDD drive (see table D.1) is applied to verify the simulated magnitude of the QPS. This measurement shown in fig. 15.3 is maximally suppressing magnetic field deviations, but not the QPS. It is compared to the simulated QPS on the bare $|D_{5/2}, -\frac{3}{2}\rangle$ transition, which was shown in fig. 15.1. The quadratic shape of the shift is clearly visible. The unsymmetrical distortion of the measured lines reflects the remaining shift arising from the rf-field inhomogeneities.

Next, the magic angle detuning is applied on the 2nd stage drive to suppress the shift. For the measurements shown in fig. 15.4, the second stage D detuning was detuned by $\Delta_{D2} = \frac{1}{\sqrt{32}}(g_d\Omega_{D2})$. For reducing the effect of inhomogeneous rf-fields, all coupling strengths were reduced by roughly a factor of two for this measurement (see table D.1).

With magic angle detuning, the quadratic dependence of the shift is reduced by a factor $\frac{c_{2,\text{res.}}}{c_{2,\text{mag.}}} = 12$ compared to the resonant case, but the total shift along the crystal is comparable due to the larger linear contribution. This is caused by the

worse suppression of the B-field for the detuned parameter set (compare section 14.3.1). In addition, a shortcoming in the measurement of the cross-coupling and Bloch-Siegert shifts caused an unintentional detuning. This results in first stage detuning errors of $\Delta_{1S} = 1.89(20)$ kHz and $\Delta_{1D} = 30(200)$ Hz for this measurement.

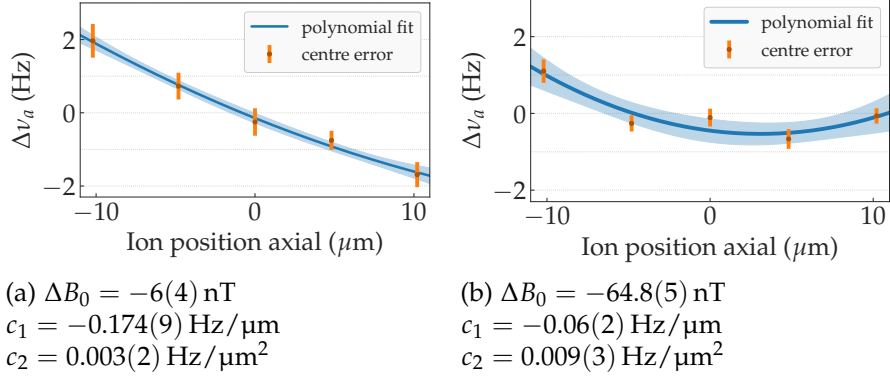


Figure 15.4: Frequency shift of the 2nd stage dynamical decoupling transition on a five ion crystal for two static B-field values with 2nd stage D-drive on magic angle (table D.1). The centres of the spectroscopic lines of the camera data are shown for the individual ions. The measured data is approximated by a polynomial function of the form $f(y) = c_0 + c_1x + c_2x^2$. (a) Target parameter set. (b) Same waveform, but detuned B-field, thus altered detunings Δ_i .

For optimization of the CDD parameter, the static B-field was detuned from its target value (fig. 15.4b). By altering the static offset field, the gradient of the B-field shift sensitivity is altered. There is a point, where the two inhomogeneous effects cancel each other out. Unfortunately, this also alters the resonance frequencies for all CDD transitions, thus all detunings Δ_i change and the magic angle condition is no longer perfectly fulfilled. Quantitatively, this optimization results in a $\frac{c_{1,a}}{c_{1,b}} = 27$ fold reduced linear dependency, but also a decreased QPS suppression, visible on the three-fold higher c_2 -factor.

Altering all the detunings via B_0 is suboptimal. With an optimization of all available control parameters, a flatter frequency dependence should be possible. Unfortunately, also the sensitivity to B-field fluctuations, thus the frequency shift over time, is determined by these detunings, so the goal of a stability improvement is not necessarily reached. This is confirmed by the following results.

15.3.1 Five ion stability

The stability of the five ion crystal with optimized parameter set is displayed in fig. 15.5. The 729 nm frequency deviation over time was taken with two-sample Rabi pulses with length $t_r = 100$ ms. A calibration scan was performed to deduce the signal slope $s = \frac{\partial(P_{e,\text{left}} - P_{e,\text{right}})}{\partial\nu}$ from the left $P_{e,\text{left}}$ and right $P_{e,\text{right}}$ slope of the transition. In addition to the data of the individual ions recorded with the camera, their average is shown.

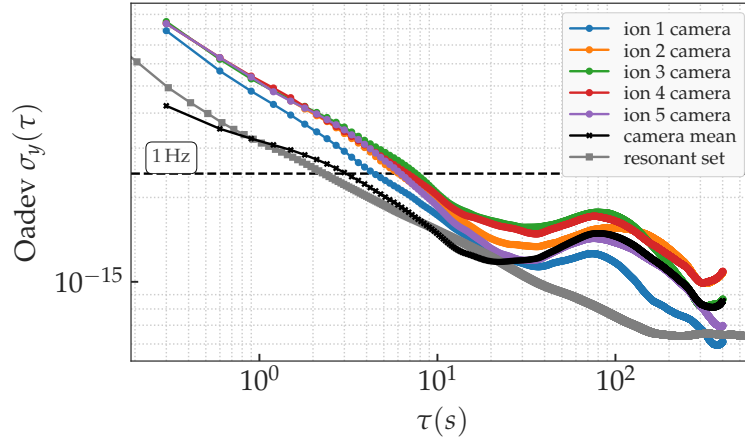


Figure 15.5: Overlapping Allan deviation of a five ion crystal with magic angle detuning. The same optimized parameter set as shown in fig. 15.4b is used. The stability data from the camera acquisition is displayed for each ion separately as well as their averaged signal (black). For comparison, the single ion stability (grey) with the on-resonance parameter set is shown (compare fig. 14.11).

For comparison, the single ion measurement with the *all resonant* parameter set (table D.1) is displayed (compare fig. 14.11). For short times, the averaged stability and the single ion measurement are comparable, the estimated scaling gain $\propto 1/\sqrt{N}$ for the higher ion number is compensated by the unfavourable interrogation with the two-sample Rabi instead of Ramsey technique. This was deliberately chosen for this measurement to avoid Ramsey fringe ambiguities for individual ions. In addition, the detection and cooling times are longer in the case of five ions. Therefore, the interrogation duty cycle decreased from $\frac{T}{T_c} = 59\%$ for the single ion measurement to $\frac{T}{T_c} = 33\%$ for multi-ion interrogation. With shorter camera exposure times and optimized cooling strategy, a higher duty-cycle is possible. At the averaging-time $\tau \approx 100$ s the five ion Allan deviation

has a peak. The reason for this is the lower B-field suppression due to the different used parameter set in combination with typical B-field deviations (compare fig. 14.6). Due to the field inhomogeneities, each ion experiences a slightly different drive strength and B-field offset. Therefore, the curves differ for the individual ions, despite their similar shape.

Part V

Outlook and Summary

Continuous dynamical decoupling improvements

The stability and homogeneity of the rf-drive constitute a major limitation of the used CDD-scheme (section 14.3.2). It has been shown that the suppression of the relevant frequency shifts is dependent on the coupling strength. Therefore, a priori lower perturbation of the magnetic field, especially of the fast mains supply contribution, would allow using decreased coupling strength, and thus a lower absolute shift caused by amplitude fluctuations. Therefore, an active magnetic field feed forward will be used in the future to cancel out the mains field and its harmonics [2]. The field homogeneity at the ions positions can be measured using the method demonstrated in section 15.2 and optimized with an additional coil.

It should also be possible to increase the stability of the driving fields by technical means. Heating of the critical coil components could be avoided by choosing another design for the radiating coil [118] to redirect power dissipation away from the sensitive electronic parts. A smaller distance of the radiating structure to the ion crystal would be beneficial to lower the power requirement and potentially avoid inhomogeneities with a smaller ratio of distance to coil diameter. This has to be implemented into a new trap design, as the smallest possible distance from outside the vacuum vessel is already implemented. The amplitude stability of the used rf-equipment, like AWG and amplifier, are not investigated individually, but it is expected that these contribute to the stability limit. An active envelope stabilization of their signal could decrease these contributions, but stabilization of the pulsed and modulated signal poses a technical challenge.

Usage of an alternative CDD-scheme is another option to avoid the high sensitivity to amplitude fluctuations in the first place. Implementing of a third drive with even lower amplitude is the consistent extension of the scheme [1]. The hierarchy of coupling has to be chosen analogously to the first two drives $\Omega_{1i} \gg \Omega_{2i} \gg \Omega_{3i} \gg \Omega_{729}$. Therefore, the energetic separation of the states would be $\Omega_{3i} \lesssim 1$ kHz and the spectrum will become quite dense. Also, the optical coupling strength to these

3rd-stage states would be reduced. This tightens the requirement on the spectral purity of the clock laser, but poses no fundamental limitation.

A different CDD-technique is used in [128] and [65]. Here, a Ramsey-like interrogation is used with several rf-pulses applied within its dark time to cancel the quadrupole shift using a tailored time-dependent Hamiltonian function. With correlation spectroscopy on a seven ion $^{88}\text{Sr}^+$ crystal, cancellation of the QPS to the level of $\Delta\nu_{\text{QPS}} \approx 10$ mHz was shown together with suppression of a static B-field gradient. However, that experiment was not sensitive to differential shifts between S and D states.

Yet another approach is used to avoid inhomogeneous motional dephasing in collective states [36]. In contrast to other continuous dynamical decoupling approaches, it uses two dressing fields with opposite detunings to cancel the drive shift to first order. The applicability of such a scheme to the $^{40}\text{Ca}^+$ system has to be investigated.

New experimental control system

Some shortcomings of the described experimental setup are caused by the experimental hard- and software. Therefore, a new framework¹ was implemented in the last months. The benefits of the new system include:

- Finer frequency resolution of the used DDS-chips.
- Data acquisition within the sequence to avoid delay times.
- Extended communication capabilities with non-core devices.
- Direct FPGA controlled parameter variation for e.g. faster controlled frequency steering to an atomic resonance.
- Extended possibilities for automation of calibration experiments.
- Inclusion of many data sources like WM, counters etc. to detect malicious events within the framework.
- Tighter collaboration with other experiments to enhance development of the software.
- Future-proof hardware maintainability.

With this, the capabilities of the old system are superseded by the new experimental control hard- and software. The control system is continuously tested and extended in the presented setup at the moment [25].

¹ ARTIQ-Software combined with Sinara Hardware family, M-Labs [82]

Compound clock

The artificial clock transition formed with CDD is not as accurate as other atomic clock candidates. There are two reasons for this. First, the theoretical investigation of this system has just started recently, therefore additional line shifts might be included in the future. A not included effect is e.g. the 2nd order Zeeman effect. Simulation of the full dynamics of the system is highly resource intensive. Therefore, some approximations have to be made to treat the system analytically and account for corrections afterwards. However, the larger uncertainty at the moment is the dependency of the artificial transition frequency on the applied static and rf B-fields. They need to be calibrated on the ion crystal in situ. For slow fluctuations of the drive amplitude, it would be possible to stabilize the clock laser to a virtual transition. This transition should be independent of the drive strength by averaging over different states with opposing dressed state quantum numbers $m_{1S}, m_{1D}, m_{2S}, m_{2D}$ analogously to averaging over Zeeman levels in other experiments. With this, the coupling strength can be monitored and corrected without compromising the long probe time per interrogation.

As stated in the introduction, absolute accuracy is not the main requirement for the anticipated application. It is designed for low statistical uncertainty, which would be beneficial in a compound clock as well as in applications where only relative frequency differences are needed. In a compound clock, a system with low statistical uncertainty is used to track the laser phase noise coarsely. This information is then used to extend the interrogation time for the synchronously probed accurate clock beyond the coherence time of the local oscillator. Thus, relative phase excursions $|\Phi| > \pi/2$ between uncorrected laser and atomic oscillator do not pose a strict limitation any more. The ambiguous fringe assignment in such a Ramsey experiment can be lifted with help of the coarse phase information. Therefore, the compound clock can achieve higher frequency stability due to the laser-coherence-time exceeding interrogation time. An interrogation scheme using multiple $\pi - \epsilon$ -pulses within the dark time to partially decouple laser phase noise in a controlled

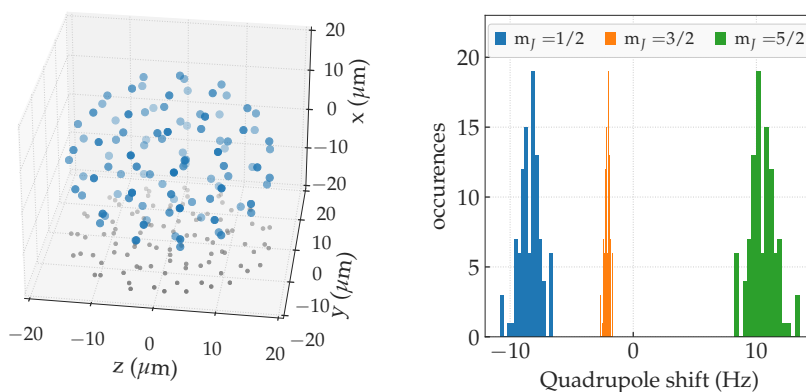
fashion is shown in [26]. This scheme is suitable to imprint coarse phase information into the state of one clock during the long interrogation time of the other clock.

Under optimal conditions with increased duty cycle, the QPN limited decoupled $^{40}\text{Ca}^+$ system would require $N \lesssim 10$ ions to compete with the stability of the Si-cavity reference laser at an averaging time of 20 s. For a more detailed discussion, the noise processes of the LO must be analyzed together with the interrogation strategy for both clocks [58, 78]. In general, the stability gain for a compound system in comparison to a single ion clock is larger for a given pre-stabilization with higher noise contributions [1].

In an envisioned setup, an $^{27}\text{Al}^+ / ^{40}\text{Ca}^+$ crystal and a large spherical $^{40}\text{Ca}^+$ crystal are trapped within different potential wells of the same segmented Paul trap. They form a compound clock whose performance limit is less affected by LO stability. Especially for applications like transportable clocks for geodetic measurements with restricted footprint and disturbing environmental influences, such a system would be advantageous. This work is meant to be a building block towards such a system.

Spherical ion crystal

For improved statistical uncertainty, the ion number N should be increased in the future. Above a few tens of stored ions, it is desirable to use a 3D ion crystal configuration as proposed in [1]. There are several reasons for this. With a maximal radial trapping frequency given by the trap limitations, the axial trapping potential has to be lowered in order to store longer linear ion strings. First, the large axial extension of the crystal will increase the influence of inhomogeneous fields like the static- and rf B-field. In addition, cooling of larger ion strings will become less efficient. The higher Lamb-Dicke parameter increases the minimum achievable temperature for Doppler-cooling as well as EIT- and SBC-cooling. In combination with larger heating rates for lower secular frequencies[66], a much higher phonon number is expected. The relative influence of stray fields is also larger at lower dc-voltages.

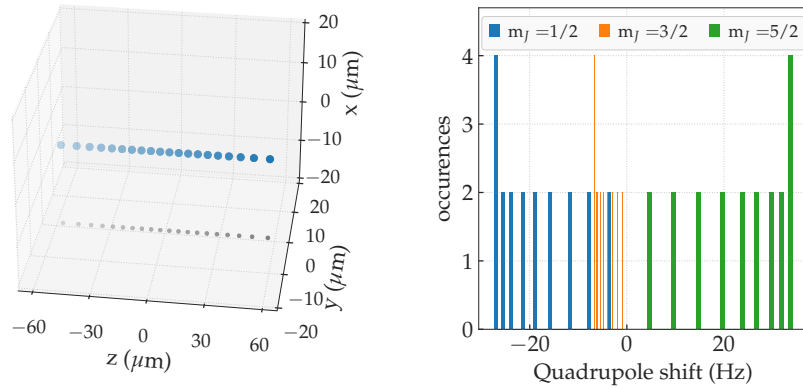


(a) Simulation of equilibrium positions of a 100 ion $^{40}\text{Ca}^+$ crystal in spherical configuration with $\omega_{x,y,z} = 2\pi \times 1$ MHz. Grey dots indicate the projection in one direction.

(b) Histogram of quadrupole shifts for the 100 ions crystal. The distribution width of electric field gradient is small for a spherical crystal. Thus, the QPS is comparable for the individual ions.

Figure 19.1: Simulations of spherical multi-ion crystals.

As shown in section 11.3.2, the negative static electric-dipole polarizability enables a cancellation of uncompensated EMM



(a) Simulation of equilibrium positions of a linear 20 ion $^{40}\text{Ca}^+$ crystal with $\omega_{x,y,z} = 2\pi \times (2.0, 2.0, 0.2)$ MHz close to the 2D phase transition. (b) Histogram of quadrupole shifts for the linear 20 ions crystal. The QPS varies largely for the individual ions.

Figure 19.2: Simulations of linear multi-ion crystals.

and ac-Stark shift for the magic drive frequency. This is of special importance for 3D configurations with unavoidable radial EMM contribution. The validity of 2nd order Doppler shift and ac-Stark shift cancellation must be investigated carefully, especially with respect to higher order corrections [4]. In addition, the ion movement will be strongly driven in radial direction with the trap drive frequency. Therefore, only axial clock laser interrogation seems feasible to avoid dramatic contrast loss due to this modulation. The trap drive-induced factor within the time-dilation shift (compare eq. (11.1)) is not cancelled by the magic frequency, so low motional mode excitation is needed to reduce this shift.

As these configurations have a relatively small spatial expansion even for large ion numbers (fig. 19.1a and fig. 19.2a), effects of field inhomogeneities are reduced. In addition, the electric field gradient distribution is relative narrow across the crystal, thus QPS and TASS are more homogeneous compared to a linear crystal (fig. 19.1b and fig. 19.2b). Nevertheless, increasing the ion number poses new challenges. More frequent background gas collisions in combination with additional heating processes from e.g. higher order trapping potential contributions disturb the crystallization process [27]. The energetic gap between slightly different crystal configuration becomes smaller for larger crystals, resulting in frequent configuration changes.

The perturbation of longer spectroscopy pulses by this effect must be investigated.

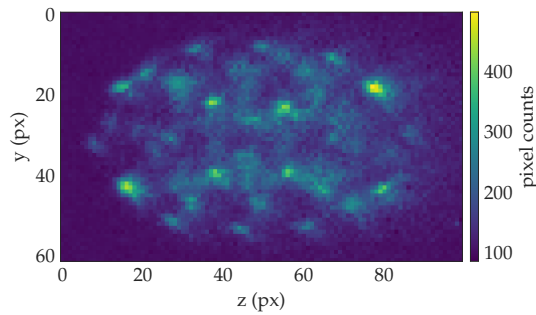


Figure 19.3: Camera picture of a near-spherical 52 ion crystal taken with long exposure time. The field of depth of the used imaging system is too small to resolve all individual ions.

As seen in fig. 19.3, individual ions of spherical crystals are overlapping and are not resolved with the current imaging optics, so the joint fluorescence of the crystal on the PMT must be employed to detect their joint excitation probability.

Summary

Modern single ion optical atomic clocks reach excellent frequency accuracies. But their statistical uncertainty cannot compete with optical clocks based on trapped neutral atoms. More stable local oscillators would elongate the usable probe time, thus improve their statistical uncertainty. However, technical challenges will slow their progress in the future. Scaling up the number of ions stored in a Paul trap will hamper the superb accuracy of single ion clocks due to the strong trapping field. The dynamical decoupling scheme investigated within this work has the potential to mitigate some of these shifts to allow multi-ion operation.

The main achievement in this work is the creation of an optical transition with high robustness to the perturbations present in an ion trap experiment. However, the absolute frequency accuracy of the transitions cannot yet get traced back with high accuracy to the bare $^{40}\text{Ca}^+$ transition, as a large artificial line shift is applied. The major frequency shifts of the single ion $^{40}\text{Ca}^+$ clock transition were characterized and the prospect for multi-ion operation is given. The negative static electric-dipole polarizability in calcium enables cancellation of trap drive induced shifts, which is especially beneficial for spherical crystals. Fast ground state cooling of a single ion was shown and the prospect for the transferability of EIT-cooling to larger ion crystals was indicated. The secular motion-induced 2nd order Doppler shift would require sub-Doppler temperatures to reach a level of 10^{-18} even for linear multi-ion crystals. Therefore, methods for cooling of all motional modes must be investigated in the future.

The artificial clock transition of the coupled system formed by CDD suppresses the linear Zeeman shift to a high degree. With the CDD-drive strengths used in this work, a magnetic-field sensitivity of $-1.2(1) \times 10^{-4} \text{ Hz/nT}^2$ was achieved, which is comparable to the 2nd order Zeeman shift of field insensitive clock species. With this, a long coherence time on the order of the natural lifetime limit in $^{40}\text{Ca}^+$ could be realized without the need for magnetic shielding. This allowed the resolution of the artificial transition with a probe time-limited linewidth of $\Delta\nu =$

2.2(4) Hz, which is to my knowledge the narrowest transition measured on a $^{40}\text{Ca}^+$ system so far¹. Here, the measurement benefits from the high stability of the clock laser's stabilization to the Si-cavity.

The presented scheme is also capable of suppressing the inhomogeneous tensorial QPS and TASS on ion crystals. A 12-fold suppression of the QPS was shown for a linear five ion crystal. A conflict between higher suppression of magnetic-field noise by stronger rf-magnetic fields and their induced line shift poses a limitation. The technical limitations from this were investigated in detail and potential improvements were pointed out. Further reduction seems feasible with minor technical improvements.

A statistical uncertainty of $4 \times 10^{-15} / \sqrt{\tau}$ was reached for short interrogation times. For longer times the uncertainty is limited by the residual shifts on the artificial transition. For multi-ion crystals the residual B-field noise poses a limitation, as its magnetic field sensitivity suppression is lower for a CDD-scheme, optimized for simultaneous suppression of tensorial shifts. A higher duty cycle would be attained with an optimized sequence with less frequent state interrogation, shorter read-out times and an optimized adiabatic state initialization.

This work is a step forward on the way towards a compound ion clock with improved statistical uncertainty. The engineering needed for constructing an ultra-stable cavity is reduced for such a system. In addition, continuous dynamical decoupling can be seamlessly integrated in most Paul trap experiments without the need for involved changes in the setup. The method is applicable to atomic species with similar level structure. Hence, other academic research groups may benefit from this new method in the quantum state manipulation toolbox.

¹ Other experiments have performed measurements with lower uncertainties with averaging over Zeeman sub-levels. But here, the single interrogation limit is meant.

Part VI

Appendix

Ion crystal shape

The potential energy of N ions with charge $q = Ze$ and mass m in a harmonic pseudo-potential with secular trapping frequencies ω_i can be written as extension of eq. (10.3) [62]

$$V = \sum_{i=x,y,z}^3 \sum_{m=1}^N \frac{1}{2} m \omega_i^2 r_{m,i}^2 + \sum_{\substack{m,n=1 \\ m \neq n}}^N \frac{q^2}{8\pi\epsilon_0} \left[\sum_{i=x,y,z}^3 (r_{n,i} - r_{m,i})^2 \right]^{-\frac{1}{2}}, \quad (\text{A.1})$$

with position vector component $r_{n,i}$ of the n^{th} ion. The equilibrium positions are attained by minimizing the potential with respect to the positions of all ions and directions

$$\left[\frac{\partial V}{\partial \mathbf{r}_m} \right]_{\mathbf{r}_m = \mathbf{r}_m^{(0)}} = 0. \quad (\text{A.2})$$

For higher ion numbers, the equilibrium positions are found numerically¹.

The displacements from the equilibrium positions $u_{n,i}(t) = r_{n,i} - r_{n,i}^0(t)$ and velocities $\dot{u}_{n,i}$ of the ions are coupled by the Coulomb interaction. For sufficient cold ions the displacements are small, so higher order effects can be neglected. The Lagrangian of motion is described by [33]

$$\begin{aligned} L &= \frac{m}{2} \sum_{i=x,y,z}^3 \left(\sum_{m=1}^N (\dot{q}_{m,i})^2 - \frac{1}{m} \sum_{n,m=1}^N q_{n,i} q_{m,i} \left[\frac{\partial^2 V}{\partial x_{n,i} \partial x_{m,i}} \right]_{q_n=q_m=0} \right) \\ &= \frac{m}{2} \left(\sum_{m=1}^N (\dot{q}_{m,z})^2 - \omega_z^2 \sum_{n,m=1}^N A_{n,m} q_{n,z} q_{m,z} \right) \\ &\quad + \frac{m}{2} \left(\sum_{m=1}^N (\dot{q}_{m,x})^2 - \omega_x^2 \sum_{n,m=1}^N B_{n,m} q_{n,x} q_{m,x} \right) \\ &\quad + \frac{m}{2} \left(\sum_{m=1}^N (\dot{q}_{m,y})^2 - \omega_y^2 \sum_{n,m=1}^N B_{n,m} q_{n,y} q_{m,y} \right), \end{aligned}$$

¹ using the Python function `scipy.optimize.basinhopping`

with

$$A_{nm} = \begin{cases} 1 + \frac{2q^2}{4\pi\epsilon_0 m \omega_z^2} \sum_{p=1, p \neq m}^N \frac{1}{|r_m^0 - r_p^0|^3} & \text{for } n = m \\ \frac{-2q^2}{4\pi\epsilon_0 m \omega_z^2} \frac{1}{|r_m^0 - r_p^0|^3} & \text{for } n \neq m \end{cases}$$

$$B_{n,m} = \left(\frac{1}{\alpha_i} + \frac{1}{2} \right) \delta_{n,m} - \frac{1}{2} A_{n,m}$$

, with anisotropy parameter $\alpha_{x(y)} = (\omega_z / \omega_{x(y)})^2$ and Kronecker delta $\delta_{n,m}$.

The eigenvectors and eigenvalues of the matrix $A_{n,m}$ ($B_{n,m}$) define the normal modes of the crystal in axial (radial) direction, by

$$\sum_{m=1}^N A_{n,m} b_m^p = \mu_p b_n^p$$

$$\sum_{m=1}^N B_{n,m} b_m^p = \left(\frac{1}{\alpha} + \frac{1}{2} - \frac{\mu_p}{2} \right) b_n^p,$$

with the normalized eigenvectors b_n^p of the n^{th} ion and p^{th} mode. The mode frequencies are given by $\omega_{i,p} = \sqrt{\mu_p} \omega_i$. With descending ratio of axial to radial confinement, the critical anisotropy parameter $\alpha_{\text{crit}} = 2 / (\mu_{\text{max}} - 1)$ is reached. Beyond this, the highest radial mode gets unstable (the eigenvalues become negative) and a transition from linear to 2D crystal occurs.

Laser angle determination

Geometric measurements of the laser incidence angles with respect to the principal axis of the trap are error-prone. But by measuring the ratio of carrier and blue sideband for a ground state cooled ion, the exact alignment of the used laser beam can be determined. Using eq. (10.5) and the coupling strengths of the transitions yield

$$\phi_i = \cos^{-1} \left(|k| \frac{\Omega_{\text{BSB},i}}{\Omega_{\text{car}}} \sqrt{\frac{2m\omega_i}{\hbar}} \right). \quad (\text{B.1})$$

With this technique, the measured angles of the diagonal beam to the mode directions are $\phi_x = 67.1(2)^\circ$, $\phi_y = 47.5(4)^\circ$ and $\phi_z = 48.4(3)^\circ$ with a typical set of trap voltages. The absolute value of the directional normal vector based on these angles show a 2% deviation from unity. This may be caused by altered laser intensity by different AOM frequencies for the vibrational modes.

Waveforms for continuous dynamical decoupling

First sweep

$$y(t) = \frac{1}{2} e^{-\frac{(t-T)^2}{\sigma^2}} \Omega_1 \sin \left(2\pi \left[f_{1,\text{init}} t + \frac{(f_1 - f_{1,\text{init}})}{2T} t^2 \right] \right) \quad (\text{C.1})$$

First stage

$$y(t) = \frac{1}{2} \Omega_1 \sin(2\pi t f_1 + \phi_{\text{fast}}) \quad (\text{C.2})$$

Second sweep

$$y(t) = \frac{1}{2} \Omega_1 \sin(2\pi t f_1 + \phi_{\text{fast}}) + \frac{1}{2} e^{-\frac{(t-T)^2}{\sigma^2}} \Omega_2 \sin(2\pi t f_1 + \frac{\pi}{2} + \phi_{\text{fast}}) \times \sin \left(2\pi \left[f_{2,\text{init}} t + \frac{f_2 - f_{2,\text{init}}}{2T} t^2 \right] + \phi_{\text{slow}} \right) \quad (\text{C.3})$$

Second stage

$$y(t) = \frac{1}{2} \Omega_1 \sin(2\pi t f_1 + \phi_{\text{fast}}) + \frac{1}{2} \Omega_2 \sin(2\pi t f_1 + \frac{\pi}{2} + \phi_{\text{fast}}) \times \sin(2\pi f_2 t + \phi_{\text{slow}}) \quad (\text{C.4})$$

In order to ensure a smooth transition from one waveform to the next, the phases ϕ_{slow} and ϕ_{fast} are adapted.

Continuous dynamical decoupling parameter sets

	Full coupling resonant	Half coupling resonant	Half coupling magic angle
f_{S1}	10007947	10002089	10002089
f_{D1}	5994613	5994834	5994834
Ω_{S1}	93546	46862	46862
Ω_{D1}	225332	115446	115446
Ω_{S2}	14774	3469	3469
Ω_{D2}	13589	6809	6809
f_{S2}	93652	46915	46951
f_{D2}	135236	69287	70731
Δf_{sw1}	-1500000	-150000	-1500000
t_{sw}	500	500	500
Δf_{sw2}	80000	80000	30000
t_{sw2}	7000	7000	7000
used in	fig. 14.4, fig. 14.10 fig. 14.11, fig. 14.12 fig. 14.12, fig. 15.3	fig. 14.4	fig. 14.4, fig. 15.4 fig. 15.5

Table D.1: Parameter sets for CDD waveforms. All units of frequencies and coupling strength are Hz, all units for times are μs . For facilitating the assignment, the used parameter sets are named and references to the performed measurements are given.

Optical coupling of first stage artificial transition

m_{0S}	m_{0D}	m_{1S}	m_{1D}	$\Delta\nu_{\text{calc}}$ (MHz)	$\Delta\nu$ (MHz)	$\Omega_M/\Omega_{m_{0S},m_{0D}}$ calculated	Ω_M (kHz)
-1/2	-5/2	1/2	-5/2	-10.18386	-10.18395	0.12331	0.23861
-1/2	-5/2	-1/2	-5/2	-10.13697	-10.13702	0.12845	0.22617
-1/2	-5/2	1/2	-3/2	-10.11448	-10.11448	0.27493	0.52114
-1/2	-5/2	-1/2	-3/2	-10.06759	-10.06771	0.28640	0.52519
-1/2	-5/2	1/2	-1/2	-10.04510	-10.04488	0.38769	0.81061
-1/2	-5/2	-1/2	-1/2	-9.99821	-9.99805	0.40385	0.77476
-1/2	-5/2	1/2	1/2	-9.97572	-9.97573	0.38657	0.78431
-1/2	-5/2	-1/2	1/2	-9.92883	-9.92877	0.40269	0.77869
-1/2	-5/2	1/2	3/2	-9.90634	-9.90644	0.27255	0.54841
-1/2	-5/2	-1/2	3/2	-9.85945	-9.85939	0.28392	0.55880
-1/2	-5/2	1/2	5/2	-9.83696	-9.83703	0.12154	0.24665
-1/2	-5/2	-1/2	5/2	-9.79007	-9.79012	0.12661	0.24661
-1/2	-3/2	1/2	-5/2	-4.18903	-4.18906	0.27493	0.46923
-1/2	-3/2	-1/2	-5/2	-4.14213	-4.14214	0.28640	0.45828
-1/2	-3/2	1/2	-3/2	-4.11965	-4.11970	0.36708	0.62568
-1/2	-3/2	-1/2	-3/2	-4.07275	-4.07281	0.38239	0.62326
-1/2	-3/2	1/2	-1/2	-4.05027	-4.05028	0.17087	0.29412
-1/2	-3/2	-1/2	-1/2	-4.00337	-4.00337	0.17799	0.29951
-1/2	-3/2	1/2	1/2	-3.98089	-3.98091	0.17538	0.27588
-1/2	-3/2	-1/2	1/2	-3.93399	-3.93401	0.18270	0.26195
-1/2	-3/2	1/2	3/2	-3.91151	-3.91156	0.36743	0.61065
-1/2	-3/2	-1/2	3/2	-3.86461	-3.86458	0.38276	0.61313
-1/2	-3/2	1/2	5/2	-3.84213	-3.84216	0.27255	0.45904
-1/2	-3/2	-1/2	5/2	-3.79523	-3.79526	0.28392	0.45519

Table E.1: Measured and calculated optical coupling strengths and the frequency offsets from the field-free ${}^2S_{1/2} \leftrightarrow {}^2D_{5/2}$ for the 1st stage near-resonant CDD-transition. This data is used for fig. 14.3.

E.1 Analytic function for deriving CDD transitions

```

1 import pandas as pd
2 import numpy as np
3 from math import factorial
4
5 def weight(j, angle, mj, m):
6     """
7     Function to calculate the relative optical coupling due to the rotation around
8     ↪ Jy
9     adapted version base on idea of Victor Martinez
10    :param j: (float); the total angular momentum

```

```

10 :param angle: (float) angle of rotation
11 :param mj: (int) bare Zeeman magnetic quantum number
12 :param m: (int); m quantum number dressed basis
13 :return: (float) the relative weight for the coupling
14 """
15 factor = np.sqrt(factorial(j + m) * factorial(j - m) * factorial(j + mj) *
16                 ↪ factorial(j - mj))
17 kvalues = np.arange(max(mj - m, 0), min(j + mj, j - m) + 1)
18 x = 0
19 for k in kvalues:
20     x += pow(-1, k - mj + m) * pow(np.cos(angle / 2), 2 * j - 2 * k + mj - m)
21         ↪ * \
22         pow(np.sin(angle / 2), 2 * k - mj + m) / \
23         (factorial(j + mj - k) * factorial(k) * factorial(j - k - m) *
24         ↪ factorial(k - mj + m))
25 return x * factor
26
27 def DD_1_lines(carrier_ax, B_splitting, S0_f_cc, D0_f_cc, S1_Omega, D1_Omega,
28             ↪ S1_Delta, D1_Delta,
29             mjs_list=[-1/2, 1/2], mjd_list=[-5/2, -3/2, -1/2, 1/2, 3/2, 5/2],
30             ms_list=[-1/2, 1/2], md_list=[-5/2, -3/2, -1/2, 1/2, 3/2, 5/2], **
31             ↪ kwargs):
32     """
33     calculates frequencies of first stage CDD states for given parameters
34     param: carrier_ax (float) AOM frequency of S-0.5 ↔ D-3/2 transition
35     param: B_splitting (float) ground state splitting (MHz)
36     param: S0_f_cc, D0_f_cc: (float) first stage resonant frequencies (Hz) =
37         ↪ Zeeman splitting + correction if any
38     param: S1_Omega, D1_Omega: (float) first stage coupling strength = splitting
39         ↪ of states (Hz)
40     param: S1_Delta, D1_Delta: (float) detuning of actual drive from resonant
41         ↪ frequencies
42     param: mjs_list, mjd_list: (list) Zeeman quantum number lists
43     param: ms_list, md_list: (list) CDD state quantum number lists
44     returns: pandas.DataFrame with transitions, labels... frequencies in (MHz)
45     """
46
47     # generalised rabi frequencies
48     S1_Omega_bar = np.sqrt(S1_Delta ** 2 + (S1_Omega * gs / 2) ** 2)
49     D1_Omega_bar = np.sqrt(D1_Delta ** 2 + (D1_Omega * gd / 2) ** 2)
50     thetarotate_s = np.arccos(-S1_Delta / S1_Omega_bar)
51     thetarotate_d = np.arccos(-D1_Delta / D1_Omega_bar)
52     temp = []
53     # calculate center frequencies from given -0.5 ↔ -3/2 carrier frequency
54     center_freq = carrier_ax + 0.5 * (-0.5 * B_splitting + 3/2 * gd/gs *
55         ↪ B_splitting)
56     # print(f'center_freq {center_freq}')
57     for mjs in mjs_list:
58         for mjd in mjd_list:
59             if abs(mjd - mjs) < 3:
60                 for ms in ms_list:
61                     for md in md_list:
62                         frequency = (center_freq + 1 / 2 * (S1_Omega_bar * ms +
63                             ↪ D1_Omega_bar * md - (S0_f_cc + S1_Delta) * mjs +
64                             ↪ D0_f_cc + D1_Delta) * mjd) / 1e6
65
66                         rel_coupling = abs(weightd(j=1 / 2, angle=thetarotate_s,
67                             ↪ mj=mjs, m=ms) * weightd(j=5 / 2, angle=
68                             ↪ thetarotate_d, mj=mjd, m=md))
69
70                         temp.append({'mjs': mjs, 'mjd': mjd, 'ms': ms, 'md': md, '
71                             ↪ label': f'{int(2 * mjs)}/2{int(2 * mjd)}/2{int(2
72                             ↪ * ms)}/2{int(2 * md)}/2', 'freq_cal': frequency,
73                             ↪ 'rel_coupling': rel_coupling})
74
75     df = pd.DataFrame(temp)

```

```

60 df.sort_values(axis=0, by='freq_cal', inplace=True)
61 df1 = df.reset_index(drop=True)
62 return df1
63
64 def DD_2_lines(DD_1_lines, S2_Omega, D2_Omega, S2_Delta, D2_Delta, ms2_list=[-0.5,
65     ↪ 0.5], md2_list=[-5/2,-3/2, -1/2, 1/2, 3/2, 5/2], **kwargs):
66     """
67     calculates frequencies of second stage CDD states for given parameters
68     param: DD_1_lines (pd.DataFrame) first stage frequencies df (output of DD_1_lines
69     ↪ ), if None, calc only one ensemble around 0
70     param: S2_Omega, D2_Omega: (float) second stage experimental coupling strength =
71     ↪ splitting of states (Hz)
72     param: S2_Delta, D2_Delta: (float) detuning of actual drive from resonant
73     ↪ frequencies
74     param: ms2_list, md2_list: (list) CDD state quantum number lists
75     returns: pandas.DataFrame with transitions, labels... frequencies in (MHz)
76     """
77     if (DD_1_lines is None):
78         DD_1_lines = pd.DataFrame({'mjs':[0], 'ms':[0], 'mjd':[0], 'md':[0], 'freq_cal'
79         ↪ : [0]})
80
81     S2_Omega_bar = np.sqrt(S2_Delta**2 + (S2_Omega*gs/4)**2)
82     D2_Omega_bar = np.sqrt(D2_Delta**2 + (D2_Omega*gd/4)**2)
83     temp = []
84     for index, row in DD_1_lines.iterrows():
85         for ms2 in ms2_list:
86             for md2 in md2_list:
87                 frequency = row['freq_cal'] + 0.5 * (- S2_Omega_bar * ms2 + D2_Omega_bar * md2
88                 ↪ + S2_Delta * row.ms - D2_Delta * row.md)/1e6
89                 temp.append({'mjs': row.mjs, 'mjd': row.mjd, 'ms': row.ms, 'md': row.md, 'ms2'
90                 ↪ : ms2, 'md2': md2,
91                 ↪ 'label': f'{int(2 * row.mjs)}/2|{int(2 * row.mjd)}/2|'
92                 ↪ f'{int(2 * row.ms)}/2|{int(2 * row.md)}/2|'
93                 ↪ f'{int(2 * ms2)}/2|{int(2 * md2)}/2', 'freq_cal': frequency})
94     df = pd.DataFrame(temp)
95     df.sort_values(axis=0, by='freq_cal', inplace=True)
96     df1 = df.reset_index(drop=True)
97     return df1

```


Error signal corrections by optical coupling variations

A modification of the artificial transition to normal atomic transitions is the change in optical coupling strength with altered static magnetic field (compare section 14.2). Although most clock interrogation sequences are immune to Rabi frequency fluctuations to some degree, it still can affect stability measurements. Magnetic field changes cause a variation of the frequency deviation slope by the altered optical coupling strength. Although this effect is quite small in most cases, it is important to investigate and correct such unusual effects for the artificial transition.

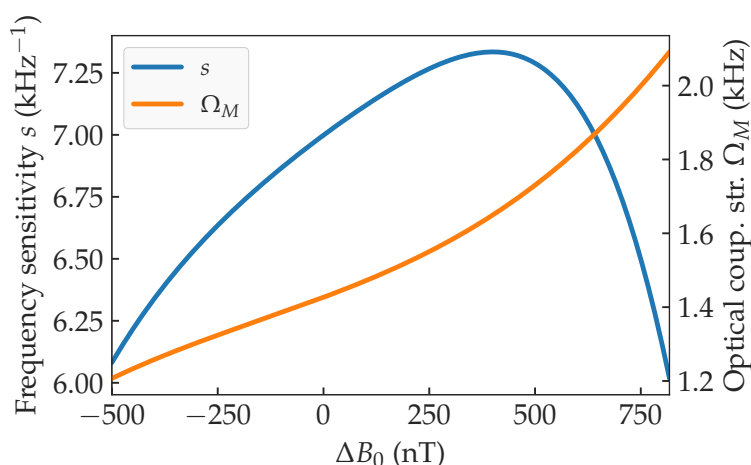


Figure F.1: Dependency of side-of-fringe measurements on the artificial transition from static B-field changes. The frequency sensitivity (blue, left) and optical coupling strength (orange, right) are displayed in dependence of magnet field shifts. The coupling strength data was approximated with a polynomial function. The frequency sensitivity slope $s = \frac{\partial(P_{e,\text{left}} - P_{e,\text{right}})}{\partial\nu}$ was derived from simulating sinc² functions with changing pulse areas due to the altered optical coupling strength. The maximal sensitivity at $\Delta B \neq 0$ reveals the non-optimal pulse area for this measurement.

In the following, the influence of this effect on a two-sample side-of-fringe Rabi experiment is shown as an example. The variation of optical coupling strength was measured for different magnetic fields and approximated by a polynomial function.

With this, the magnetic field-dependent frequency sensitivity $s = \frac{\partial(P_{e,\text{left}} - P_{e,\text{right}})}{\partial\nu}$ could be derived for a fixed interrogation time (see fig. F.1). Here, $P_{e,\text{left}}$ and $P_{e,\text{right}}$ are the excitation probabilities of the pulses on the left and right flank. In order to correct a measurement accordingly, the altered frequency discriminant has to be accounted for. In fig. F.2, this is shown for a wide scan of the static offset field ΔB_0 .

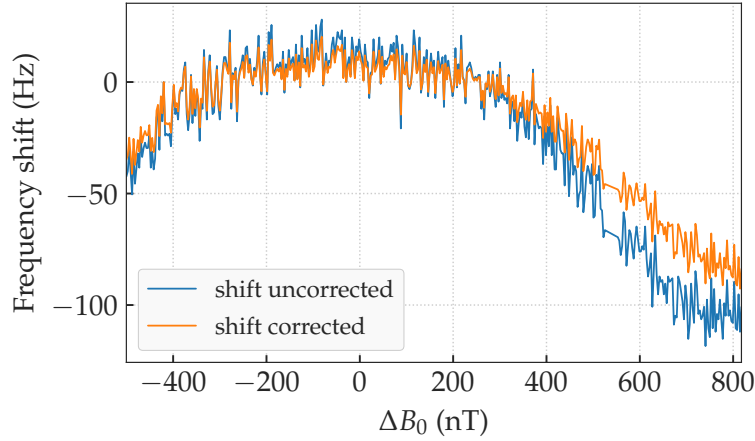


Figure F.2: Frequency shift of the doubly dressed transition with respect to an offset magnetic field ΔB_0 from the point of zero frequency gradient. Frequency deviations over time were taken with a two sample Rabi pulse with length $t_r = 2$ ms. For the corrected data (orange), the frequency sensitivity $s = \frac{\partial(P_{e,\text{left}} - P_{e,\text{right}})}{\partial\nu}$ was adapted according to fig. F.1.

Bibliography

Bibliography

- [1] N. Aharon, N. Spethmann, I. D. Leroux, P. O. Schmidt, and A. Retzker. “Robust Optical Clock Transitions in Trapped Ions Using Dynamical Decoupling”. In: *New Journal of Physics* 21.8 (2019), p. 083040. DOI: 10.1088/1367-2630/ab3871 (cit. on pp. 87, 89, 95, 98, 117, 133, 138, 139).
- [2] L. Anders. “Entwicklung einer Magnetfeldstabilisierung für den gezielten Ausgleich periodischer, sinusförmiger Störfelder mit einem FPGA- basierten Entwicklungsboard”. de. Bachelor Thesis. Ostfalia Hochschule für angewandte Wissenschaften, 2020 (cit. on p. 133).
- [3] E. R. Andrew, A. Bradbury, and R. G. Eades. “Nuclear Magnetic Resonance Spectra from a Crystal Rotated at High Speed”. In: *Nature* 182.4650 (1958), pp. 1659–1659. DOI: 10.1038/1821659a0 (cit. on pp. 93, 94).
- [4] K. Arnold, E. Hajiyev, E. Paez, C. H. Lee, M. D. Barrett, and J. Bollinger. “Prospects for Atomic Clocks Based on Large Ion Crystals”. In: *Physical Review A* 92.3 (2015), p. 032108. DOI: 10.1103/PhysRevA.92.032108 (cit. on pp. 11, 140).
- [5] P. A. Barton, C. J. S. Donald, D. M. Lucas, D. A. Stevens, A. M. Steane, and D. N. Stacey. “Measurement of the lifetime of the $3d^2D_{5/2}$ state in $^{40}\text{Ca}^+$ ”. In: *Physical Review A* 62.3 (2000), p. 032503. DOI: 10.1103/PhysRevA.62.032503 (cit. on p. 33).
- [6] K. Beeks, T. Sikorsky, T. Schumm, J. Thielking, M. V. Okhapkin, and E. Peik. “The Thorium-229 Low-Energy Isomer and the Nuclear Clock”. In: *Nature Reviews Physics* 3.4 (2021), pp. 238–248. DOI: 10.1038/s42254-021-00286-6 (cit. on p. 7).

- [7] N. Beev, J.-A. Fenske, S. Hannig, and P. O. Schmidt. “A Low-Drift, Low-Noise, Multichannel Dc Voltage Source for Segmented-Electrode Paul Traps”. In: *Review of Scientific Instruments* 88.5 (2017), p. 054704. DOI: 10.1063/1.4983925 (cit. on p. 16).
- [8] E. Benkler, B. Lipphardt, T. Puppe, R. Wilk, F. Rohde, and U. Sterr. “End-to-end topology for fiber comb based optical frequency transfer at the 10^{-21} level”. In: *Optics Express* 27.25 (2019), p. 36886. DOI: 10.1364/OE.27.036886 (cit. on pp. 46, 47).
- [9] D. J. Berkeland, J. D. Miller, J. C. Bergquist, W. M. Itano, and D. J. Wineland. “Minimization of Ion Micromotion in a Paul Trap”. In: *Journal of Applied Physics* 83.10 (1998), pp. 5025–5033. DOI: 10.1063/1.367318 (cit. on pp. 61, 62, 86).
- [10] E. D. Black. “An Introduction to Pound–Drever–Hall Laser Frequency Stabilization”. In: *American Journal of Physics* 69.1 (2000), pp. 79–87. DOI: 10.1119/1.1286663 (cit. on p. 39).
- [11] R. Blatt, H. Häffner, C. F. Roos, C. Becher, and F. Schmidt-Kaler. “Ion Trap Quantum Computing with Ca^+ Ions”. In: *Quantum Information Processing* 3.1 (2004), pp. 61–73. DOI: 10.1007/s11128-004-3105-1 (cit. on p. 33).
- [12] F. Bloch and A. Siegert. “Magnetic Resonance for Nonrotating Fields”. In: *Physical Review* 57.6 (1940), pp. 522–527. DOI: 10.1103/PhysRev.57.522 (cit. on p. 98).
- [13] I. Bloch. “Ultracold Quantum Gases in Optical Lattices”. In: *Nature Physics* 1.1 (2005), pp. 23–30. DOI: 10.1038/nphys138 (cit. on p. 5).
- [14] T. Bothwell, D. Kedar, E. Oelker, J. M. Robinson, S. L. Bromley, W. L. Tew, J. Ye, and C. J. Kennedy. “JILA SrI optical lattice clock with uncertainty of 2.0×10^{-18} ”. In: *Metrologia* 56.6 (2019), p. 065004. DOI: 10.1088/1681-7575/ab4089 (cit. on p. 7).
- [15] S. M. Brewer, J.-S. Chen, A. M. Hankin, E. R. Clements, C. W. Chou, D. J. Wineland, D. B. Hume, and D. R. Leibbrandt. “ $^{27}\text{Al}^+$ Quantum-Logic Clock with a Systematic Uncertainty below 10^{-18} ”. In: *Physical Review Letters* 123.3 (2019), p. 033201. DOI: 10.1103/PhysRevLett.123.033201 (cit. on pp. 7, 78).

- [16] M. Brownnutt, M. Kumph, P. Rabl, and R. Blatt. “Ion-Trap Measurements of Electric-Field Noise near Surfaces”. In: *Reviews of Modern Physics* 87.4 (2015), pp. 1419–1482. DOI: 10.1103/RevModPhys.87.1419 (cit. on pp. 77, 78).
- [17] T. Burgermeister. “Development and Characterization of a Linear Ion Trap for an Improved Optical Clock Performance”. PhD thesis. Leibniz Universität Hannover, 2019 (cit. on p. 15).
- [18] J. Cao, P. Zhang, J. Shang, K. Cui, J. Yuan, S. Chao, S. Wang, H. Shu, and X. Huang. “A Compact, Transportable Single-Ion Optical Clock with 7.8×10^{-17} Systematic Uncertainty”. In: *Applied Physics B* 123.4 (2017), p. 112. DOI: 10.1007/s00340-017-6671-5 (cit. on p. 33).
- [19] J.-S. Chen, K. Wright, N. C. Piseni, D. Murphy, K. M. Beck, K. Landsman, J. M. Amini, and Y. Nam. “Efficient-Sideband-Cooling Protocol for Long Trapped-Ion Chains”. In: *Physical Review A* 102.4 (2020), p. 043110. DOI: 10.1103/PhysRevA.102.043110 (cit. on pp. 11, 71).
- [20] M. Chwalla, J. Benhelm, K. Kim, G. Kirchmair, T. Monz, M. Riebe, P. Schindler, A. Villar, W. Hänsel, C. Roos, R. Blatt, M. Abgrall, G. Santarelli, G. Rovera, and P. Laurent. “Absolute Frequency Measurement of the $^{40}\text{Ca}^+ 4s^2S_{1/2} - 3d^2D_{5/2}$ Clock Transition”. In: *Physical Review Letters* 102.2 (2009), p. 023002. DOI: 10.1103/PhysRevLett.102.023002 (cit. on pp. 80, 89).
- [21] M. Chwalla. “Precision spectroscopy with $^{40}\text{Ca}^+$ ions in a Paul trap”. PhD thesis. Innsbruck: Leopold-Franzens-Universität Innsbruck, 2009 (cit. on p. 81).
- [22] S. Cook, T. Rosenband, and D. R. Leibbrandt. “Laser-Frequency Stabilization Based on Steady-State Spectral-Hole Burning in $\text{Eu}^{3+} : \text{Y}_2\text{SiO}_5$ ”. In: *Physical Review Letters* 114.25 (2015), p. 253902. DOI: 10.1103/PhysRevLett.114.253902 (cit. on p. 10).
- [23] C. Degenhardt, T. Nazarova, C. Lisdat, H. Stoehr, U. Sterr, and F. Riehle. “Influence of Chirped Excitation Pulses in an Optical Clock With Ultracold Calcium Atoms”. In: *IEEE Transactions on Instrumentation and Measurement* 54.2 (2005), pp. 771–775. DOI: 10.1109/TIM.2004.843388 (cit. on p. 120).

- [24] G. J. Dick, J. D. Prestage, C. A. Greenhall, and L. Maleki. “Local Oscillator Induced Degradation of Medium-Term Stability in Passive Atomic Frequency Standards”. In: *Proceedings of the 22th Annual Precise Time and Time Interval Systems and Applications Meeting*. 1990, pp. 487–508 (cit. on p. 6).
- [25] K. Dietze. “Zustandskontrolle Und Dynamical Decoupling Mit Pulssequenzen Für Gefangene Ionen”. MA thesis. Braunschweig: Technische Universität Braunschweig, 2019 (cit. on p. 135).
- [26] S. Dörscher, A. Al-Masoudi, M. Bober, R. Schwarz, R. Hobson, U. Sterr, and C. Lisdat. “Dynamical Decoupling of Laser Phase Noise in Compound Atomic Clocks”. In: *Communications Physics* 3.1 (2020), pp. 1–9. DOI: 10.1038/s42005-020-00452-9 (cit. on pp. 10, 138).
- [27] A. Drakoudis, M. Söllner, and G. Werth. “Instabilities of Ion Motion in a Linear Paul Trap”. In: *International Journal of Mass Spectrometry* 252.1 (2006), pp. 61–68. DOI: 10.1016/j.ijms.2006.02.006 (cit. on pp. 123, 140).
- [28] M. Drechsler, S. Wolf, C. T. Schmiegelow, and F. Schmidt-Kaler. “Optical Superresolution Sensing of a Trapped Ion’s Wave Packet Size”. In: *Physical Review Letters* 127.14 (2021), p. 143602. DOI: 10.1103/PhysRevLett.127.143602 (cit. on p. 51).
- [29] R. W. P. Drever, J. L. Hall, F. V. Kowalski, J. Hough, G. M. Ford, A. J. Munley, and H. Ward. “Laser Phase and Frequency Stabilization Using an Optical Resonator”. In: *Applied Physics B* 31.2 (1983), pp. 97–105. DOI: 10.1007/BF00702605 (cit. on p. 39).
- [30] P. Dubé, A. A. Madej, and B. Jian. “Sr + Single-Ion Clock”. In: *Journal of Physics: Conference Series* 723 (2016), p. 012018. DOI: 10.1088/1742-6596/723/1/012018 (cit. on p. 82).
- [31] P. Dubé, A. A. Madej, M. Tibbo, and J. E. Bernard. “High-Accuracy Measurement of the Differential Scalar Polarizability of a $^{88}\text{Sr}^+$ Clock Using the Time-Dilation Effect”. In: *Physical Review Letters* 112.17 (2014), p. 173002. DOI: 10.1103/PhysRevLett.112.173002 (cit. on pp. 82, 86).

- [32] P. Dubé, A. A. Madej, Z. Zhou, and J. E. Bernard. “Evaluation of systematic shifts of the $^{88}\text{Sr}^+$ single-ion optical frequency standard at the 10^{-17} level”. In: *Physical Review A* 87.2 (2013), p. 023806. DOI: 10.1103/PhysRevA.87.023806 (cit. on pp. 7, 81).
- [33] D. G. Enzer, M. M. Schauer, J. J. Gomez, M. S. Gulley, M. H. Holzscheiter, P. G. Kwiat, S. K. Lamoreaux, C. G. Peterson, V. D. Sandberg, D. Tupa, A. G. White, R. J. Hughes, and D. F. V. James. “Observation of Power-Law Scaling for Phase Transitions in Linear Trapped Ion Crystals”. In: *Physical Review Letters* 85.12 (2000), pp. 2466–2469. DOI: 10.1103/PhysRevLett.85.2466 (cit. on pp. 124, 147).
- [34] J. Eschner, G. Morigi, F. Schmidt-Kaler, and R. Blatt. “Laser Cooling of Trapped Ions”. In: *JOSA B* 20.5 (2003), pp. 1003–1015. DOI: 10.1364/JOSAB.20.001003 (cit. on pp. 11, 68).
- [35] L. Essen and J. V. L. Parry. “An Atomic Standard of Frequency and Time Interval: A Cæsium Resonator”. In: *Nature* 176.4476 (1955), pp. 280–282. DOI: 10.1038/176280a0 (cit. on p. 3).
- [36] R. Finkelstein, O. Lahad, I. Cohen, O. Davidson, S. Kiriati, E. Poem, and O. Firstenberg. “Continuous Protection of a Collective State from Inhomogeneous Dephasing”. In: *Physical Review X* 11.1 (2021), p. 011008. DOI: 10.1103/PhysRevX.11.011008 (cit. on p. 134).
- [37] M. Fleischhauer, A. Imamoglu, and J. P. Marangos. “Electromagnetically Induced Transparency: Optics in Coherent Media”. In: *Reviews of Modern Physics* 77.2 (2005), pp. 633–673. DOI: 10.1103/RevModPhys.77.633 (cit. on p. 71).
- [38] S. M. Foreman, A. D. Ludlow, M. H. G. de Miranda, J. E. Stalnaker, S. A. Diddams, and J. Ye. “Coherent Optical Phase Transfer over a 32-km Fiber with 1 s Instability at 10^{-17} ”. In: *Physical Review Letters* 99.15 (2007). DOI: 10.1103/PhysRevLett.99.153601 (cit. on p. 41).
- [39] A. Franzen. *Component Library*. <http://www.gwoptics.org/ComponentLibrary/> Published according to <http://creativecommons.org/licenses/by-nc/3.0/>. 2009 (cit. on p. 37).

- [40] J. Gambetta, W. A. Braff, A. Wallraff, S. M. Girvin, and R. J. Schoelkopf. "Protocols for Optimal Readout of Qubits Using a Continuous Quantum Nondemolition Measurement". In: *Physical Review A* 76.1 (2007), p. 012325. DOI: 10.1103/PhysRevA.76.012325 (cit. on p. 54).
- [41] P. Gill. "When Should We Change the Definition of the Second?" In: *Philosophical Transactions of the Royal Society A: Mathematical, Physical and Engineering Sciences* 369.1953 (2011), pp. 4109–4130. DOI: 10.1098/rsta.2011.0237 (cit. on p. 7).
- [42] D. A. Golter, T. K. Baldwin, and H. Wang. "Protecting a Solid-State Spin from Decoherence Using Dressed Spin States". In: *Physical Review Letters* 113.23 (2014), p. 237601. DOI: 10.1103/PhysRevLett.113.237601 (cit. on p. 94).
- [43] G. Grosche. "Eavesdropping Time and Frequency: Phase Noise Cancellation along a Time-Varying Path, Such as an Optical Fiber". In: *Optics Letters* 39.9 (2014), pp. 2545–2548. DOI: 10.1364/OL.39.002545 (cit. on p. 41).
- [44] J. Grotti, S. Koller, S. Vogt, S. Häfner, U. Sterr, C. Lisdat, H. Denker, C. Voigt, L. Timmen, A. Rolland, F. N. Baynes, H. S. Margolis, M. Zampaolo, P. Thoumany, M. Pizzocaro, et al. "Geodesy and Metrology with a Transportable Optical Clock". In: *Nature Physics* 14.5 (2018), pp. 437–441. DOI: 10.1038/s41567-017-0042-3 (cit. on p. 8).
- [45] S. Gulde, D. Rotter, P. Barton, F. Schmidt-Kaler, R. Blatt, and W. Hogervorst. "Simple and Efficient Photo-Ionization Loading of Ions for Precision Ion-Trapping Experiments". In: *Applied Physics B* 73.8 (2001), pp. 861–863. DOI: 10.1007/s003400100749 (cit. on p. 34).
- [46] S. Häfner, S. Falke, C. Grebing, S. Vogt, T. Legero, M. Merimaa, C. Lisdat, and U. Sterr. " 8×10^{-17} fractional laser frequency instability with a long room-temperature cavity". In: *Optics Letters* 40.9 (2015), p. 2112. DOI: 10.1364/OL.40.002112 (cit. on p. 41).
- [47] E. L. Hahn. "Spin Echoes". In: *Physical Review* 80.4 (1950), pp. 580–594. DOI: 10.1103/PhysRev.80.580 (cit. on p. 93).
- [48] J. L. Hall. "Nobel Lecture: Defining and Measuring Optical Frequencies". In: *Reviews of Modern Physics* 78.4 (2006), pp. 1279–1295. DOI: 10.1103/RevModPhys.78.1279 (cit. on p. 5).

- [49] S. Hannig, L. Pelzer, N. Scharnhorst, J. Kramer, M. Stepanova, Z. T. Xu, N. Spethmann, I. D. Leroux, T. E. Mehlstäubler, and P. O. Schmidt. “Towards a Transportable Aluminium Ion Quantum Logic Optical Clock”. In: *Review of Scientific Instruments* 90.5 (2019), p. 053204. DOI: 10.1063/1.5090583 (cit. on pp. 13, 33, 35, 51, 82, 87).
- [50] S. Hannig. “Development and Characterization of a Transportable Aluminum Ion Quantum Logic Optical Clock Setup”. PhD thesis. Leibniz Universität Hannover, 2018 (cit. on pp. 13, 15, 16, 33, 35, 38, 49, 51, 87).
- [51] T. Hänsch and A. Schawlow. “Cooling of Gases by Laser Radiation”. In: *Optics Communications* 13.1 (1975), pp. 68–69. DOI: 10.1016/0030-4018(75)90159-5 (cit. on p. 67).
- [52] S. W. Hell and J. Wichmann. “Breaking the Diffraction Resolution Limit by Stimulated Emission: Stimulated-Emission-Depletion Fluorescence Microscopy”. In: *Optics Letters* 19.11 (1994), pp. 780–782. DOI: 10.1364/OL.19.000780 (cit. on p. 51).
- [53] B. Hemmerling, F. Gebert, Y. Wan, and P. O. Schmidt. “A Novel, Robust Quantum Detection Scheme”. In: *New Journal of Physics* 14.2 (2012), p. 023043. DOI: 10.1088/1367-2630/14/2/023043 (cit. on p. 53).
- [54] R. Hendricks, D. Grant, P. Herskind, A. Dantan, and M. Drewsen. “An All-Optical Ion-Loading Technique for Scalable Microtrap Architectures”. In: *Applied Physics B* 88.4 (2007), pp. 507–513. DOI: 10.1007/s00340-007-2698-3 (cit. on p. 34).
- [55] N. Herschbach, K. Pyka, J. Keller, and T. E. Mehlstäubler. “Linear Paul Trap Design for an Optical Clock with Coulomb Crystals”. In: *Applied Physics B* 107.4 (2012), pp. 891–906. DOI: 10.1007/s00340-011-4790-y (cit. on pp. 15, 63).
- [56] Y. Huang, H. Guan, M. Zeng, L. Tang, and K. Gao. “ $^{40}\text{Ca}^+$ ion optical clock with micromotion-induced shifts below 1×10^{-18} ”. In: *Physical Review A* 99.1 (2019), p. 011401. DOI: 10.1103/PhysRevA.99.011401 (cit. on pp. 82, 86).
- [57] Y. Huang, B. Zhang, M. Zeng, H. Zhang, Y. Hao, Z. Chen, M. Wang, H. Guan, and K. Gao. “Nearly continuous Ca^+ optical clocks with stability at the 10^{-18} level”. In: (2021). DOI: 10.21203/rs.3.rs-120082/v1 (cit. on p. 81).

- [58] D. B. Hume and D. R. Leibbrandt. “Probing beyond the Laser Coherence Time in Optical Clock Comparisons”. In: *Physical Review A* 93.3 (2016), p. 032138. DOI: 10.1103/PhysRevA.93.032138 (cit. on pp. 10, 138).
- [59] N. Huntemann, C. Sanner, B. Lipphardt, C. Tamm, and E. Peik. “Single-Ion Atomic Clock with 3×10^{-18} Systematic Uncertainty”. In: *Physical Review Letters* 116.6 (2016), p. 063001. DOI: 10.1103/PhysRevLett.116.063001 (cit. on pp. 7, 82).
- [60] W. M. Itano, J. C. Bergquist, J. J. Bollinger, J. M. Gilligan, D. J. Heinzen, F. L. Moore, M. G. Raizen, and D. J. Wineland. “Quantum Projection Noise: Population Fluctuations in Two-Level Systems”. In: *Physical Review A* 47.5 (1993), pp. 3554–3570. DOI: 10.1103/PhysRevA.47.3554 (cit. on p. 9).
- [61] W. Itano. “External-field shifts of the $^{199}\text{Hg}^+$ optical frequency standard”. In: *Journal of Research of the National Institute of Standards and Technology* 105.6 (2000), p. 829. DOI: 10.6028/jres.105.065 (cit. on pp. 88, 93).
- [62] D. James. “Quantum Dynamics of Cold Trapped Ions with Application to Quantum Computation”. In: *Applied Physics B* 66.2 (1998), pp. 181–190. DOI: 10.1007/s003400050373 (cit. on pp. 59, 147).
- [63] M. Johanning. “Isospaced Linear Ion Strings”. In: *Applied Physics B* 122.4 (2016), p. 71. DOI: 10.1007/s00340-016-6340-0 (cit. on p. 123).
- [64] M. K. Joshi, A. Fabre, C. Maier, T. Brydges, D. Kiesenhofer, H. Hainzer, R. Blatt, and C. F. Roos. “Polarization-Gradient Cooling of 1D and 2D Ion Coulomb Crystals”. In: *New Journal of Physics* 22.10 (2020), p. 103013. DOI: 10.1088/1367-2630/abb912 (cit. on p. 11).
- [65] R. Kaewuam, T. R. Tan, K. J. Arnold, S. R. Chanu, Z. Zhang, and M. D. Barrett. “Hyperfine Averaging by Dynamic Decoupling in a Multi-Ion Lutetium Clock”. In: *Physical Review Letters* 124.8 (2020), p. 083202. DOI: 10.1103/PhysRevLett.124.083202 (cit. on pp. 94, 134).
- [66] D. Kalincev, L. S. Dreissen, A. P. Kulosa, C.-H. Yeh, H. A. Fürst, and T. E. Mehlstäubler. “Motional Heating of Spatially Extended Ion Crystals”. In: *Quantum Science and Technology* 6.3 (2021), p. 034003. DOI: 10.1088/2058-9565/abee99 (cit. on pp. 11, 78, 79, 139).

- [67] J. Keller, T. Burgermeister, D. Kalincev, A. Didier, A. P. Kulosa, T. Nordmann, J. Kiethe, and T. E. Mehlstäubler. “Controlling systematic frequency uncertainties at the 10^{-19} level in linear Coulomb crystals”. In: *Physical Review A* 99.1 (2019), p. 013405. DOI: 10.1103/PhysRevA.99.013405 (cit. on pp. 11, 15, 78, 123).
- [68] J. Keller, D. Kalincev, T. Burgermeister, A. P. Kulosa, A. Didier, T. Nordmann, J. Kiethe, and T. Mehlstäubler. “Probing Time Dilation in Coulomb Crystals in a High-Precision Ion Trap”. In: *Physical Review Applied* 11.1 (2019), p. 011002. DOI: 10.1103/PhysRevApplied.11.011002 (cit. on p. 83).
- [69] J. Keller, H. L. Partner, T. Burgermeister, and T. E. Mehlstäubler. “Precise Determination of Micromotion for Trapped-Ion Optical Clocks”. In: *Journal of Applied Physics* 118.10 (2015), p. 104501. DOI: 10.1063/1.4930037 (cit. on pp. 83, 85).
- [70] E. M. Kessler, P. Kómár, M. Bishof, L. Jiang, A. S. Sørensen, J. Ye, and M. D. Lukin. “Heisenberg-Limited Atom Clocks Based on Entangled Qubits”. In: *Physical Review Letters* 112.19 (2014), p. 190403. DOI: 10.1103/PhysRevLett.112.190403 (cit. on p. 10).
- [71] S. A. King, T. Leopold, P. Thekkeppatt, and P. O. Schmidt. “A Self-Injection Locked DBR Laser for Laser Cooling of Beryllium Ions”. In: *Applied Physics B* 124.11 (2018), p. 214. DOI: 10.1007/s00340-018-7080-0 (cit. on p. 40).
- [72] A. Kreuter, C. Becher, G. P. T. Lancaster, A. B. Mundt, C. Russo, H. Häffner, C. Roos, W. Hänsel, F. Schmidt-Kaler, R. Blatt, and M. S. Safronova. “Experimental and theoretical study of the $3d^2D$ -level lifetimes of $^{40}\text{Ca}^+$ ”. In: *Physical Review A* 71.3 (2005), p. 032504. DOI: 10.1103/PhysRevA.71.032504 (cit. on pp. 118, 121).
- [73] R. Lange, N. Huntemann, J. M. Rahm, C. Sanner, H. Shao, B. Lipphardt, C. Tamm, S. Weyers, and E. Peik. “Improved Limits for Violations of Local Position Invariance from Atomic Clock Comparisons”. In: *Physical Review Letters* 126.1 (2021), p. 011102. DOI: 10.1103/PhysRevLett.126.011102 (cit. on p. 8).
- [74] R. Lange, N. Huntemann, C. Sanner, H. Shao, B. Lipphardt, C. Tamm, and E. Peik. “Coherent Suppression of Tensor Frequency Shifts through Magnetic Field Rota-

- tion". In: *Physical Review Letters* 125.14 (2020), p. 143201. DOI: 10.1103/PhysRevLett.125.143201 (cit. on p. 93).
- [75] R. Lechner, C. Maier, C. Hempel, P. Jurcevic, B. P. Lanyon, T. Monz, M. Brownnutt, R. Blatt, and C. F. Roos. "Electromagnetically-Induced-Transparency Ground-State Cooling of Long Ion Strings". In: *Physical Review A* 93.5 (2016). DOI: 10.1103/PhysRevA.93.053401 (cit. on pp. 11, 73).
- [76] D. Leibfried, M. D. Barrett, T. Schaetz, J. Britton, J. Chiaverini, W. M. Itano, J. D. Jost, C. Langer, and D. J. Wineland. "Toward Heisenberg-limited Spectroscopy with Multiparticle Entangled States". In: *Science* 304.5676 (2004), p. 1476 (cit. on p. 10).
- [77] D. Leibfried, R. Blatt, C. Monroe, and D. Wineland. "Quantum Dynamics of Single Trapped Ions". In: *Reviews of Modern Physics* 75.1 (2003), pp. 281–324. DOI: 10.1103/RevModPhys.75.281 (cit. on pp. 61, 65).
- [78] I. D. Leroux, N. Scharnhorst, S. Hannig, J. Kramer, L. Pelzer, M. Stepanova, and P. O. Schmidt. "On-Line Estimation of Local Oscillator Noise and Optimisation of Servo Parameters in Atomic Clocks". In: *Metrologia* 54.3 (2017), pp. 307–321. DOI: 10.1088/1681-7575/aa66e9 (cit. on pp. 10, 123, 138).
- [79] P. D. Lett, C. I. Westbrook, R. N. Watts, S. L. Rolston, P. L. Gould, H. J. Metcalf, and W. D. Phillips. "Atoms Laser-Cooled Below the Doppler-Cooling Limit". In: *Frequency Standards and Metrology*. Ed. by A. De Marchi. Berlin, Heidelberg: Springer, 1989, pp. 264–269. DOI: 10.1007/978-3-642-74501-0_45 (cit. on p. 68).
- [80] A. D. Ludlow, M. M. Boyd, J. Ye, E. Peik, and P. O. Schmidt. "Optical Atomic Clocks". In: *Reviews of Modern Physics* 87.2 (2015), pp. 637–701. DOI: 10.1103/RevModPhys.87.637 (cit. on pp. 81, 88).
- [81] H. Lyons. "The Atomic Clock". In: *Instruments* 22.174 (1949), pp. 133–165 (cit. on p. 3).
- [82] M-Labs. ARTIQ | M-Labs. <https://m-labs.hk/experiment-control/artiq/>. 2021 (cit. on p. 135).
- [83] L.-S. Ma, P. Jungner, J. Ye, and J. L. Hall. "Delivering the Same Optical Frequency at Two Places: Accurate Cancellation of Phase Noise Introduced by an Optical Fiber or Other Time-Varying Path". In: *Optics Letters* 19.21 (1994), p. 1777. DOI: 10.1364/OL.19.001777 (cit. on p. 41).

- [84] W. Macalpine and R. Schildknecht. “Coaxial Resonators with Helical Inner Conductor”. In: *Proceedings of the IRE* 47.12 (1959), pp. 2099–2105. DOI: 10.1109/JRPR0C.1959.287128 (cit. on p. 17).
- [85] A. A. Madej, P. Dubé, Z. Zhou, J. E. Bernard, and M. Gertsvolf. “ $^{88}\text{Sr}^+$ 445-THz Single-Ion Reference at the 10^{-17} Level via Control and Cancellation of Systematic Uncertainties and Its Measurement against the SI Second”. In: *Physical Review Letters* 109.20 (2012), p. 203002. DOI: 10.1103/PhysRevLett.109.203002 (cit. on p. 89).
- [86] T. H. Maiman. “Stimulated Optical Radiation in Ruby”. In: *Nature* 187.4736 (1960), pp. 493–494. DOI: 10.1038/187493a0 (cit. on p. 5).
- [87] Z.-C. Mao, Y.-Z. Xu, Q.-X. Mei, W.-D. Zhao, Y. Jiang, Y. Wang, X.-Y. Chang, L. He, L. Yao, Z.-C. Zhou, Y.-K. Wu, and L.-M. Duan. “Experimental Realization of Multi-ion Sympathetic Cooling on a Trapped Ion Crystal”. In: *Physical Review Letters* 127.14 (2021), p. 143201. DOI: 10.1103/PhysRevLett.127.143201 (cit. on p. 11).
- [88] V. J. Martínez-Lahuerta, L. Pelzer, K. Dietze, L. Krinner, P. O. Schmidt, and K. Hammerer. *Quadrupole Transitions and Quantum Gates Protected by Continuous Dynamic Decoupling*. 2023. DOI: 10.48550/arXiv.2301.07974. arXiv: 2301.07974 [quant-ph] (cit. on pp. 95, 98, 109, 111).
- [89] D. G. Matei, T. Legero, S. Häfner, C. Grebing, R. Weyrich, W. Zhang, L. Sonderhouse, J. M. Robinson, J. Ye, F. Riehle, and U. Sterr. “1.5 μm Lasers with Sub-10 mHz Linewidth”. In: *Physical Review Letters* 118.26 (2017), p. 263202. DOI: 10.1103/PhysRevLett.118.263202 (cit. on pp. 10, 35, 47, 48).
- [90] W. F. McGrew, X. Zhang, R. J. Fasano, S. A. Schäffer, K. Beloy, D. Nicolodi, R. C. Brown, N. Hinkley, G. Milani, M. Schioppo, T. H. Yoon, and A. D. Ludlow. “Atomic Clock Performance Enabling Geodesy below the Centimetre Level”. In: *Nature* 564.7734 (2018), pp. 87–90. DOI: 10.1038/s41586-018-0738-2 (cit. on p. 7).
- [91] T. E. Mehlstäubler, G. Grosche, C. Lisdat, P. O. Schmidt, and H. Denker. “Atomic Clocks for Geodesy”. In: *Reports on Progress in Physics* 81.6 (2018), p. 064401. DOI: 10.1088/1361-6633/aab409 (cit. on p. 8).

- [92] P. Micke, T. Leopold, S. A. King, E. Benkler, L. J. Spieß, L. Schmöger, M. Schwarz, J. R. C. López-Urrutia, and P. O. Schmidt. “Coherent Laser Spectroscopy of Highly Charged Ions Using Quantum Logic”. In: *Nature* 578.7793 (2020), pp. 60–65. DOI: 10.1038/s41586-020-1959-8 (cit. on pp. 7, 8, 76).
- [93] J. Millo, D. Magalhães, C. Mandache, Y. Le Coq, E. English, P. Westergaard, J. Lodewyck, S. Bize, P. Lemonde, and G. Santarelli. “Ultrastable Lasers Based on Vibration Insensitive Cavities”. In: *Physical Review A* 79.5 (2009), p. 053829. DOI: 10.1103/PhysRevA.79.053829 (cit. on p. 41).
- [94] W. R. Milner, J. M. Robinson, C. J. Kennedy, T. Bothwell, D. Kedar, D. G. Matei, T. Legero, U. Sterr, F. Riehle, H. Leopardi, T. M. Fortier, J. A. Sherman, J. Levine, J. Yao, J. Ye, and E. Oelker. “Demonstration of a Timescale Based on a Stable Optical Carrier”. In: *Physical Review Letters* 123.17 (2019), p. 173201. DOI: 10.1103/PhysRevLett.123.173201 (cit. on p. 48).
- [95] C. Monroe, D. M. Meekhof, B. E. King, S. R. Jefferts, W. M. Itano, D. J. Wineland, and P. Gould. “Resolved-Sideband Raman Cooling of a Bound Atom to the 3D Zero-Point Energy”. In: *Physical Review Letters* 75.22 (1995), pp. 4011–4014. DOI: 10.1103/PhysRevLett.75.4011 (cit. on p. 65).
- [96] T. Monz. “Quantum Information Processing beyond Ten Ion-Qubits”. PhD thesis. University of Innsbruck, 2011 (cit. on p. 60).
- [97] W. Neuhauser, M. Hohenstatt, P. Toschek, and H. Dehmelt. “Optical-Sideband Cooling of Visible Atom Cloud Confined in Parabolic Well”. In: *Physical Review Letters* 41.4 (1978), pp. 233–236. DOI: 10.1103/PhysRevLett.41.233 (cit. on p. 67).
- [98] NobelPrize.org. *The Nobel Prize in Physics 2005*. Nobel Prize Outreach AB 2021 www.nobelprize.org/prizes/physics/2005/summary/. 2021 (cit. on p. 44).
- [99] A. Noguchi, S. Haze, K. Toyoda, and S. Urabe. “Generation of a Decoherence-Free Entangled State Using a Radio-Frequency Dressed State”. In: *Physical Review Letters* 108.6 (2012), p. 060503. DOI: 10.1103/PhysRevLett.108.060503 (cit. on p. 94).

- [100] T. Nordmann, A. Didier, M. Doležal, P. Balling, T. Burgermeister, and T. E. Mehlstäubler. “Sub-Kelvin Temperature Management in Ion Traps for Optical Clocks”. In: *Review of Scientific Instruments* 91.11 (2020), p. 111301. DOI: 10.1063/5.0024693 (cit. on p. 82).
- [101] W. Paul. “Electromagnetic Traps for Charged and Neutral Particles”. In: *Reviews of Modern Physics* 62.3 (1990), pp. 531–540. DOI: 10.1103/RevModPhys.62.531 (cit. on p. 6).
- [102] *Pco.Edge 4.2 LT Data Sheet*. www.pco.de/fileadmin/user_upload/pco-product_sheets/pco.edge_42_lt_data_sheet.pdf. Data Sheet (cit. on p. 53).
- [103] L. Pelzer, K. Dietze, J. Kramer, F. Dawel, L. Krinner, N. Spethmann, V. Martinez, N. Aharon, A. Retzker, K. Hammerer, and P. O. Schmidt. “Tailored optical clock transition in $^{40}\text{Ca}^+$ ”. In: *Measurement: Sensors* 18 (2021), p. 100326. DOI: 10.1016/j.measen.2021.100326 (cit. on pp. 34, 108).
- [104] P. T. T. Pham. “A General-Purpose Pulse Sequencer for Quantum Computing”. PhD thesis. Cambridge, Massachusetts, USA: Massachusetts Institute of Technology, 2005 (cit. on p. 23).
- [105] I. Pogorelov, T. Feldker, C. D. Marciniak, L. Postler, G. Jacob, O. Krieglsteiner, V. Podlesnic, M. Meth, V. Negnevitsky, M. Stadler, B. Höfer, C. Wächter, K. Lakhmanskiy, R. Blatt, P. Schindler, and T. Monz. “Compact Ion-Trap Quantum Computing Demonstrator”. In: *PRX Quantum* 2.2 (2021), p. 020343. DOI: 10.1103/PRXQuantum.2.020343 (cit. on p. 33).
- [106] K. Pyka. “High-Precision Ion Trap for Spectroscopy of Coulomb Crystals”. PhD thesis. Universität Hannover, 2010 (cit. on p. 15).
- [107] N. F. Ramsey. “A Molecular Beam Resonance Method with Separated Oscillating Fields”. In: *Physical Review* 78.6 (1950), pp. 695–699. DOI: 10.1103/PhysRev.78.695 (cit. on p. 60).
- [108] F. Riehle. *Frequency Standards: Basics and Applications*. Weinheim: Wiley-VCH, 2004 (cit. on p. 10).

- [109] F. Riehle. “Towards a Redefinition of the Second Based on Optical Atomic Clocks”. In: *Comptes Rendus Physique. The Measurement of Time / La Mesure Du Temps* 16.5 (2015), pp. 506–515. DOI: 10.1016/j.crhy.2015.03.012 (cit. on p. 7).
- [110] W. J. Riley and W. J. Riley. *Handbook of Frequency Stability Analysis*. Tech. rep. NIST SP 1065. Gaithersburg, MD: National Institute of Standards and Technology, 2008, NIST SP 1065. DOI: 10.6028/NIST.SP.1065 (cit. on pp. 9, 119).
- [111] C. F. Roos, M. Chwalla, K. Kim, M. Riebe, and R. Blatt. “‘Designer Atoms’ for Quantum Metrology”. In: *Nature* 443.7109 (2006), pp. 316–319. DOI: 10.1038/nature05101 (cit. on p. 88).
- [112] C. F. Roos, D. Leibfried, A. Mundt, F. Schmidt-Kaler, J. Eschner, and R. Blatt. “Experimental Demonstration of Ground State Laser Cooling with Electromagnetically Induced Transparency”. In: *Physical Review Letters* 85.26 (2000), pp. 5547–5550. DOI: 10.1103/PhysRevLett.85.5547 (cit. on p. 71).
- [113] C. Roos. “Controlling the Quantum State of Trapped Ions”. PhD thesis. Leopold-Franzens-Universität Innsbruck, 2000 (cit. on pp. 54, 63, 80).
- [114] T. Rosenband, D. B. Hume, P. O. Schmidt, C. W. Chou, A. Bruschi, L. Lorini, W. H. Oskay, R. E. Drullinger, T. M. Fortier, J. E. Stalnaker, S. A. Diddams, W. C. Swann, N. R. Newbury, W. M. Itano, D. J. Wineland, and J. C. Bergquist. “Frequency Ratio of Al^+ and Hg^+ Single-Ion Optical Clocks; Metrology at the 17th Decimal Place”. In: *Science* 319.5871 (2008), pp. 1808–1812. DOI: 10.1126/science.1154622 (cit. on pp. 7, 8).
- [115] T. Ruster, C. T. Schmiegelow, H. Kaufmann, C. Warschburger, F. Schmidt-Kaler, and U. G. Poschinger. “A Long-Lived Zeeman Trapped-Ion Qubit”. In: *Applied Physics B* 122.10 (2016), p. 254. DOI: 10.1007/s00340-016-6527-4 (cit. on pp. 21, 60, 81, 93).
- [116] M. S. Safronova, D. Budker, D. DeMille, D. F. J. Kimball, A. Derevianko, and C. W. Clark. “Search for New Physics with Atoms and Molecules”. In: *Reviews of Modern Physics* 90.2 (2018), p. 025008. DOI: 10.1103/RevModPhys.90.025008 (cit. on p. 7).

- [117] M. S. Safronova and U. I. Safronova. “Blackbody radiation shift, multipole polarizabilities, oscillator strengths, lifetimes, hyperfine constants, and excitation energies in Ca^+ ”. In: *Physical Review A* 83.1 (2011), p. 012503. DOI: 10.1103/PhysRevA.83.012503 (cit. on p. 82).
- [118] F. Scazza, G. Del Pace, L. Pieri, R. Concas, W. J. Kwon, and G. Roati. “An Efficient High-Current Circuit for Fast Radio-Frequency Spectroscopy in Cold Atomic Gases”. In: *arXiv:2104.12730 [cond-mat, physics:physics]* (2021). arXiv: 2104.12730 [cond-mat, physics:physics] (cit. on pp. 117, 133).
- [119] N. Scharnhorst. “Multi-Mode Ground State Cooling of Trapped Ions”. PhD thesis. Hannover: Leibniz Universität Hannover, 2018 (cit. on pp. 74, 76).
- [120] N. Scharnhorst, J. Cerrillo, J. Kramer, I. D. Leroux, J. B. Wübbena, A. Retzker, and P. O. Schmidt. “Experimental and Theoretical Investigation of a Multimode Cooling Scheme Using Multiple Electromagnetically-Induced-Transparency Resonances”. In: *Physical Review A* 98.2 (2018), p. 023424. DOI: 10.1103/PhysRevA.98.023424 (cit. on pp. 73, 74).
- [121] N. Scharnhorst, J. B. Wübbena, S. Hannig, K. Jakobsen, J. Kramer, I. D. Leroux, and P. O. Schmidt. “High-Bandwidth Transfer of Phase Stability through a Fiber Frequency Comb”. In: *Optics Express* 23.15 (2015), pp. 19771–19776. DOI: 10.1364/OE.23.019771 (cit. on pp. 38, 44).
- [122] P. Schindler. “Frequency Synthesis and Pulse Shaping for Quantum Information Processing with Trapped Ions”. Diploma Thesis. Innsbruck, Austria: University of Innsbruck, 2008 (cit. on p. 23).
- [123] P. O. Schmidt, T. Rosenband, C. Langer, W. M. Itano, J. C. Bergquist, and D. J. Wineland. “Spectroscopy Using Quantum Logic”. In: *Science* 309.5735 (2005), pp. 749–752. DOI: 10.1126/science.1114375 (cit. on p. 7).
- [124] P. O. Schmidt, S. Hensler, J. Werner, T. Binhammer, A. Görlitz, and T. Pfau. “Doppler Cooling of an Optically Dense Cloud of Magnetically Trapped Atoms”. In: *Journal of the Optical Society of America B* 20.5 (2003), p. 960. DOI: 10.1364/JOSAB.20.000960 (cit. on p. 68).

- [125] H. Schnatz, B. Lipphardt, J. Helmcke, F. Riehle, and G. Zinner. "First Phase-Coherent Frequency Measurement of Visible Radiation". In: *Physical Review Letters* 76.1 (1996), pp. 18–21. DOI: 10.1103/PhysRevLett.76.18 (cit. on pp. 5, 44).
- [126] T. Schneider, E. Peik, and C. Tamm. "Sub-Hertz Optical Frequency Comparisons between Two Trapped $^{171}\text{Yb}^+$ Ions". In: *Physical Review Letters* 94.23 (2005), p. 230801. DOI: 10.1103/PhysRevLett.94.230801 (cit. on pp. 93, 126).
- [127] J.-J. Shang, K.-F. Cui, J. Cao, S.-M. Wang, S.-J. Chao, H.-L. Shu, and X.-R. Huang. "Sympathetic Cooling of $^{40}\text{Ca}^+$ $^{27}\text{Al}^+$ Ion Pair Crystal in a Linear Paul Trap". In: *Chinese Physics Letters* 33.10 (2016), p. 103701. DOI: 10.1088/0256-307X/33/10/103701 (cit. on p. 76).
- [128] R. Shaniv, N. Akerman, T. Manovitz, Y. Shapira, and R. Ozeri. "Quadrupole Shift Cancellation Using Dynamic Decoupling". In: *Physical Review Letters* 122.22 (2019), p. 223204. DOI: 10.1103/PhysRevLett.122.223204 (cit. on pp. 94, 134).
- [129] J. D. Siverns, L. R. Simkins, S. Weidt, and W. K. Hensinger. "On the Application of Radio Frequency Voltages to Ion Traps via Helical Resonators". In: *Applied Physics B* 107.4 (2012), pp. 921–934. DOI: 10.1007/s00340-011-4837-0 (cit. on p. 17).
- [130] A. M. Souza, G. A. Álvarez, and D. Suter. "Experimental Protection of Quantum Gates against Decoherence and Control Errors". In: *Physical Review A* 86.5 (2012), p. 050301. DOI: 10.1103/PhysRevA.86.050301 (cit. on p. 94).
- [131] M. Stepanova. "Setup of a logic laser for Ca^+ ". MA thesis. Hannover: Leibniz Universität Hannover, 2017 (cit. on p. 38).
- [132] M. Takamoto, I. Ushijima, N. Ohmae, T. Yahagi, K. Kokado, H. Shinkai, and H. Katori. "Test of General Relativity by a Pair of Transportable Optical Lattice Clocks". In: *Nature Photonics* 14.7 (2020), pp. 411–415. DOI: 10.1038/s41566-020-0619-8 (cit. on p. 8).

- [133] C. Tamm, N. Huntemann, B. Lipphardt, V. Gerginov, N. Nemitz, M. Kazda, S. Weyers, and E. Peik. “Cs-Based Optical Frequency Measurement Using Cross-Linked Optical and Microwave Oscillators”. In: *Physical Review A* 89.2 (2014), p. 023820. DOI: 10.1103/PhysRevA.89.023820 (cit. on p. 44).
- [134] T. R. Tan, R. Kaewuam, K. J. Arnold, S. R. Chanu, Z. Zhang, M. S. Safronova, and M. D. Barrett. “Suppressing Inhomogeneous Broadening in a Lutetium Multi-ion Optical Clock”. In: *Physical Review Letters* 123.6 (2019), p. 063201. DOI: 10.1103/PhysRevLett.123.063201 (cit. on p. 11).
- [135] Y. Tanaka and H. Katori. “Exploring Potential Applications of Optical Lattice Clocks in a Plate Subduction Zone”. In: *Journal of Geodesy* 95.8 (2021), p. 93. DOI: 10.1007/s00190-021-01548-y (cit. on p. 9).
- [136] H. Telle, B. Lipphardt, and J. Stenger. “Kerr-Lens, Mode-Locked Lasers as Transfer Oscillators for Optical Frequency Measurements”. In: *Applied Physics B: Lasers and Optics* 74.1 (2002), pp. 1–6. DOI: 10.1007/s003400100735 (cit. on pp. 44, 45).
- [137] O. Terra, G. Grosche, and H. Schnatz. “Brillouin Amplification in Phase Coherent Transfer of Optical Frequencies over 480 Km Fiber”. In: *Optics Express* 18.15 (2010), pp. 16102–16111. DOI: 10.1364/OE.18.016102 (cit. on p. 41).
- [138] G. Tommaseo, T. Pfeil, G. Revalde, G. Werth, P. Indelicato, and J. P. Desclaux. “The g_J -factor in the ground state of Ca^+ ”. In: *The European Physical Journal D - Atomic, Molecular, Optical and Plasma Physics* 25.2 (2003), pp. 113–121. DOI: 10.1140/epjd/e2003-00096-6 (cit. on p. 80).
- [139] *Treizième conférence générale des poids et mesures*. 1967 (cit. on p. 3).
- [140] S. Weyers, V. Gerginov, M. Kazda, J. Rahm, B. Lipphardt, G. Dobrev, and K. Gibble. “Advances in the Accuracy, Stability, and Reliability of the PTB Primary Fountain Clocks”. In: *Metrologia* 55.6 (2018), pp. 789–805. DOI: 10.1088/1681-7575/aae008 (cit. on p. 4).

- [141] D. J. Wineland, R. E. Drullinger, and F. L. Walls. "Radiation-Pressure Cooling of Bound Resonant Absorbers". In: *Physical Review Letters* 40.25 (1978), pp. 1639–1642. DOI: 10.1103/PhysRevLett.40.1639 (cit. on p. 67).
- [142] D. J. Wineland, C. Monroe, W. M. Itano, D. Leibfried, B. E. King, and D. M. Meekhof. "Experimental Issues in Coherent Quantum-State Manipulation of Trapped Atomic Ions". In: *Journal of Research of the National Institute of Standards and Technology* 103.3 (1998), pp. 259–328. DOI: 10.6028/jres.103.019 (cit. on p. 51).
- [143] D. Wineland and H. Dehmelt. "Proposed $10^4 \delta\nu/\nu$ Laser Fluorescence Spectroscopy on Tl^+ Mono-Ion Oscillator III (Side Band Cooling)". In: *Bull. Am. Phys. Soc.* 20 (1975), p. 637 (cit. on p. 67).
- [144] F. Wolf, Y. Wan, J. C. Heip, F. Gebert, C. Shi, and P. O. Schmidt. "Non-Destructive State Detection for Quantum Logic Spectroscopy of Molecular Ions". In: *Nature* 530.7591 (2016), pp. 457–460. DOI: 10.1038/nature16513 (cit. on p. 7).
- [145] H. Wu and J. Müller. "Towards an International Height Reference Frame Using Clock Networks". In: International Association of Geodesy Symposia. Berlin, Heidelberg: Springer, pp. 1–8. DOI: 10.1007/1345_2020_97 (cit. on p. 8).
- [146] S.-H. Wu, M. Amezcuca, and H. Wang. "Adiabatic Population Transfer of Dressed Spin States with Quantum Optimal Control". In: *Physical Review A* 99.6 (2019), p. 063812. DOI: 10.1103/PhysRevA.99.063812 (cit. on p. 108).
- [147] J. B. Wübbena, S. Amairi, O. Mandel, and P. O. Schmidt. "Sympathetic Cooling of Mixed-Species Two-Ion Crystals for Precision Spectroscopy". In: *Physical Review A* 85.4 (2012), p. 043412. DOI: 10.1103/PhysRevA.85.043412 (cit. on pp. 11, 61).
- [148] Y. Zhao, Q. Wang, F. Meng, Y. Lin, S. Wang, Y. Li, B. Lin, S. Cao, J. Cao, Z. Fang, T. Li, and E. Zang. "High-Finesse Cavity External Optical Feedback DFB Laser with Hertz Relative Linewidth". In: *Optics Letters* 37.22 (2012), pp. 4729–4731. DOI: 10.1364/OL.37.004729 (cit. on p. 40).

Curriculum Vitæ

Personal data

Name Lennart Pelzer
Date of birth June 23, 1985
Place of birth Wiesbaden-Dotzheim
Nationality German

Employments

01/2015 – 01/2016 IT-Administrator, Elektro-Kuhlmann, Geisenheim
10/2014 – 01/2015 Internship, Elektro-Kuhlmann, Geisenheim
04/2009 – 02/2010 Academic Assistant, Johannes Gutenberg-Universität,
Mainz
08/2004 – 07/2005 Civil service, Arbeiter-Samariter-Bund, Wiesbaden

Education

02/2016 – today PhD student, QUEST - Institute for experimental quantum metrology, group of Prof. Dr. Piet O. Schmidt, Physikalisch-Technische Bundesanstalt, Braunschweig
10/2005 – 09/2013 Student of physics with degree *Diplom-Physiker*, Diploma thesis with the title "Ionisation von $^{40}\text{Ca}^+$ und Untersuchung gemischter $^{40}\text{Ca}^+ / ^{40}\text{Ca}^{2+}$ Ionenkristalle" prepared in group of Prof. Dr. Ferdinand Schmidt-Kaler, Johannes Gutenberg-Universität, Mainz
07/2004 Abitur, St. Ursula-Schule, Geisenheim

January 22, 2023

Publications

- T. Feldker, L. Pelzer, M. Stappel, P. Bachor, R. Steinborn, D. Kolbe, J. Walz, and F. Schmidt-Kaler. “Mode shaping in mixed ion crystals of $^{40}\text{Ca}^{2+}$ and $^{40}\text{Ca}^+$ ”. In: *Applied Physics B* 114.1 (2014), pp. 11–16. DOI: 10.1007/s00340-013-5673-1
- I. D. Leroux, N. Scharnhorst, S. Hannig, J. Kramer, L. Pelzer, M. Stepanova, and P. O. Schmidt. “On-Line Estimation of Local Oscillator Noise and Optimisation of Servo Parameters in Atomic Clocks”. In: *Metrologia* 54.3 (2017), pp. 307–321. DOI: 10.1088/1681-7575/aa66e9
- S. Hannig, L. Pelzer, N. Scharnhorst, J. Kramer, M. Stepanova, Z. T. Xu, N. Spethmann, I. D. Leroux, T. E. Mehlstäubler, and P. O. Schmidt. “Towards a Transportable Aluminium Ion Quantum Logic Optical Clock”. In: *Review of Scientific Instruments* 90.5 (2019), p. 053204. DOI: 10.1063/1.5090583
- M. Abdel-Hafiz, P. Ablewski, A. Al-Masoudi, H. Á. Martínez, P. Balling, G. Barwood, E. Benkler, M. Bober, M. Borkowski, W. Bowden, R. Ciuryło, H. Cybulski, A. Didier, M. Doležal, S. Dörscher, S. Falke, R. M. Godun, R. Hamid, I. R. Hill, R. Hobson, N. Huntemann, Y. L. Coq, R. L. Targat, T. Legero, T. Lindvall, C. Lisdat, J. Lodewyck, H. S. Margolis, T. E. Mehlstäubler, E. Peik, L. Pelzer, M. Pizzocaro, B. Rauf, A. Rolland, N. Scharnhorst, M. Schioppo, P. O. Schmidt, R. Schwarz, Ç. Şenel, N. Spethmann, U. Sterr, C. Tamm, J. W. Thomsen, A. Vianello, and M. Zawada. “Guidelines for developing optical clocks with 10^{-18} fractional frequency uncertainty”. In: *arXiv:1906.11495 [physics]* (2019). arXiv: 1906.11495 [physics]
- L. Pelzer, K. Dietze, J. Kramer, F. Dawel, L. Krinner, N. Spethmann, V. Martinez, N. Aharon, A. Retzker, K. Hammerer, and P. O. Schmidt. “Tailored optical clock transition in $^{40}\text{Ca}^+$ ”. In: *Measurement: Sensors* 18 (2021), p. 100326. DOI: 10.1016/j.measen.2021.100326
- V. J. Martínez-Lahuerta, L. Pelzer, K. Dietze, L. Krinner, P. O. Schmidt, and K. Hammerer. *Quadrupole Transitions and Quantum Gates Protected by Continuous Dynamic Decoupling*. 2023. DOI: 10.48550/arXiv.2301.07974. arXiv: 2301.07974 [quant-ph]

Acknowledgements / Danksagung

Diese Arbeit wäre nicht möglich gewesen ohne die Hilfe von sehr vielen Menschen. Ich möchte mich hier zumindest bei Einigen dafür bedanken:

Vielen dank, Piet für deinen kompetenten und gleichzeitig herzlichen Führungsstil. Du verstehst es, das Beste aus Einem rauszuholen ... und man hat auch noch Spaß dabei. Dein Fachwissen war sehr oft Gold wert. Vielen Dank an die Korreferenten dieser Arbeit Christian und Roe für ihre wertvolle Zeit in der Promotionskommission.

Besonders danken möchte ich meinen Mentoren Ian und Steven dafür, dass sie mich an ihrem riesigen Erfahrungsschatz haben teilhaben lassen. Das Gleiche gilt für Nils und Nicolas, die mir oft bei kleinen und größeren Problemchen geholfen haben. Stephan möchte ich für die Übergabe des hervorragenden experimentellen Aufbaus danken. Außerdem hast du mir immer mit Rat und Tat zur Seite gestanden.

Die Montage der schier endlosen Versionen von immer besseren CDD-Spulen verdanke ich Kai. Genauso wie die wertvolle Unterstützung beim Experimentieren. Ludwig hat einen unschätzbaren Beitrag für die Arbeit am Experiment geleistet und gleichzeitig immer super Stimmung verbreitet. Die längste gemeinsame Zeit bei IQLOC teile ich mit Johannes. Es war eine sehr *nice* Zeit mit dir! Vielen Dank für deine andauernde Hilfe beim Kammlocken. Speziell bei Fabian möchte ich mich für sein unermüdliches Korrekturlesen bedanken. Darüber hinaus hast du immer mit angepackt, wenn jemand gebraucht wurde.

Every experimenter would be happy to find such competent advice for the theoretical description of his measurements. Thank you for your great work Victor and Klemens.

Vielen Dank an die *Bewohner* des Paschen-Baus insbesondere Erik und Thomas. Ohne euren Si-lock wären meine Messungen kaum möglich gewesen. Das Difcos-Team, besonders Fabian, Max und Jan-Christoph war immer zu haben für vertiefte Diskussionen über Ionen fangen und andere Hobbies. Vielen Dank André, Hardik und Nicolas für die gute Labor-Nachbarschaft Fachsimpeln im Flur hat immer viel Freude bereitet und das gelegentliche Ausleihen von Komponenten war wirklich praktisch. Sandra und Sina haben immer souverän und geduldig meine administrativen Probleme gelöst. Nikolai, Tjerd, David und Julia waren immer eine große Hilfe für alle Elektronik Fragen. Grade in den ersten Jahren habe ich sehr von Ratschlägen von Sebastian, Jonas, Sofia und Christan zum Optimieren von Cavities profitiert.

Um allen geliebten Menschen zu danken würde der Platz hier niemals ausreichen.